Taiwan Microscopy Society

OXFORD INSTRUMENTS

JEO

Serving Advanced Techn

目　錄

頁數

一、第十三屆第一次中華民國顯微鏡學會年會會員大會暨
第二十七屆中華民國顯微鏡學會學術研討會大會會程……2

二、第十三屆理、監事名錄……3

三、中華民國顯微鏡學會新會員入會申請書……4

四、中華民國顯微鏡學會九十五年收支決算表、現金出納表、
資產負債表、和九十六年收支預算表……5

五、第二十七屆中華民國顯微鏡學會學術研討會
主題演講及論文摘要目錄……9
論文摘要……15

六、贊助廠商廣告……118

中 華 民 國 顯 微 鏡 學 會

PROCEEDING OF THE 27TH SYMPOSIUM ON MICROSCOPY

June 22, 2007, Shih-Pai, Nat'l Yang-Ming University

8:00 – 8:30	Registration	
8:30 – 9:00	Opening Ceremony (第三會議室)	
9:00 -9:50	陳力俊	ELECTRON MICROSCOPY FOR THE NANOTECHNOLOGY
10:00-10:50	高甫仁	IMPLEMENTING TIME-RESOLVED MICROSCOPY OF MOLECULAR DYNAMICS
10:50-11:50	第十三屆第一次中華民國顯微鏡學會年會會員大會	
12:00-13:30	Lunch (川堂午餐)	
Chairs	第二會議室(BIOMEDICAL SCIENCE): 楊瑞森、胡宇光	
13:30-13:45	胡宇光	GOLD NANOPARTICLES AND CELLS UNDER THE MICROSCOPES
13:45-14:00	李耀昌	THE BIOLOGICAL APPLICATION OF SYNCHROTRON RADIATION-BASED FOURIER TRANSFORM MICROSPECTROSCOPY
14:00-14:15	周逸鵬	THE SIGNALING MECHANISM UNDERLYING THE ANTI-ANGIOGENIC EFFECT OF β-LAPACHONE
14:15-14:30	楊瑞森	EFFECTS OF EMBEDDING MEDIA AND DIVALENT IONS ON THE STRUCTURE OF *EPINEPHELUS MALABARICUS* EGGS FOR TEM EXAMINATION
14:30-15:00	COFFEE BREAK (川堂)	
Chairs	第二會議室 (BIOMEDICIAL SCIENCE): 黃玲瓏、黃榮南	
15:00-15:15	黃玲瓏	THE ANATOMICAL CHARACTERISTICS OF *DENDROCALAMUS GIGANTEUS* MUNRO
15:15-15:30	黃榮南	GALECTIN-1 SUPPORTS IMMORTAL RAT CHONDROCYTE PROLIFERATION ON THE SURFACE OF CHITOSAN-COATED PLGA SCAFFOLD
15:30-15:45	盧國賢	IMMUNOHISTOCHEMICAL AND ULTRASTRUCTURAL STUDIES ON THE VALLATE TASTE BUD IN *DT/DT* AND *DB/DB* MICE
15:45-16:00	陳玉怜	STATINS INCREASE THROMBOMODULIN EXPRESSION IN HUMAN AORTIC ENDOTHELIAL CELLS WITH OR WITHOUT TUMOR NECROSIS FACTOR-A TREATMENT
Chairs	第三會議室(Material Science): 開執中、陳福榮	
13:45-14:00	陳福榮	PHASE PROBLEM IN TRANSMISSION ELECTRON MICROSCOPY
14:00-14:15	王蔚鈞	THE STUDY OF STRUCTURE REVERSION APPROACHING ATOMIC-RESOLUTION TOMOGRAPHY
14:15-14:30	殷廣鈐	PHASE IMAGING IN TRANSMISSION X-RAY MIRCROSCOPE
14:30-15:00	COFFEE BREAK (川堂)	
Chairs	第三會議室(MATERIAL SCIENCE): 陳正弦、開物	
15:00-15:15	CHEN, Hung-Sheng	Z-CONTRAST HOLLOW CONE DARK FIELD IMAGING
15:15-15:30	WU, Sheng-Wang	THE MICROSTRUCTURE EVOLUTION OF HIGH ENTROPY ALLOYS DURING HEAVY ION IRRADIATION AT ELEVATED TEMPERATURE
15:30-15:45	鍾鴻欽	DIRECT CORRELCTION OF In/Ga INTERMIXING WITH PHTOTLUMINESCENCE IN InAs/GaAs QUANTUM DOTS BY ENERGY FILTER TRANSMISSION ELECTRON MICROSCOPY
16:00 – 17:00	討論、頒獎、摸彩、閉幕 (第三會議室)	

中華民國顯微鏡學會

第十三屆理、監事名錄

理 事 長	游祥明	陽明大學醫學院解剖暨細胞生物學研究所	教授
副理事長	陳福榮	清華大學工程與系統科學系	教授
常務理事	張　立	交通大學材料科學與工程學系	教授
	黃玲瓏	台灣大學生命科學系	教授
	薛富盛	中興大學材料工程學系	教授
理　　事	沈博彥	中山大學材料科學研究所	教授
	林鶴南	清華大學材料科學與工程學系	教授
	陳正弦	台灣大學凝態中心	主任
	開　物	海洋大學材料工程研究所	教授
	黃宏圖	中山大學生物科學系	教授
	黃榮南	中央大學生命科學系	教授
	楊哲人	台灣大學材料科學研究所	教授
	楊瑞森	海洋大學海洋生物研究所	教授
	劉康庭	友聯光學股份有限公司	董事長
	蘇紘儀	台灣積體電路公司	故障分析處處長
常務監事	李志浩	清大工程與系統科學系	教授
監　　事	林招松	台灣大學材料科學研究所	教授
	張庭訓	捷東股份有限公司	董事長
	胡宇光	中央研究院物理研究所	研究員
	陳玉怜	台灣大學醫學院解剖暨細胞生物學研究所	教授
榮譽理事	李英雄	中國醫藥學院研發處	研發長
	侯書文	台灣大學醫學院病理科	教授
	陳脈紀	中興大學植物病蟲害系	教授
	吳信淦	中央研究院植物所	研究員
	林良平	台灣大學農化系	教授
	陳力俊	清華大學科學工程學系	教授
	王長君	輔仁大學解剖學科	教授
	開執中	清華大學工程與系統科學系	教授
秘 書 長	鄭瓊娟	陽明大學醫學院解剖暨細胞生物學研究所	教授

中華民國顯微鏡學會新會員入會申請書

(一)姓名:_____ 性別:_____

(二)服務機關:_____ 職務:_____

(三)通訊處:_____

_____

Phone: *Fax:*

E-mail:

(四)學歷: 畢業年月

(1)

(2)

(五)經歷:

(1)

(2)

(六)主要研究領域:

(1)

(2)

(3)

(七)申請入會為

(1)永久會員:入會費 NT.600	永久會費 NT.3000
(2)一般會員:入會費 NT.600	常年會費 NT.500
(3)學生會員:入會費 NT.200	常年會費 NT.200
(4)團體會員:入會費 NT.10,000	常年會費 NT.5000

(八)介紹人

(1)姓名:_____ 簽章:_____ 服務機關與職務:_____

(2)姓名:_____ 簽章:_____ 服務機關與職務:_____

(九)申請人簽章:_____

中華民國 年 月 日

【表一】

中華民國顯微鏡學會九十五年收支決算表

(95 年 1 月 1 日至 95 年 12 月 31 日)

單位：新台幣

科目				決算數		上年度決算數		本年度與上年度決算比較數				說明
款	項	目	名稱					增加		減少		
1			本會經費收入									
	1		入會費、會員年費	38,600		46,000				7,400		
	2		其他收入	155,000		150,000				5,000		
		1	利息收入	6,116		4,000		2,116		-		
2			本會經費支出									
	1		辦公費	27,910		40,000				12,090		
		1	文具及其他印刷費	33,605		50,000				16,395		
		2	郵電費	10,822		10,000		822				
	2		業務費	41,700		40,000		1,700				
			學會會刊印刷費	31,800		40,000				8,200		
	3		臨時工資	26,000		20,000		6,000				
3			本期餘絀	27,879		0						

理事長：游祥明　　秘書長：　　會計及製表：　　出納：

【表二】

中華民國顯微鏡學會

現金出納表

中華民國 95 年 12 月 31 日

單位：新台幣

收入之部		支出之部	
科目名稱	金額	科目名稱	金額
上期結存	1,220,992	本期結存	1,217,986
本期收入	199,716		
本期支出	202,722		
合計	1,217,986	合計	1,217,986

理事長：游明祥　　秘書長：　　會計及製表：　　出納：

【表三】

中華民國顯微鏡學會

資產負債表

中華民國 95 年 12 月 31 日

單位：新台幣

資產		負債、基金及餘絀	
科目	金額	科目	金額
流動資產 銀行存款	1,217,986	餘絀	1,217,986
合計	1,217,986	合計	1,217,986

理事長：游祥明　秘書長：　會計及製表：　出納：

		2	郵電費	10,000		10,000				-	
	3		業務費	30,000		40,000		1,700		10,000	
			學會會刊印刷費	40,000		40,000				-	
	4		臨時工資	30,000		20,000		10,000			
3			本期餘絀	0		0		23,700		62,000	

理事長：游祥明　秘書長：　會計及製表：　出納：

主題演講　PLENARY LECTURE

ELECTRON MICROSCOPY FOR THE NANOTECHNOLOGY
CHEN, Lih-Juann P-1----------P.15

IMPLEMENTING TIME-RESOLVED MICROSCOPY OF MOLECULAR DYNAMICS
GUKASSYAN, Vladimir and KAO, Fu-Jen..... P-2----------P.17

論文宣讀　ORAL PRESENTATION

[材料物理組]

PHASE PROBLEM IN TRANSMISSION ELECTRON MICROSCOPY
CHEN, Fu-Rong; HWANG, Sheng-Hui; WANG, Mugwort; HWU, Yeukuang;
CHANG, Wei-Hao; KAI, J. J. and CHANG, Jason.....M-O-1----------P.19

THE STUDY OF STRUCTURE REVERSION APPROACHING ATOMIC-RESOLUTION TOMOGRAPHY
WANG, Wei-Chun; CHEN, Fu-Rong and KAI, Ji-Jung..... ..M-O-2----------P.21

PHASE IMAGING IN TRANSMISSION X-RAY MIRCROSCOPE
YIN, Gung-Chian, CHEN, Fu-Rong, HWU, Yeukuang and LIANG, Keng-S.. M-O-3--------P.23

Z-CONTRAST HOLLOW CONE DARK FIELD IMAGING
CHEN, Hung-Sheng; CHEN, Fu-Rong; CHRISTIAN, Kisielowski and KAI,
Ji-Jung M-O-4----------P.25

THE MICROSTRUCTURE EVOLUTION OF HIGH ENTROPY ALLOYS DURING HEAVY ION IRRADIATION AT ELEVATED TEMPERATURE
WU, Sheng-Wang; LI, Shang-Wei; CHEN, Fu-Rong; YEH, Jien- We and
KAI, Ji-Jung.....M-O-5----------P.27

DIRECT CORRELCTION OF In/Ga INTERMIXING WITH PHTOTLUMINESCENCE IN InAs/GaAs QUANTUM DOTS BY ENERGY FILTER TRANSMISSION ELECTRON MICROSCOPY
CHUNG, Hung-Chin; LAI, Yi-Feng; LIU, Chuan-Pu; LAI, Yen-Lin; FANG, Yu-Ching, HSU, Li and
TANG, Shiang-Feng.....M-O-6----------P.29

[生物醫農組]

GOLD NANOPARTICLES AND CELLS UNDER THE MICROSCOPES
WANG, Chang-Hai; HUA, Tzu-En; LENG, Wei-Hua; LEE, Cheng-Feng; LIU, Chi-Jen and HWU, Yeu-Kuang.....B-O-1----------P.31

THE BIOLOGICAL APPLICATION OF SYNCHROTRON RADIATION-BASED FOURIER TRANSFORM MICROSPECTROSCOPY
LEE,Yao-Chang; HUANG, Pei-Yu and CHEN, Ching-Iue.....B-O-2----------P.33

THE SIGNALING MECHANISM UNDERLYING THE ANTI-ANGIOGENIC EFFECT OF β-LAPACHONE
CHAU, Yat-Pang; KUNG, Hsiu-Ni; KE, Ying-Ru and LU, Kuo-Shyan...B-O-3----------P.35

EFFECTS OF EMBEDDING MEDIA AND DIVALENT IONS ON THE STRUCTURE OF *EPINEPHELUS MALABARICUS* EGGS FOR TEM EXAMINATION
KAO, CHAO-FU AND YANG, JUI-SEN.....B-O-4----------P.37

THE ANATOMICAL CHARACTERISTICS OF *DENDROCALAMUS GIGANTEUS* MUNRO
KUO-HUANG, Ling-Long; HUANG, Yan-San; CHEN, Shin-Shin and CHEN, Shiang-Jiuun..... B-O-5----------P.39

GALECTIN-1 SUPPORTS IMMORTAL RAT CHONDROCYTE PROLIFERATION ON THE SURFACE OF CHITOSAN-COATED PLGA SCAFFOLD
Chang, Yu-Ying; Chen, Shinn-Jiuun; Tseng, Ching-Shiow; Tuan, Wei-Cheh and Huang, Rong-Nan..... B-O-6----------P.41

IMMUNOHISTOCHEMICAL AND ULTRASTRUCTURAL STUDIES ON THE VALLATE TASTE BUD IN *DT/DT* AND *DB/DB* MICE
SU, Yu-Jen; Kung, Hsiu-Ni; Chang, Chi-Fenand Lu, Kuo-Shyan.....B-O-7----------P.43

STATINS INCREASE THROMBOMODULIN EXPRESSION IN HUMAN AORTIC ENDOTHELIAL CELLS WITH OR WITHOUT TUMOR NECROSIS FACTOR-A TREATMENT
HSIEH, Fang-Yu; GUANG, I-I; WANG, Shu-Huei; LIN Shing-Jong ; KU Hung-Hai and CHEN,Yuh-Lien B-O-8----------P.45

論文壁報　POSTER PRESENTATION

[材料物理組]

MORPHOLOGY AND DIAMETER CONTROLLED SYNTHESIS OF Ag NANOSTRUCTURES WITH A SIMPLE GALVANIC DISPLACEMENT METHOD ON V FOILS
WANG, Chiu-Yen; LU, Ming-Yen and CHEN, Lih-Juann M-P-1----------P.47

CONTROLLED GROWTH OF ALIGNED ZnO NANOTOWERS WITH ENHANCED ULTRAVIOLET CATHODOLUMINESCENCE AND FIELD-EMISSION PROPERTIES
CHANG, Yu-Cheng and CHEN, Lih-Juann.....M-P-2----------P.49

Au-FILLED GA_2O_3 NANOTUBE AND ITS APPLICATION AS HIGH-TEMPERATURE NANOTHERMOMETER
Gong, Nan-Wei; Lu, Ming-Yen ; Wang, Chiu-Yen;Chen, Yu and Chen, Lih-Juann M-P-3----------P.51

PREPARATION OF 3-D ORDERED POROUS GA_2O_3 FILMS SYNTHESIZED VIA COLLOIDAL TEMPLATES
WU, Han-Wei; TSAI, Cho-Jen and CHEN, Lih-Juann M-P-4----------P.53

THE MICRO-FABRICATED ELECTROSTATIC ZERNIKE PHASE PLATE FOR PHASE CONTRAST IMAGING IN TEM
WANG, Wan Jhih; CHUANG, Y. J.; HUANG, S. H; HSU, C. H.; TSENG, F. G.1; KAI, J. J. and CHEN, F. R..... M-P-5----------P.55

THE STUDY OF NANO-CRYSTALLOGRAPH BY COHERENT ELECTRON DIFFRACTION IMAGING
FENG, Chi-Kai , Dronyak Roman1; CHEN, Fu-Rong1 and KAI, Ji-Jung ...M-P-6---------P.57

VALENCE STATE MAP OF IRON OXIDE THIN FILM OBTAINED FROM ELECTRON SPECTROSCOPY IMAGING SERIES
CHEN, Ko-Feng; KAI, Ji-Jung and CHEN, Fu-Rong.....M-P-7----------P.59

ANNEALING EFFECT ON ELECTROCHROMIC PROPERTIES OF TUNGSTEN OXIDE NANOWIRES
LIAO, Chia-Ching; CHEN, Fu-Rong and KAI, Ji-Jung.....M-P-8----------P.61

TEM STUDY OF NANOCRYSTALLINE ZrNxOy THIN FILM
Liu, Yee-Langa; HUANG, Ja-Honga; CHEN, Fu-Ronga and KAI, Ji-Junga...M-P-9-------P.63

OBSERVATION OF V-DEFECTS IN MULTIPLE INGAN/GAN QUANTUM WELLS
Tsai, H. L.; Wang, T. Y.; Yang, J. R.; Kuo, T. W.; Feng, Z. C. and
Li, Alan G.....M-P-10---------P.65

ELECTROCHROMIC PROPERTY OF NANO-COMPOSITE PRUSSIAN BLUE BASED THIN FILM
CHENG, Keng-Che; CHEN, Fu-Rong and KAI, Ji-Jung.....M-P-11----------P.67

STEM-EELS INVESTIGATION OF AU NANOPEAPODS EMBEDDED IN SILICA
WU, Chien-Ting; CHEN, Chun-Wei; CHEN, Kuei-Hsien; CHEN, Li-Chyong;
CHU, Ming-Wen, CHEN, Cheng-Hsuan.....M-P-12----------P.69

ELECTRONIC MICROSCOPY STUDY OF EPITAXIAL GROWTH OF GALLIUM NITRIDE ON PATTERNED SAPPHIRE SUBSTRATES
CHEN, Hou-Guang; CHANG, LI, WU, Yue-Han; KO, TS; LU, Tien-Chang;
KUO, Hao-Chung and WANG, Shing-Chung.....M-P-13----------P.71

INVESTIGATION OF THE HIGH-ORDER-LAUE-ZONE LINES' SPLITTING BY KINEMATICAL CBED SIMULATION
KO, Yu-Feng; LI, CHANG; CHU, HongYuan and LEE, Jon C.....M-P-14----------P.73

THE PH EFFECT TO THE PHOSPHATE-PERMANGANATE CONVERSION COATING ON THE AZ31 MAGNESIUM ALLOYS
CHU, Y. R.; LI, W. J. and LIN, C. S.....M-P-15----------P.75

IN-SITU TEM HEATING ZINC-ZINC OXIDE CORE-SHELL NANOWIRES
CHEN, Yen-Chih; TU, Chia-Hao and LIU, Chuan-Pu.....M-P-16----------P.77

THE-OXIDATION OF A $Pd_{40}Ni_{40}P_{20}$ BULK AMORPHOUS ALLOY AT 350-450°C IN DRY AIR.
JEN, I-Fei; HSIEH, Hsin-Hsin; Ho, Jih-Hsin; CHEN, Yen-Jung and KAI,
Wu.....M-P-17----------P.79

MICROSTRUCTURE EVOLUTION OF A Ti-Mo CONTAINING STEEL
Kao, Fang-Hsin; Chen, Chih-Yuan; Li, Wei-Chi; Chang, Hsiao-Tzu and Yang,
Jern-Ren M-P-18----------P.81

TEM INVESTIGATION ON A GALVANEALLED DUAL PHASE STEEL
Kao, Fang-Hsin; Chen, Chih-Yuan and Yang, Jern-Ren.....M-P-19----------P.83

THE EFFECT OF INTERRUPTED COOLING TEMPERATURE ON THE PRECIPITATION BEHAVIOR IN THE NOVEL HSLA STEEL
Chen, Chih-Yuan; Kao, Fang-Hsin; Hsu, Cheng-Hsun; Li, Xi-Yi and Yang, Jern-Ren M-P-20----------P.85

EFFECT OF NANOCRYSTAL ON THE MEMORY CHARACTERISTICS OF HIGH-κ HfAlO CHARGE TRAPPING LAYERS FOR NANO-SCALE NON-VOLATILE MEMORY DEVICE APPLICATIONS
WANG, T.Y.; Maikap, S. and YANG, J.R.....M-P-21----------P.87

NEW CHALLENGES ON TRANSMISSION ELECTRON MICROSCOPY FOR NEW GENERATION GaN-BASED LIGHTTING DEVICES
FENG, Zhe Chuan; TSAI, Hong-Lin and YANG, Jer-Ren.....M-P-22----------P.89

TREATMENTS FOR ENHANCING CHEMICAL AND PHYSICAL PROPERTIES OF ANODIC TITANIUM OXIDE FILM
CHEN, M.-T; Liu, J.-H. and Lin, C.-S.....M-P-23----------P.91

[生物醫農組]

THE AUTONOMOUS NOTCH SIGNAL PATHWAY IS ACTIVATED BY BAICALIN AND BAICALEIN BUT IS SUPPRESSED BY NICLOSAMIDE IN K562 CELLS
WANG, An-Ming; LEE, Shao-Pei; LIAO, Wan-Ru and YEH, Tien-Shun....B-P-1----------P.93

NEOVASCULARIZATION AND MORPHOLOGICAL CHANGES IN THE PRENATAL DEVELOPING AND LASER INDUCED RATS
LU, Min; CHEN, Yu-Lin; YANG, Chen-Chang; CHEN, Yi-Ting; YANG, Chang-Shu and YU, Shang-Ming.....B-P-2----------P.95

THE APPLICATION OF THE MESENCHYMAL STEM CELLS IN WHARTON'S JELLY OF THE HUMAN UMBILICAL CORD ON TREATMENT FOR ISCHEMIA/REPERFUSION STROKE OF RAT
LIN, Yu-Ching and FU, Yu-Show.....B-P-3----------P.97

THE STUDY OF STAMINATE AND HERMAPHRODITE FLOWERS ON FLORAL DEVELOPMENT AND MICROSPOGENSIS IN *KOELRETERIA HENRYI* DUMMER (SAPINDACEAE)
Lin, Chiou-Huey and Su-Hwa Chen.....B-P-4----------P.99

INVOLVEMENT OF ENDOPLASMIC RETICULUM STRESS-MEDIATED SIGNALS IN β-LAPACHONE-INDUCED APOPTOSIS

KE, Ying-Ru; Lien, Yi-Chen and CHAU, Yat-Pang.....B-P-5---------- P.101

TRANS-DIFFERENTIATION OF HUMAN MESENCHYMAL STEM CELLS IN WHARTON'S JELLY INTO INSULIN-PRODUCING CELLS
HSU, Hsin-Chih and Wang, Hwai-Shi.....B-P-6----------P.103

EFFECT OF ISCHEMIA ON THE ULTRASTRUCTURAL ALTERNATION OF THE HIPPOCAMPUS IN THE GERBIL
CHEN, Yu-Lin; YANG, Cheng-Chang; LU, Min; CHEN Yi-Ting and YU, Shang-Ming.....B-P-7----------P.105

CHARACTERIZATION OF INSECTICIDAL ACTIVITY OF GALECTIN-1 AGAINST *PLUTELLA XYLOSTELLA*
CHIEN, Chin-I; CHEN, Shiang-Jiuun; CHEN, Nien-Ting; WANG, Siou-Hua; KUO-HUANG, Ling-Long and HUANG, Rong-Nan.....B-P-8----------P.107

MORPHOLOGICAL CHANGES DURING SPONTANEOUS RECOVERY AFTER SPINAL CORD INJURY
YANG, Cheng-Chang; CHEN, Yu-Lin; LU, Min; LIN, Kwan-Hwa and YU, Shang-Ming.....B-P-9----------P.109

DIFFERENTIAL DISTRIBUTION OF GFP-TAGGED RAT EAG1 AND EAG2 K^+ CHANNELS IN NEURONS
JENG, Chung-Jiuan; LIN, Huei-Min; and TANG, Chih-Yung.....B-P-10----------P.111

THE DEVELOPMENT OF MALE STROBILI AND ICROSPOROGENESIS OF *TAIWANIA CRYPTOMERIOIDES* HAYATA (TAXODIACEAE)
CHEN, Su-Hwa; CHUNG, Nien-June; WANG, Ya-Nan; LEE, Jin-Ling and LEE, Yi-Ling.....B-P-11----------P.113

HNOLOGY

University,

he turn of the
to impact the
I) has become
ocations in thin
r component in
ron microscope
ing microscope
s. The timely
SEM) with a
pid advance in
strate how the

nder FESEM
e-dimensional
nowires were
nolenses with
with a special

the analysis of
. The growth
The crystalline
yramid-shaped
operties were
ectromigration
s between

Self-aligned nanowires and substrate were determined from the analysis of EDP [5].

3. Chemical compositions: Chemical compositions are determined from energy dispersive spectrometers (EDS) or electron energy loss spectrometer (EELS) attached to a TEM. High angle annular dark field images are most useful to differentiate nano-heterostructure [2].

4. Polarity of polar crystals: The polarity of polar crystals is determined from convergent beam electron diffraction (CBED) or HRTEM analysis.

5. Dynamical changes in nanostructures: In-situ ultrahigh-vacuum transmission electron microscopy (UHV-TEM) is an extremely valuable method for clarifying the growth mechanism of nanowires since it can monitor in nanoscale the dynamical process as it occurs. In contrast, post-process investigations often lead to confusing hypotheses owing to the complexity of the process. Growth of high-density titanium silicide nanowires in a single direction on a silicon surface was achieved [6].

6. Piezo-response: Nanomanipulation to measure the in-situ I-V characteristics of a single ZnO NW in a FESEM has been carried out. The electric transport was dominated by piezoelectric characteristic of ZnO, which is induced by stain. It has been demonstrated that a single ZnO NW can be a rectifier simply by mechanical bending, similar to a p-n junction based diode. To quantify the barrier height produced by piezoelectricity, the I-V characteristics received at different level of the deformation were tied in with theoretical calculation. In addition, under appropriate bending and voltage control, each NW array could correspond to a device element for RAM application [7].

References

[1] Y.L. Chueh, M.T. Lo, L.J. Chou, L.J. Chen, C.S. Wu, and C.D. Chen, Nano Lett. 6 (2006) 1637

[2] H.C. Chen, S.W. Lee, and L.J. Chen, Adv. Mater. 19 (2007) 222

[3] H.C. Chen, C.W. Wang, S.W. Lee, and L.J. Chen, Adv. Mater. 18 (2006) 367

[4] K.C. Chen, C.N. Liao, W.W. Wu, and L.J. Chen, Appl. Phys. Lett. 90 (2007) 203101

[5] C. L. Hsin, J. H. He, C. Y. Lee, W. W. Wu, P. H. Yeh, L. J. Chen, and Z. L. Wang, Nano Lett.
(online, May 21, 2007).

[6] H.C. Hsu, W.W. Wei, H.F. Hsu, and L.J. Chen, Nano Lett. 7 (2007) 885

[7] J.H. He, C.L. Hisn, J. Liu, L.J. Chen, and Z.L. Wang, Adv. Mater. 19 (2007) 781

P-2: IMPLEMENTING TIME-RESOLVED MICROSCOPY OF MOLECULAR DYNAMICS

GUKASSYAN, Vladimir (古維迪)[a] and KAO, Fu-Jen (高甫仁)[a]
[a]Institute of Biophotonics, National Yang-Ming University, Shih-Pai, Taipei 112, Taiwan.

The challenge for the 21st century is to understand how molecular characters work together to make living cells and organisms. This quest depends heavily on molecular imaging, which shows when and where genetically or biochemically defined molecules, signals or processes appear, interact, and disappear, in time and space. The rapid advancement of novel photonics technologies over the last decade has enabled unprecedented opportunity in probing the crucial mechanisms in life science. As such, the fluorescence resonance energy transfer (FRET) resolved by the fluorescence lifetime imaging (FLIM) has emerged as one of the powerful techniques with temporal and spatial resolution at picosecond and nanometer level. Among all lifetime imaging techniques, the time-correlated single photon counting (TCSPC) has demonstrated the highest recording efficiency and time resolution.

A TCSPC system based on the two-photon microscopy has been established at the National Yang-Ming University Imaging Core. Here we present the results of the system deployment, performed in collaboration with scientific groups of the NYMU, or carried out under our technical consultancy and/or user service. Informative applications of the time-resolved microscopy platform on virus infection and apoptosis of cells will be stressed.[1]

References

[1] V. Gukasyan, Y.Y. Hsu, S.H. Kung, and F.J. Kao, J. of Biomedical Optics 12, (2007) 024016.

[2] I.A. Demarco, A. Periasamy, C.F. Booker, and R.N. Day, Nature Methods 3(2006)519.

[3] H. Wallrabe and A. Periasamy, FRET-FLIM microscopy and spectroscopy in the biomedical sciences. Current Opinion in Biotechnology. 16 (2005)19.

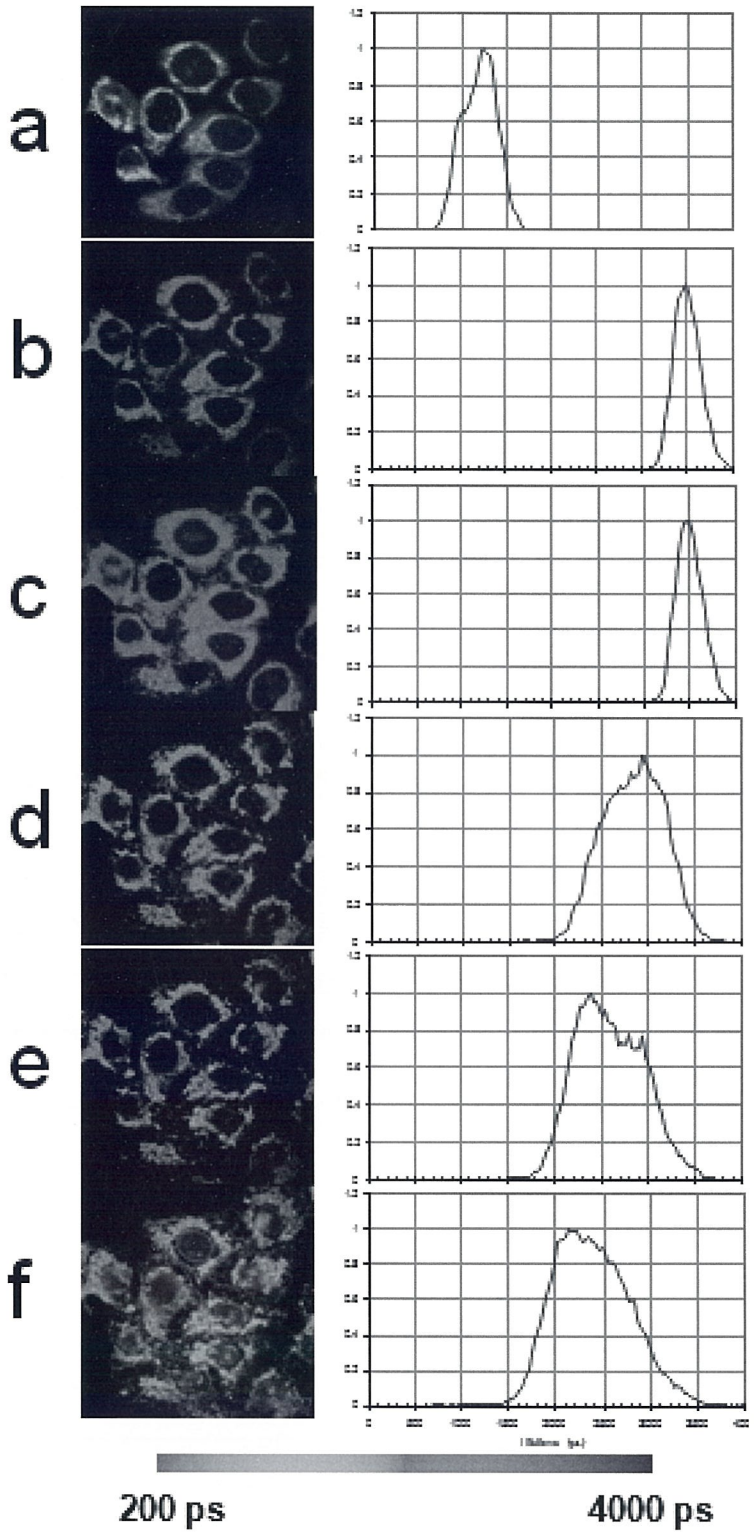

Fig. 1. Lifetime observation in HeLa cells at 15 (a), 30(b), 45 (c), 60(d), 75 (e) minutes and 10 hours (f) after treatment with apoptosis inducer staurosporine (STS). Magnified image shows characteristic to apoptosis morphological changes: nucleus shrinking and blebbing.

M-O-1: Phase Problem in Transmission Electron Microscopy

CHEN, Fu-Rong(陳福榮)[1,2,3]; HWANG, Sheng-Hui[1]; WANG, Mugwort[1]; HWU, Yeukuang[3]; CHANG, Wei-Hao[3]; KAI, J. J.[1] and CHANG, Jason[3]

1. Department of Engineering and System Science, National Tsing Hua University, HsinChu 30013, Taiwan. 2. National Synchrotron Radiation Research Center, HsinChu, Taiwan. 3 Institute of Physics, Academic Sinica, Taiwan.

The phase information in TEM has been lost in the recording system. This hinders the ultimate goal of the high resolution transmission electron microscopy (HRTEM) is to determine the 3-dimensional atomic structure for arbitrary object (crystalline and biological samples). In the case of crystalline sample, high resolution images do not reveal real atomic structure directly and the structural and chemical information related to the thickness can be heavily encoded due to the presence of dynamical diffraction and the lens aberration. Although recently developed Cs corrected TEM helps to remove the lens aberration, in general, the strong interaction nature between the incident electron and the crystal potential distorts one to one correspondence of the exit wave and the projected potential of crystalline sample, especially in the case of thick sample containing heavy element. The biological samples have extra problems in lack of contrast and radiation damage. The above mentioned problems may be overcome by recovering the phase information lost in the microscopy system to reach the 3-d phase tomography. In this paper, we will present the methodologies to solve the phase problem through retrieving the phase information from through focal images (for crystalline sample) , precisely determination of the lens aberration function and the phase plate images (for biological sample). Examples for crystalline sample and biologic sample are given follow. As shown in the fig. 1(a) is a simulated image of the ferritin on carbon film. The diameter of ferritin is and thickness of carbon are all 12nm. Fig. 1(b) shows a simulated phase contrast image of the same ferritin/carbon film recorded with phase plate on. The pure phase information of the ferritin can be deduced from Fig. 1(b). The tomography from the intensity and phase tilt series can be reconstructed and the detail will be presented in the workshop.

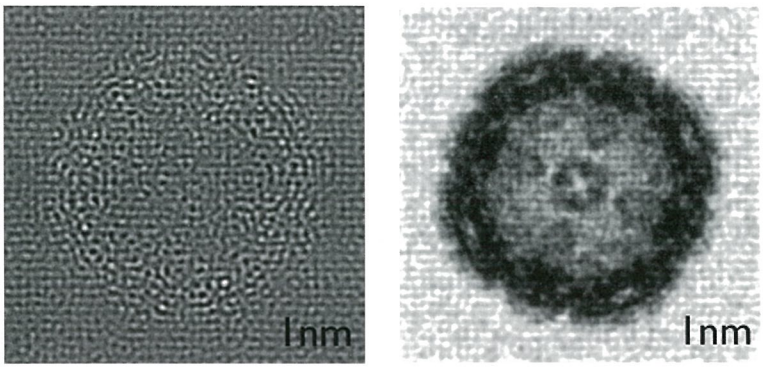

(a) (b)

Fig. 1(a) is a simulated image of the ferritin on carbon film. (b) a simulated phase contrast image of the same ferritin/carbon film recorded with phase plate on

M-O-2: THE STUDY OF STRUCTURE REVERSION APPROACHING ATOMIC-RESOLUTION TOMOGRAPHY

WANG, Wei-Chun(王蔚鈞), CHEN, Fu-Rong and KAI, Ji-Jung

Center for Electron Microscopy, Department of Engineering and System Science, National Tsing-Hua University, Hsinchu

The ultimate goal of the high resolution transmission electron microscopy (HRTEM) is to determine the atomic structure for an arbitrary object. As well known, the image-formation process in HRTEM is highly influenced by dynamical scattering effects and distortions from the lens aberrations, which make it necessary to relate object and images by extensive calculations. The study of structure reversion is a two-step procedure: first the exit wave, the electron wave at the exit plane when it passes through the specimen, especially the phase information is recovered; then the structure is reconstructed from the information of the exit wave since it is mostly related to the structure. The phase of the image plane can be recovered by the Gerchberg-Saxton method [1] or the focal series reconstruction method [2].Once the phase is retrieved in the image plane, it is obvious that the exit wave can be reconstructed simply by deconvoluting the "blurring" function that results from microscope aberrations and electron beam incoherency. Reconstruction of the whole three-dimensional structure is called tomography. Here we propose to compare reverse multislice method [3], reverse projected potential method combining with matrix reconstruction [4] to approach to atomic resolution tomography.

A wedge-shaped $NiSi_2$ is taken as a simulation sample in this research. $NiSi_2$ is composed of four Ni atoms forming a face-centered cubic structure with eight Si atoms positioning at a quarter of the lattice parameter relatively to them. The microscope settings are 300 keV with spherical aberration constant Cs=0.5 mm, chromatic aberration Cc=1.3 mm and the focus spread due to the incoherency of electron beam Δ=32.5 Å. As shown in Figure 1, the structure reversion based on reverse multislice method can give accurate number of unit cell layers up to 10 slices. And in Figure 2, a 3-D atomic resolution tomography of the $NiSi_2$ is shown.

Reference:

[1] R. W. Gerchberg and W. O. Saxton, Opitk 35 (1972) 237

[2] M. Op de Beeck, D. Van Dyck and W. Coene, Ultramicroscopy 64 (1996) 167

[3] F. R. Chen, C. Kisielowski *et al.*, submitted to Ultramicroscopy

[4] D. Gale, Pacific J. Math 7 (1957) 1073

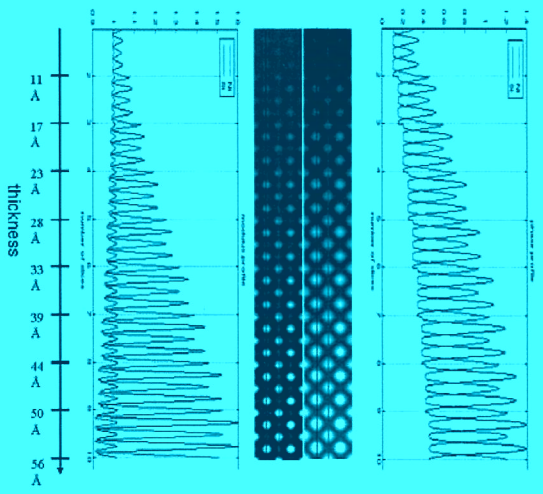

(a)

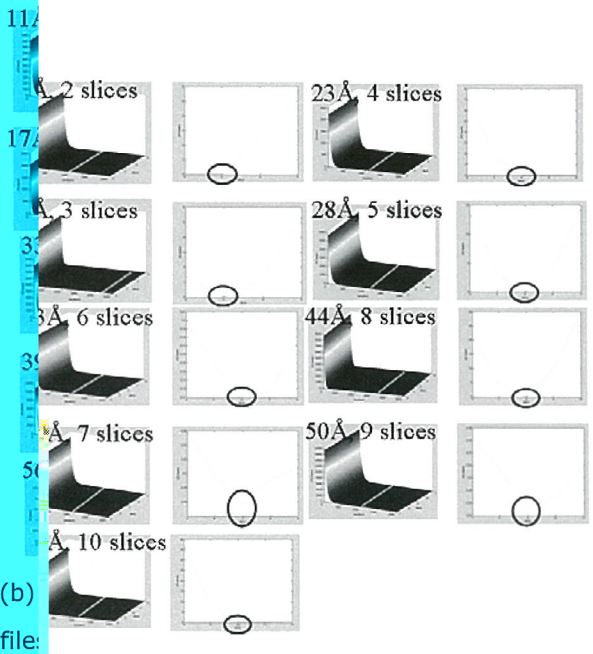

(b)

Figure 1. (a) Modulus (left) and phase (right) profiles of the exit waves from 11 Å to 56 Å. (b) Using reverse multislice method, it is possible to determine the number of unit cell for each thickness.

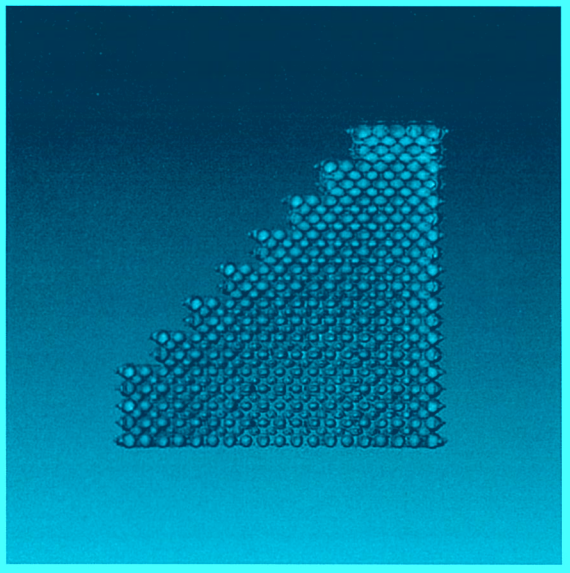

(a)

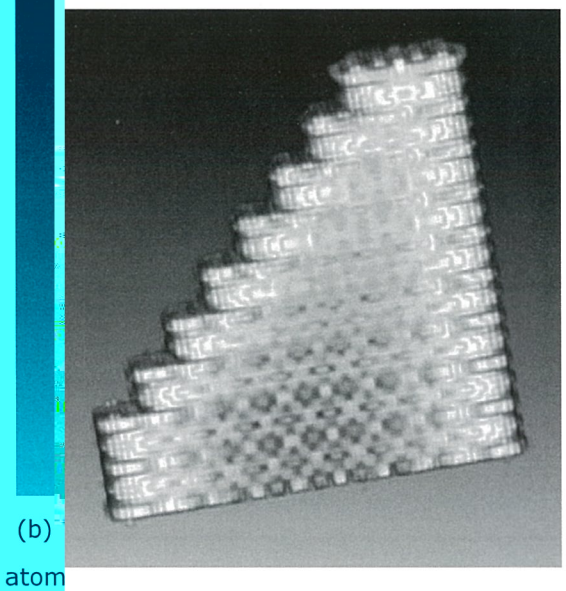

(b)

Figure 2. The reconstructed $NiSi_2$. From (a), the Ni atoms are clearly shown; (b) The Si atoms are slightly distinguished since the intensity for two Si atoms is likely the same magnitude as one Ni atom.

M-O-3: PHASE IMAGING IN TRANSMISSION X-RAY MIRCROSCOPE

YIN, Gung-Chian (殷廣鈐)[a,b]; CHEN, Fu-Rong (陳福榮)[a];
HWU, Yeukuang (胡宇光)[c]; LIANG, Keng-S. (梁耕三)[a] ;

[a] National Synchrotron Radiation Research Center, 101 Hsin-Ann Road, Hsinchu 30076, Taiwan..

[b] Department of Photonics and Display Institute, National Chiao Tung University, Hsinchu 30076, Taiwan.

[c] Institute of physic, Academic Sinica, Taipei 115, Taiwan

In x-ray imaging, the phase contrast is generally 100 to 1000 times higher than the absorption contrast in soft material. However, the quantitative phase information is required for the phase tomography in order to fully utilize the capability of the x-ray imaging. In this work, we demonstrate that the quantitative phase retrieval with a sub-100nm resolution can be achieved from micrographs of zone plate based transmission x-ray microscope (TXM)[1-3]. In this work, a zone plate made of plastic containing objects of sizes from μm down to tens of nano-meter is used as a test sample to quantify the retrieved phase. Using the focal serial images in the image plane, the phase information is retrieved quantitatively across the entire range of sizes by combining the transport intensity equation (TIE) [4] and self-consistent wave propagation methods (SCWP)[5] in this partial coherence system. The results show a good agreement with simulation. The study demonstrates a solution to retrieve the phase in the TXM and overcome the deficiency encountered in the two phase retrieval approaches of TIE and SCWP(Fig1.).

The phase imaging by Zernike's Phase Contrast will also be demonstrated (Fig2), and the methods and results for qualitatively phase retrieval from Zernike' phase contrast will be presented.

References

[1] G. Yin, et al., Appl. Phys. Lett. **88**, 241115 (2006)

[2] G. Yin, et al., Appl. Phys. Lett. **89**, 221122(2006)

[3] G. Yin, et al., Appl. Phys. Lett. **90**, 181118 (2007)

[4] K. A. Nugent, et al., Phys. Rev. Lett. **77**, 2961 (1996)

[5] W. Hsieh, et al., Ultramicroscopy **98**,99 (2004)

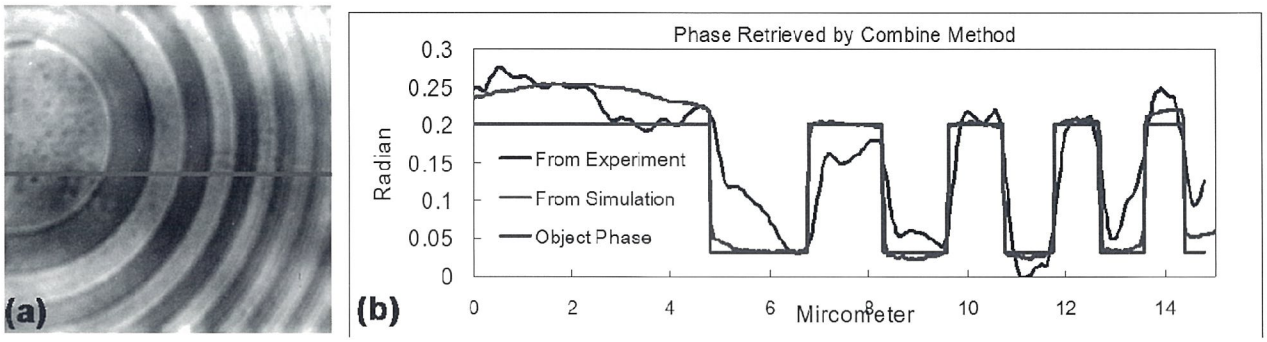

Fig1. The result phase retrieved from the plastic zone plate. (a) the phase image of zone plate. (b) the cross section plot of red line in (a).

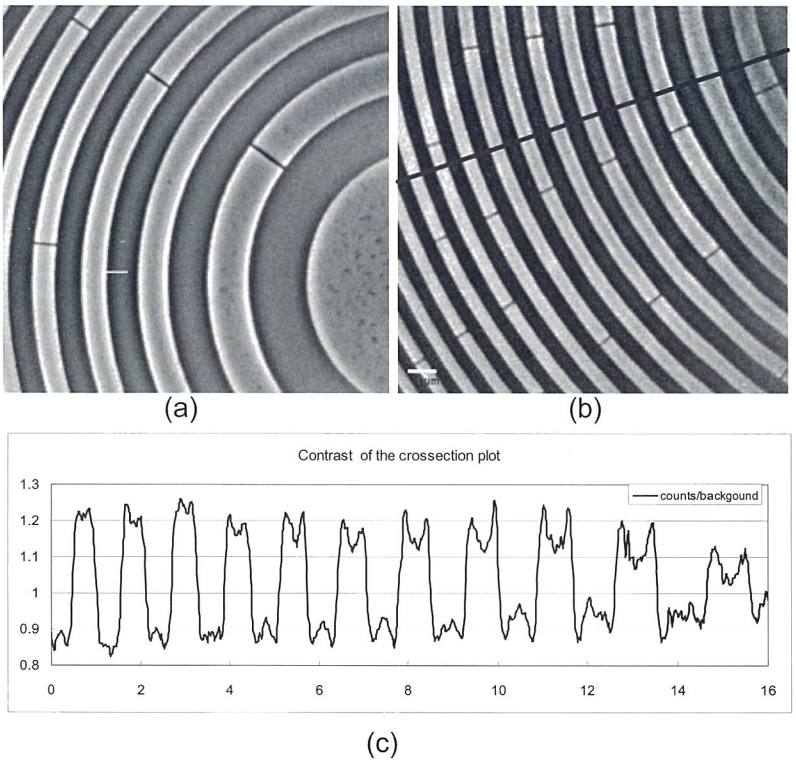

Fig2. The x-ray imaging of plastic zone plate by Zernike's Phase contrast method. (a) is the image taken in the center of the zone plate, and (b) is the image taken about 15 μm away from the center of zone plate. (c) is the cross-section plot of the red line in (b)

M-O-4: Z-contrast Hollow Cone Dark Field Imaging

CHEN, Hung-Sheng[1]*, CHEN, Fu-Rong[1], CHRISTIAN, Kisielowski[2] and KAI, Ji-Jung[1]

[1]Center for Electron Microscopy, Department of Engineering and System Science, National Tsing-Hua University, HsinChu, Taiwan. 30043, R.O.C.
[2]National Center for Electron Microscopy, Lawrence Berkeley National Lab., U.S.A.
*Correspondence:d9511809@oz.nthu.edu.tw

Z-contrast imaging was first realized by HAADF-STEM in 1970s. However, according to the principle of reciprocity, Z-contrast imaging can be realized in CTEM by hollow-cone illumination.[1] We demonstrate Z-contrast imaging can be obtained by using superposition of high-angle tilt series, which is effectively identical to hollow-cone illumination. The series images were registered(aligned) by Phase Correlation Function (PCF) and sum all images to average all the images from different orientation. The feasibility of the method was shown by an advance VLSI sample and a Al-4wt%Cu alloy sample with θ precipitates.

Fig.1 is a diagram of focused scanning probe and dynamic hollow cone illumination. For high-angle hollow cone illumination, incident beam and Bragg reflection beams are stopped by the aperture and excluded from imaging. Images formed by high-angle scattered electrons effectively suppress the image contributions originating from diffraction contrast [2].

For the incident beam was tilted to 113mrd relative to the optic axis and the objective aperture covers 26mrad, the hollow cone Z-contrast images were formed by the electrons scattered to 100~126mrad. The amount of images in one tilt series of images depends on the beam tilting angle 2θ and the size of the objective aperture.

Fig.2 (a) shows a bright field (BF) TEM image. Fig.2 (b) is an average image which is a superposition of 25 high-angle CDF images in different azimuth angles, and Fig.2(c) is a HAADF-STEM image. And, Fig. 3. is the BF, HCDF and HAADF experimental results of Al-4wt%Cu alloy sample. These two sample show discrete hollow cone dark field is compatible with HAADF in median resolution range.

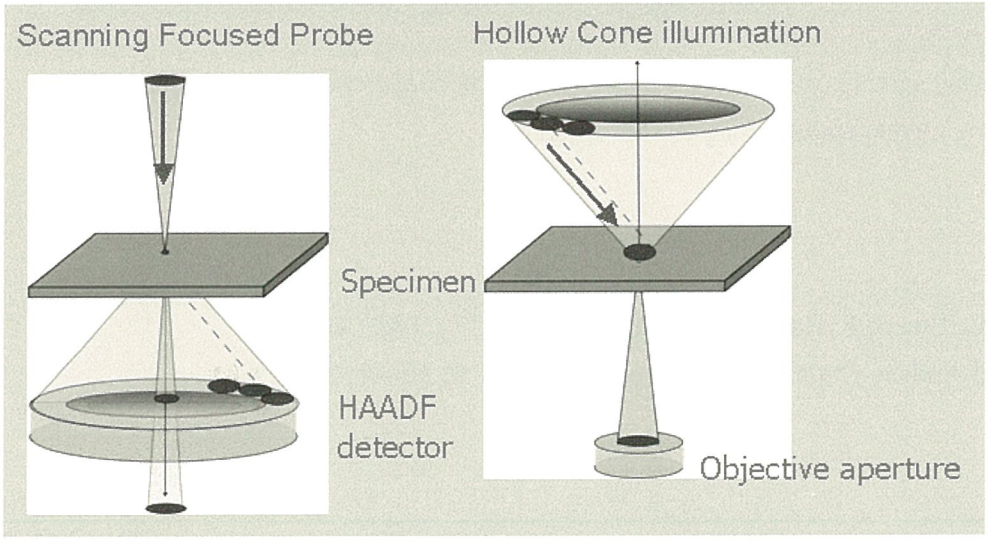

FIG. 1. The scanning focused probe of STEM and the hollow cone illumination in TEM. The contrast of images obtained by these two modes would be identical, which is based on the principle of reciprocity.

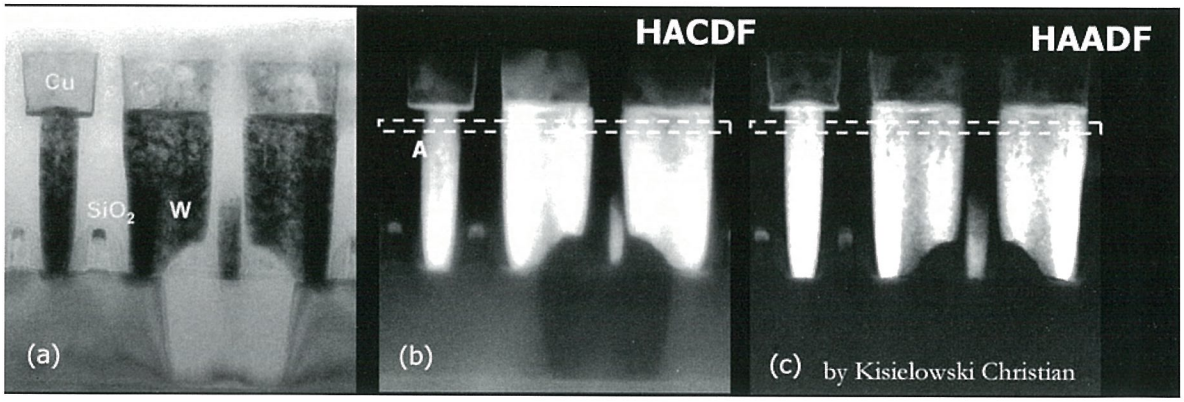

FIG. 2. (a) Bright field image of a VLSI sample, (b) is an average image which comes from 25 high-angle CDF images, (c) is a HAADF image.

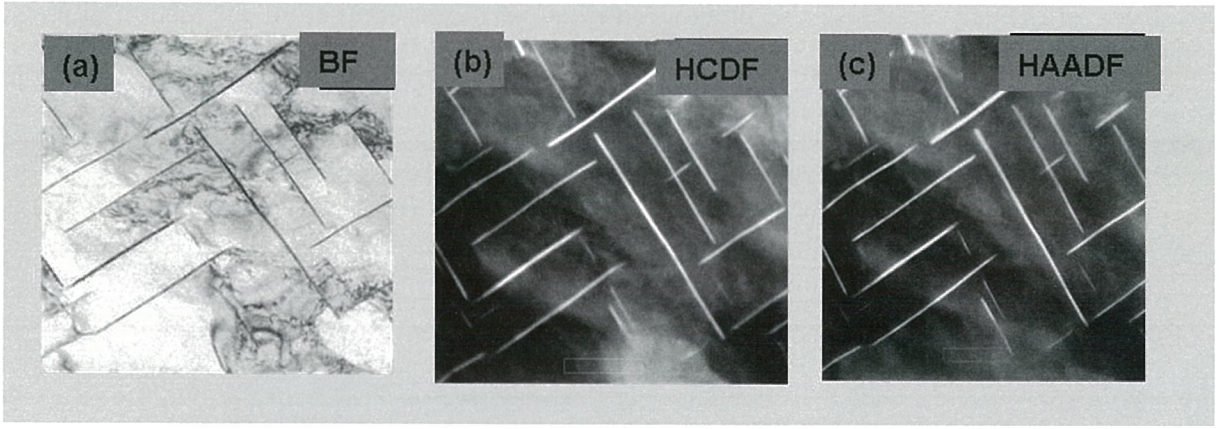

FIG.3 Al-4wt%Cu alloy sample (a)BF image , (b) Hollow cone DF image of collection angle range 113-140mrad, and (c) STEM-HAADF image of 60-160mrad

Reference:

[1] G. Schmitz, J.C. Ewert, F. Hartung, Ultramicroscopy 77 (1999) 49-63

[2] Ute Kaiser and Andrey Chuvilin, Microsc. Microanal. 9, 36–41, 2003

M-O-5: The Microstructure Evolution of High Entropy Alloys during Heavy Ion Irradiation at Elevated Temperature

WU, Sheng-Wang*, LI, Shang-Wei, CHEN, Fu-Rong[1], YEH, Jien- Wei[2] and KAI, Ji-Jung[1]

[1]Center for Electron Microscopy, Department of Engineering and System Science, National Tsing-Hua University, HsinChu, Taiwan. 30043, R.O.C.
[2]Department of Material Science and Engineering, Nation Tsing Hua University, HsinChu, Taiwan 30043, R.O.C
Correspondence:g943146@oz.nthu.edu.tw

In reviewing the development of previous alloy systems, it has always been confined to the structure of one or two main elements. We have put forward a brand-new concept of alloy design, namely "high-entropy alloy", disposeing the alloy with 5 main elements and up to 13 elements with the concentration of each element between 35 and 5 at.% [1].

The continuing improvements in the high-entropy alloys have led to many new and fascinating applications that require high strength, thermal stability, wear resistance, and corrosion resistance. From this new idea, we attempt to develop the alloy with these properties in order to reclaim a new application in fusion reactor structure materials. However, there is very limited study on microstructural stability of the high-entropy alloy under ion-beam irradiatioion at elevated temperature.

In order to investigate the value of using high-entropy alloy as the first wall structure materials, we proceeded ion-beam irradiation experiments at elevated temperature 400~900℃ and used mechanical test and HETEM equipped electron energy loss spectrometer to study radiation effect on the microstructure evolution for high-entropy alloys.

$Ti_{0.5}CrCo_{1.5}FeNi_{1.5}$ high-entropy alloy is the hardest FCC-type alloy ever found. As shown in Fig. 1, its temperature capability is higher than IN 713C and Rene 80 by 120℃ and 180 ℃. Fig.2 illustrates the aging curve of the alloy under different temperature, and there was a rare precipitation-hardening phenomenon. The microstructure of specimen irradiated to 10 dpa at 400℃ consisted of many defect clusters (<10nm in diameter) as shown in Fig.3. Furthermore, we observed the ion beam irradiation also suppressed the growth of γ' phase, and the size of γ' became more tiny as the damage dose increase (see Fig. 4). To conclude, the ion beam irradiation can cause a big change in microstructure. The suppressed growth of γ' phase may result in the change micro-hardness. Therefore, it needs micro-indentation hardness test results to clarify the radiation effects on microstructure

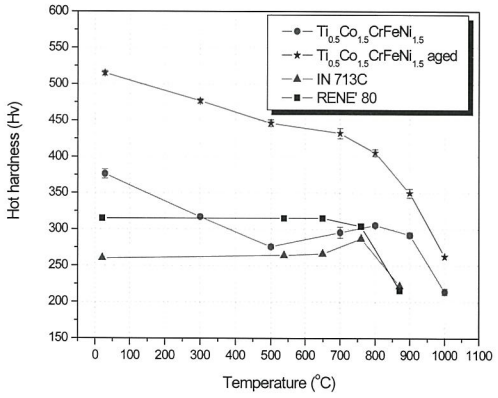

Fig. 1 The Vickers hardness test of high entropy and commercial superalloys under different temperature.

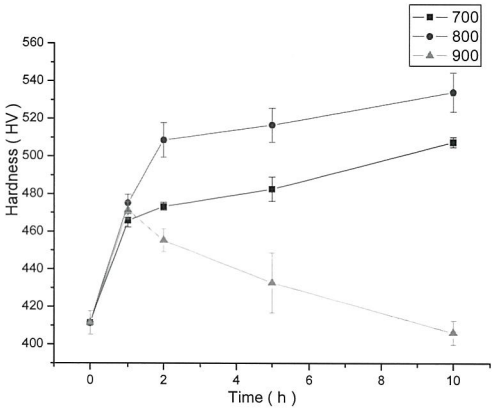

Fig. 2 The aging curves of the tested alloy at 700, 800, and 900℃.

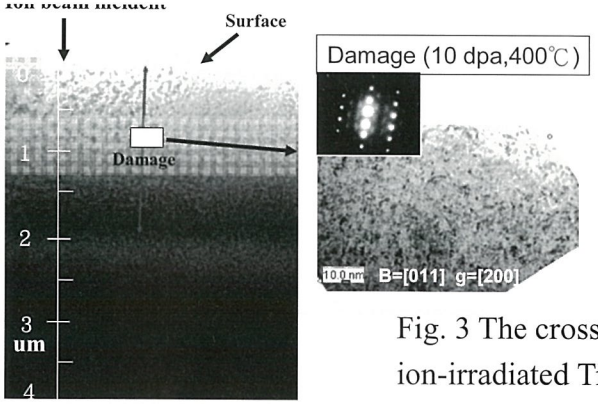

Fig. 3 The cross-sectional TEM bright field image of the single ion-irradiated $Ti_{0.5}CrCo_{1.5}FeNi_{1.5}$. (400℃, 10 dpa)

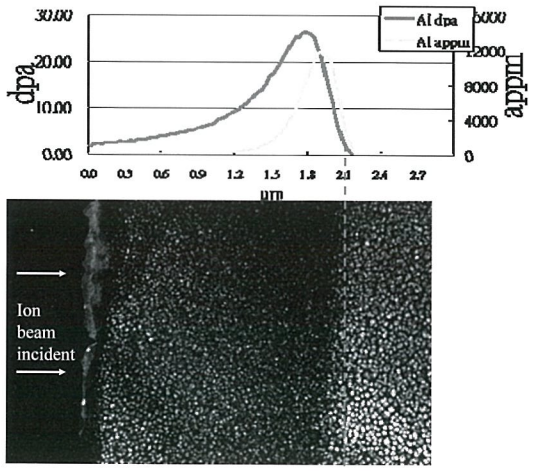

Fig. 4 The cross-sectional TEM dark field image in the single ion-irradiated $Ti_{0.5}CrCo_{1.5}FeNi_{1.5}$. (500℃, 10 dpa) and the corresponding damage profile with respect to the depth. The dash line indicates the maximum depth the ion beam can reach. The bright spots are the γ' phase.

1. J-W Yeh, S-K Chen, S-J Lin, J-Y Gan, T-S Chin, T-T Shun, C-H Tsau, and S-Y Chang, *Adv. Eng. Mater.* **5** (2004) 299-303

M-O-6: DIRECT CORRELCTION OF In/Ga INTER… MIXING WITH PHTOTLUMINESCENCE IN InAs/GaAs QUA… NTUM DOTS BY ENERGY FILTER TRANSMISSION ELECTRO… N MICROSCOPY

CHUNG, Hung-Chin[a](鍾鴻欽), LAI, Yi-Feng[a](賴益鋒), LIU, Chu… n-Pu[a](劉全璞), LAI, Yen-Lin[a](賴彥霖), FANG, Yu Ching[b](方玉清), HSU, L… i[b](徐立), and TANG, Shiang-Feng[b](湯相鋒)

[a]Department of Materials Science and Engineering and Center for … Technology, National Cheng Kung University, Tainan, Taiwan 701 … Micro/nano Science and
[b]Materials & Electro-Optics Research Division, Chung-Shan I… stitute of Science & Technology, Tao-Yuan, Taiwan

InAs quantum dots (QDs) system has been one of the most stu… died systems, however, dot morphology and composition tend to be modified in post-g… rowth process through interdiffusion and has not completely understood yet [1,2]. The… refore, we attempt to investigates shape and composition profiles of both buried and surfa… ce InAs/GaAs quantum dots (QDs) by combining three window and spectrum imagin… g (SI) methods with energy filter transmission electron microscopy (EFTEM). The QDs w… ere grown by molecular beam epitaxy via S-K growth mode. Fig.1. shows a cross-sectional … dark-field TEM image using two-beam (g 400) condition. The typical lateral sizes of the … ncapped InAs QDs are between 15 and 20 nm, which is in good agreement with those obtaine… d from plan-view TEM images, and their height is about 8 nm. By contrast, the capped InAs … QDs are shorter. Fig.2. shows the EFTEM elemental maps from the InAs/GaAs heterostruc… tures by three-window technique, where the contrast is related to elemental variations. Hov… vever, the In elemental signal was only clearly observed for the uncapped InAs layer, a… s shown in Fig.2. (b), suggesting that In has diffused into the neighboring GaAs layer. The… present work suggests that In/Ga intermixing and truncated pyramid shape represent the strai… n-relief mechanisms for the capped dots. Moreover, asymmetric photoluminescence was obs… served from the buried InAs QDs, which is attributed to the confinement effect of the pure … InAs QDs for the main emission and the strain-driven In/Ga intermixing between the QDs a… nd the matrix layer for the side peak. The significant blue-shift in the main emission coincide… s with a calculation by taking the dot height from the Indium map. These results prove that th… e photoluminescence of the buried InAs dots is the result of In/Ga intermixing during post-grow… vth.

References

[1] H. Y. Liu et al, J. Appl. Phys., 98(2005) 083516
[2] H. S. Lee et al., J. Appl. Phys., 91(2002) 5195

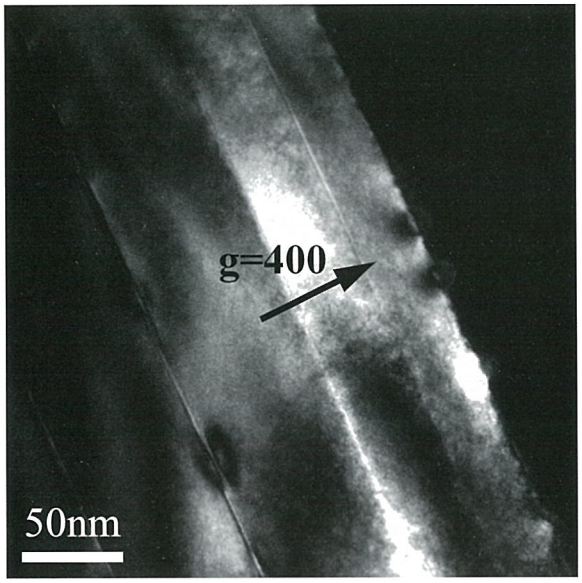

Fig.1. Cross-sectional dark-field (g=400) TEM image of 1.75 BLs InAs/GaAs QDs.

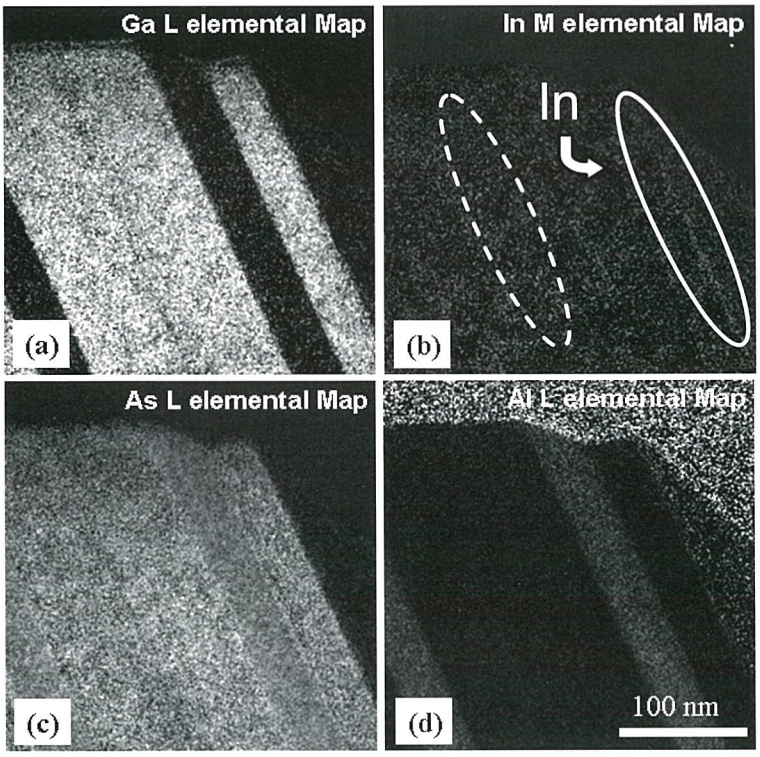

Fig.2. EFTEM elemental maps of the InAs/GaAs specimen: (a) Ga (L_{23}), (b) In (M_{45}), (c) As (L_{23}), (d) Al (L_{23}).

B-O-1: GOLD NANOPARTICLES AND CELLS UNDER THE MICROSCOPES

WANG, Chang-Hai (王長海)[a]; HUA, Tzu-En (華子恩)[a,b]; LENG Wei-Hua (冷偉華)[a]; LEE Cheng-Feng (李政峰)[a]; LIU, Chi-Jen (劉啓人)[a] and HWU Yeu-Kuang (胡宇光)[a, c, d]

[a] Institute of Physics, Academia Sinica, Nankang, Taipei 115, Taiwan.

[b] School of Life Science, National Tsing Hua University, Hsinchu 300, Taiwan.

[c] Department of Engineering and System Science, National Tsing Hua University, Hsinchu 300, Taiwan

[d] Institute of Opto-Electronics Sciences, National Taiwan Ocean University, Keelung 202, Taiwan

Gold nanoparticles have played pivotal roles in emerging novel biomedical nanotechnology. Colloidal gold involves in numerous fields including bio-sensor and disease diagnosis and therapy such as cancer. A fundamental understanding of interactions between gold nanoparticls and cells is essential to enable their functionality. We investigated the cellular uptake and immobilization of synchrotron x-ray derived 15 nm-gold nanoparticles on EMT-6 cells by confocal fluorescence microscope and transmission electron microscope. The size and morphology of gold nanoparticless were observed by TEM (Fig. 1A). Upon loading of gold nanopartticles for 48 hrs, gold nanoparticles were found as clusters and located within the intercellular matrix, as shown in Fig. 1B. It was also noted that the gold nanoparticles formed larger clusters (Fig. 1C) even though individual gold particles can also be differentiated with original size (Fig. 1D). Occasionally gold clusters immobilized within cytoplasm can be observed. As described in Fig. 1E, some gold clusters were internalized while others (arrow) were experiencing cellular uptake. The track of internalized gold nanoparticles towards perinuclear region was shown in Fig. 1F. TEM data indicated that unmodified nanoparticles can penetrate into the EMT cells, even though the amount of cellular uptake is small. This observation is consistent with the absence of cytotoxicty.

References

[1] G. F. Paciotti, L. Myer, D. Weinreich, D. Goia, N. Pavel, R. Mclaughlin, L. Tamarkin Drug Deliv. 11(2004)169

[2] J. F. Hainfeld, D. N. Slatkin, H. M. Smilowitz, Phys. Med. Biol. 49(2004)N309

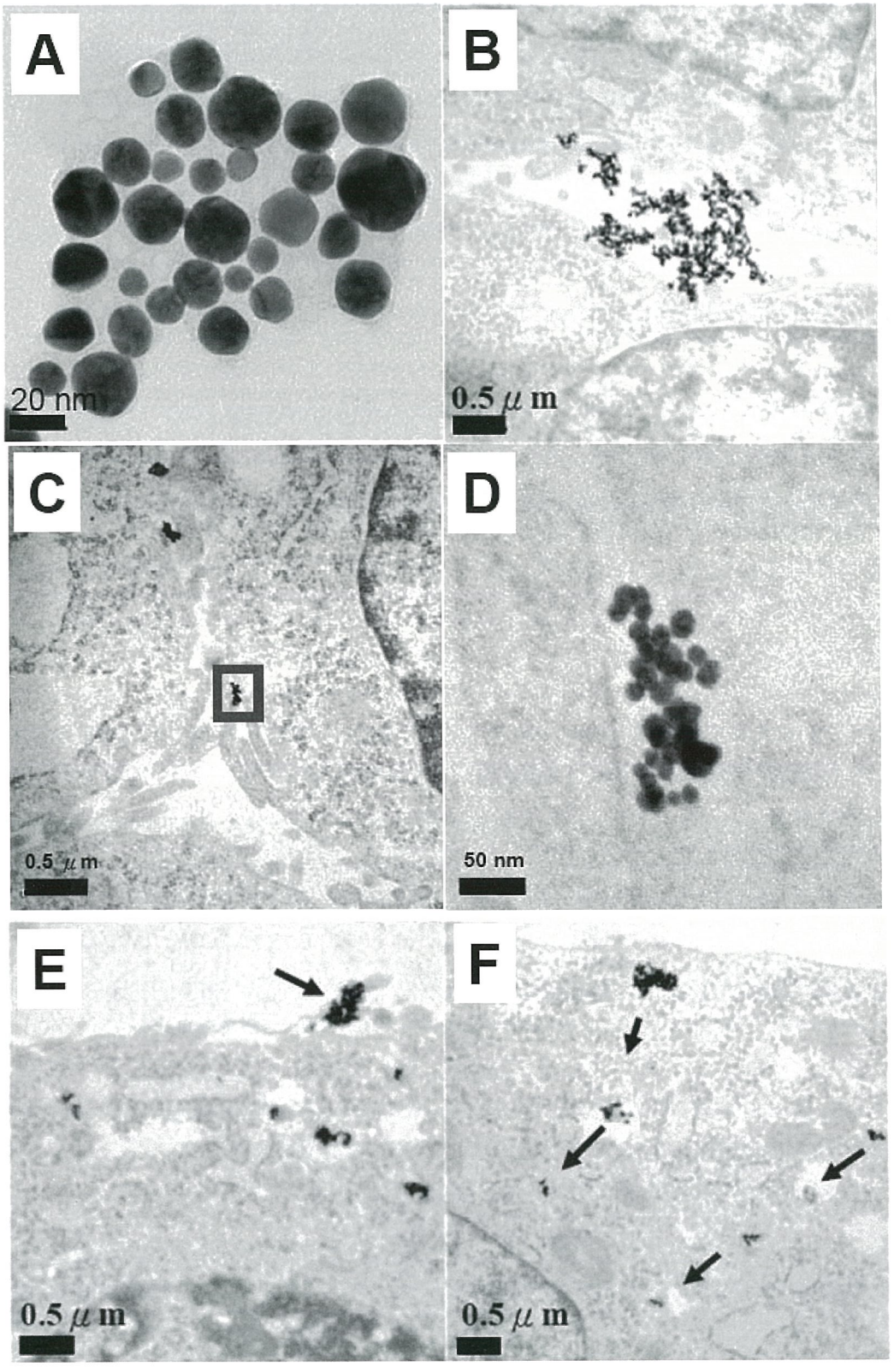
A
20 nm
B
0.5 μ m
C
0.5 μ m
D
50 nm
E
0.5 μ m
F
0.5 μ m

B-O-2: THE BIOLOGICAL APPLICATION OF SYNCHROTRON RADIATION-BASED FOURIER TRANSFORM MICROSPECTROSCOPY

LEE,Yao-Chang (李耀昌) *; HUANG, Pei-Yu 黃佩瑜) and CHEN, Ching-Iue (陳慶曰)
National Synchrotron Radiation Research Center, Hsinchu, Taiwan

Synchrotron-radiation-based Fourier transform infrared (SR-FTIR) microspectroscopy is a newly emerging bioanalytical and imaging tool. The advantage of infrared synchrotron radiation is high throughput at high spatial resolution compared to a conventional thermal source. And the beam size of the radiation after employing 32X confocal Cassegrain objective is about 10 × 13 μm^2 as shown in the Fig. 1(A), however, the conventional infrared light source is about 50 × 30 μm^2 as shown in the Fig. 1(B). SR-FTIR microspectroscopy is the combination of FT-IR microspectroscopy and high brightness infrared synchrotron radiation produces the highest signal-to-noise ratio spectrum with ultrahigh spatial resolution as fine as 8 um.

This unique technique provides mid-infrared spectra based on the vibrations of the nuclei of molecule, and the vibration frequencies of chemical component utilized for production of chemical images according to their characteristic frequencies for indicating each component to the exclusion of others within the sample. Thus it enables researchers to locate, identify, and track specific chemical events within an individual biological cell. Besides, Mid-IR photons are too low in energy (0.05-0.5 eV) to either break bonds or to cause ionization.

In this study, human scalp hair sections, malignant human colorectal tissue section and butterfly wing scale were investigated utilizing reflection detection at lateral resolution of 10 μm. The end result is two dimension infrared spectral images of the sample, enabling constituents and composition to be visualized easily, especially for protein, lipid, carbohydrate, and PO_2^- residual of DNA as shown in the Fig. 2.

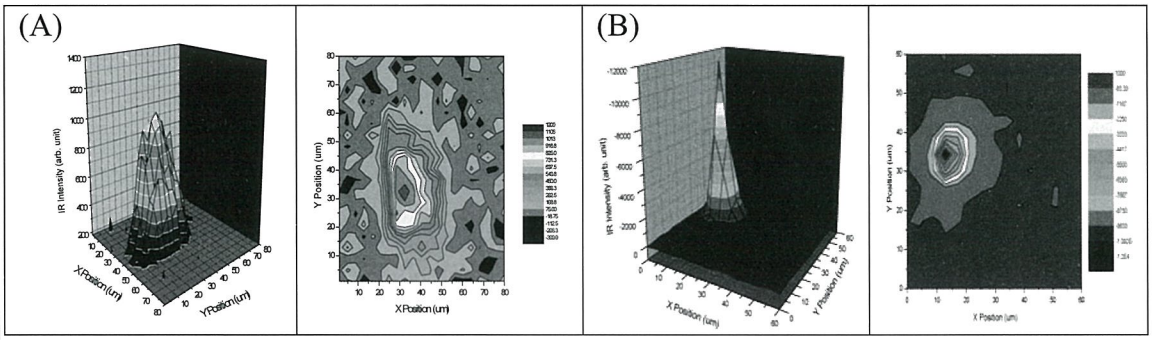

Fig.1. The beam profile of the focused IR beam is mapped by the 5 um pinhole diameter in transmission and the step size of the mapping is 4 μm. (A) The focused beam size of Globar source is around region of 50×30 μm^2. (B) The 2D beam size of the infrared synchrotron radiation is around region of 10×13 μm^2.

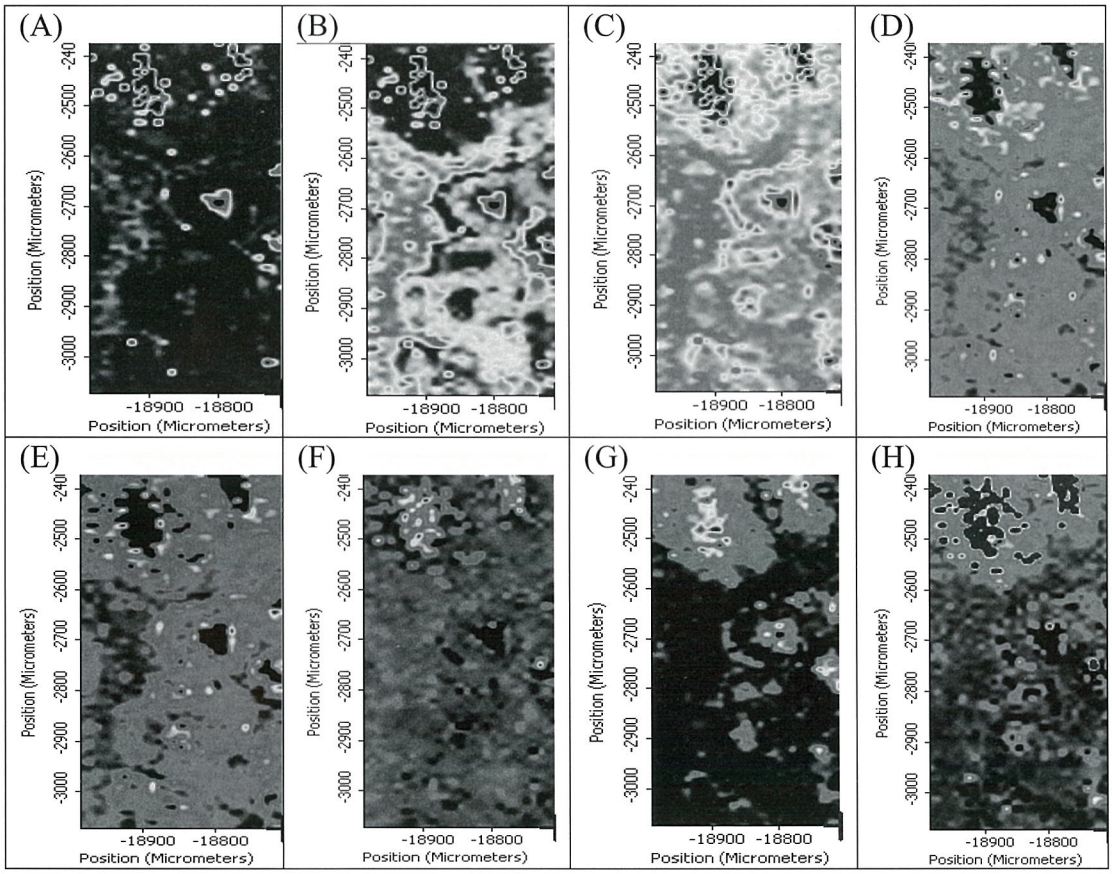

Fig. 2 The functional group map of the deparaffinized colon section of characteristic bands of (A) amide I at 1650 cm^{-1}, (B) amide I at 1638 cm^{-1}, (C) amide II at 1550 cm^{-1}, (D) CH_2 bending at 1467 cm^{-1}, (E), CH_3 bending at 1380 cm^{-1}, (F) ν_{as} PO_2^- (DNA) at 1240 cm^{-1}, and (G) ν_s PO_2^- (DNA) at 1080 cm^{-1}(H) glycogen at 1030 cm^{-1}

ALING MECHANISM UNDERLYING THE GIOGENIC EFFECT OF β-LAPACHONE

NG, Hsiu-Ni (龔秀妮)[b]; KE, Ying-Ru (柯穎如)[a]; and LU, Kuo-Shyan (盧國賢)[b]

gy, School of Medicine, National Yang-Ming University, rtment of Anatomy and Cell Biology, College of ty, Taipei 100, Taiwan.

tial process in tumor development, it is conceivable that may block tumor growth. β-Lapachone ho-[1,2-b]pyran-5,6-dione), a natural product extracted *ellanedae*), has been demonstrated to possess anticancer pachone can induce endothelial cell death or has an ar. In this study we investigated the *in vitro* effect of ncluding human vascular endothelial cell line, EAhy926 thelial cells (HUVEC). Our results revealed that (1) the itochondria membrane potential (MMP) decreased, and l, during β-lapachone-induced endothelial cell death; (2) y β-lapachone was attenuated by treatment with calpain he intracellular calcium chelator, BAPTA, but not the nk, (3) addition of nitric oxide (NO) downregulated the on and protected the cells from apoptosis by blocking the crease and (4) exogenous NO protects endothelial cells apachone, but not the anti-angiogenic effect. From all the) NO/cGMP is an signaling pathway underlying the endothelial cell death, (ii) calcium is another signaling hondrial membrane potential, and activation of the death hone may have potential as an anti-angiogenic drug.

ncol., 2005, (26) 1017
urr. Cancer Drug Targets. 2002, (2) 227.

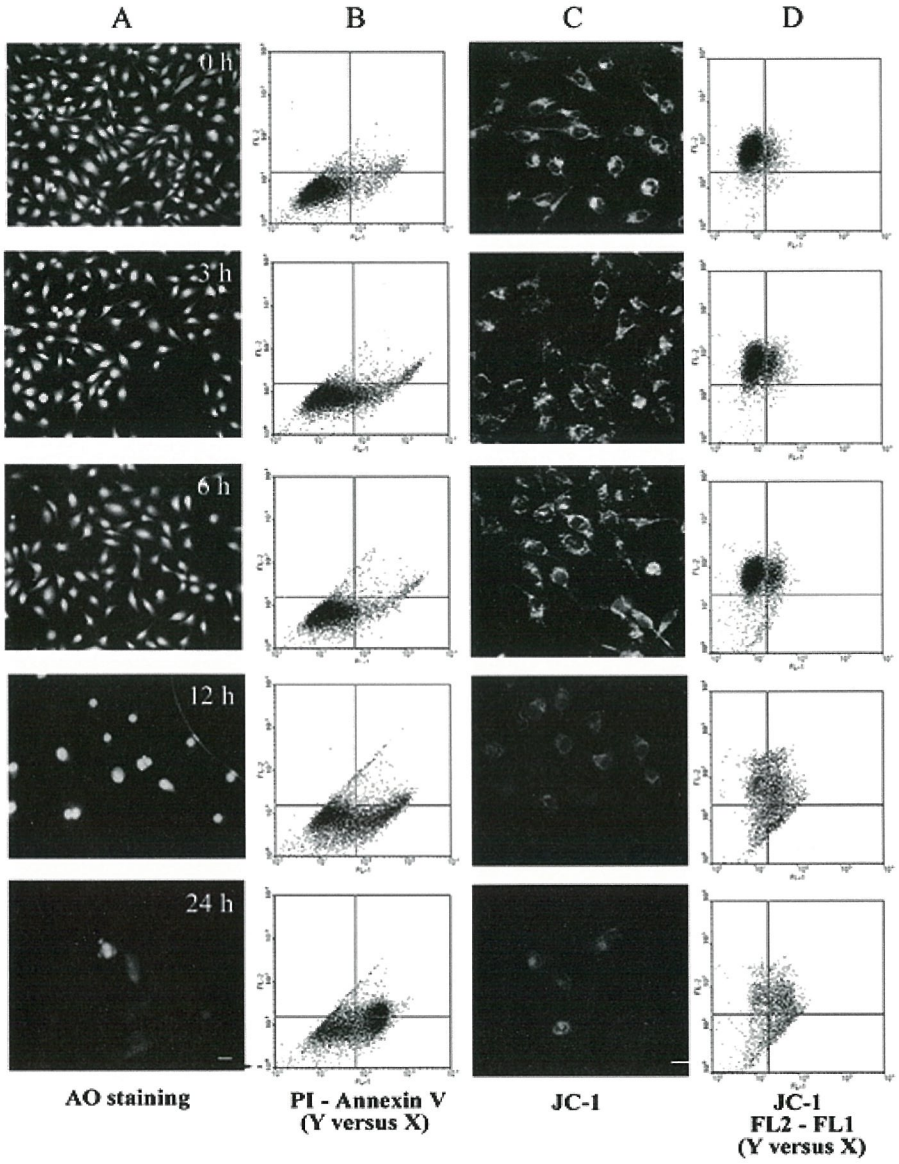

Fig. 1 **β-Lapachone induces apoptotic cell death of human endothelial cells.** (A) EAhy926 cells were treated with 2 μM β-lapachone for 0-24 h, then fixed, stained with acridine orange, and examined on a Zeiss confocal fluorescence microscope. (B) EAhy926 cells treated with 2 μM β-lapachone for 0-24 h, were stained with Annexin V Reagent and PI and analyzed by FACScan flow cytometry. (C and D) Untreated or β-lapachone-treated cells were stained with JC-1 dye for mitochondrial membrane potential measurement, then observed under a Zeiss confocal fluorescence microscope or analyzed by FACScan flow cytometry. The data are shown as dot plots of JC-1 red fluorescence against JC-1 green fluorescence.

B-O-4: EFFECTS OF EMBEDDING MEDIA AND DIVALENT IONS ON THE STRUCTURE OF *EPINEPHELUS MALABARICUS* EGGS FOR TEM EXAMINATION

Kao, Chao-Fu (高肇孚) and Yang, Jui-Sen (楊瑞森)
Institute of Marine Biology, National Taiwan Ocean University, keeling, Taiwan

The eggs of *Epinephelus malabaricus* were used for studing the preparation method of TEM specimens. Three embedding media including Spurr's medium, glutaraldehyde-carbohydrazide(GACH) and glycol methacrylate(GMA) water soluble embedding media were tested for the fish egg embedding. The effects of Spurr's medium, GACH, GMA and divalent ions as magnesium and calcium on fish egg structure during embedding for TEM specimens were sdudied. In dehydration no significant difference in the effects on egg structure between with ethanol and acetone was found. Divalent ions in fixatives partially prevented the eggs from shrinkage and breaking although magnesium ions were better than calcium ions. GACH was a good embedding medium for fish eggs. Fixation with divalent ion addition and embedding with GACH was an efficient method for preparing egg TEM specimens. A suitable method for preparing fish eggs needed forward studies.

References

[1] Dodge, J. T. andC. Mitchel, 1963. Arch. *Biochem. biophys*. 100 - 119.
[2] Rosenberg, M., Part, L. P. , and Lesko, JR.1960, *Ultrastructure Research 4*, 298.
[3] Spurr, A. R. 1969. A low-viscosity epoxy resin embedding medium for electron microscopy *J. Ultrastruct*. Res. 26:31.

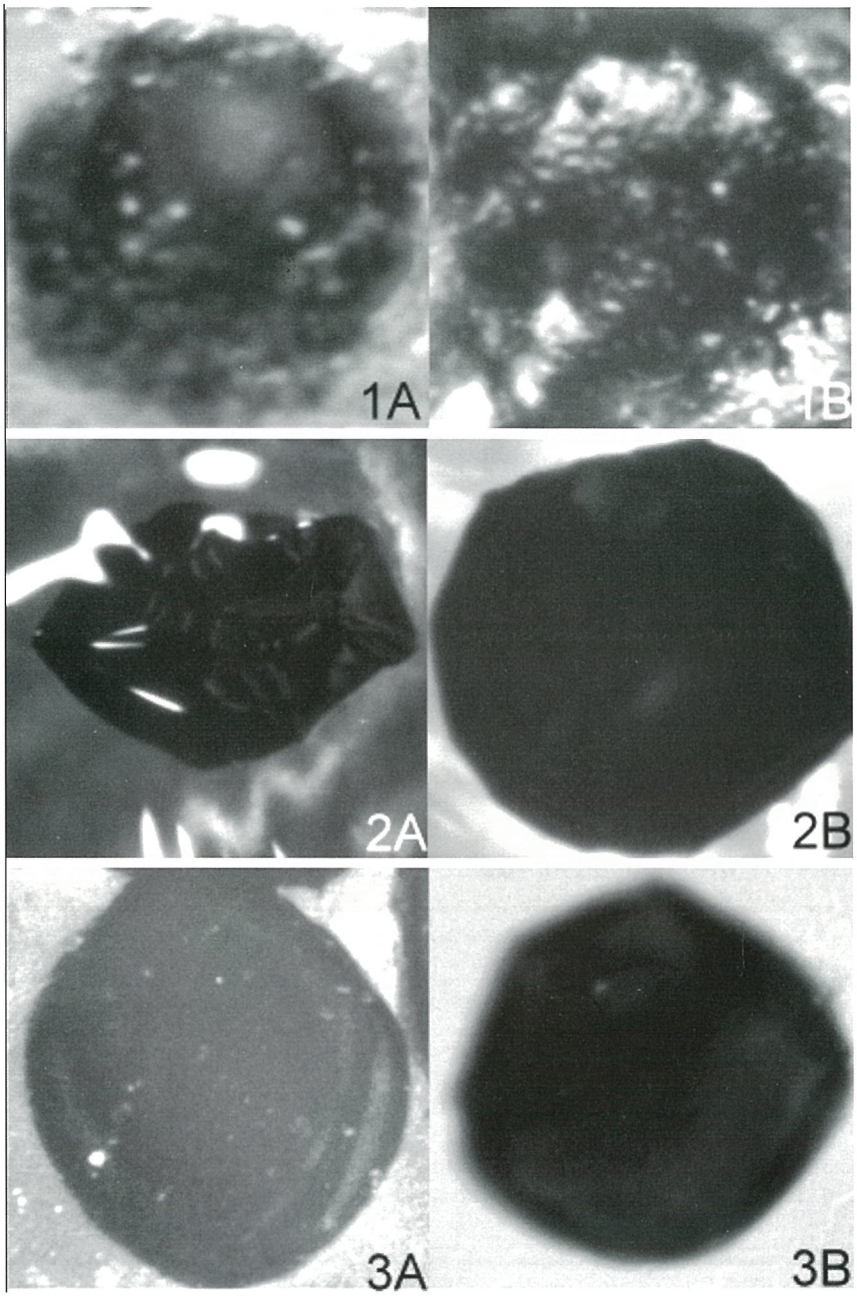

Fig.1.*Epinephelus malabaricus* eggs embedded with Spurr's media without(A)and with(B)$CaCl_2$ addition

Fig.2.*Epinephelus malabaricus* eggs embedded with glutaraldehyde-carbohydraide(GACH) without(A)and with(B)$CaCl_2$ addition

Fig.3.*Epinephelus malabaricus* eggs embedded with Glycol methacrylate(GMA) without(A)and with(B)$CaCl_2$ addition

B-O-5: THE ANATOMICAL CHARACTERISTICS OF *DENDROCALAMUS GIGANTEUS* MUNRO

KUO-HUANG, Ling-Long (黃玲瓏)[1]; HUANG, Yan-San (黃彥三)[2] ; CHEN, Shin-Shin (陳欣欣)[2] and CHEN, Shiang-Jiuun (陳香君)[1].

[1] Department of Life Science, Institute of Ecology and Evolutionary, National Taiwan University, Taipei, Taiwan.
[2] Division of Forest Utilization, Taiwan Forestry Research Institute, Taipei, Taiwan.

The growth of the lateral thickening in the woody monocots is not so well understood as that in the woody dicotyledons, partly because of the large variation of the patterns. The measurement of growth stress on rattans and palm trunks indicated that the distribution of growth stress was different and more complicate as those of the soft and hard woods [1]. The growth of hallow, flexible, and woody bamboo culms is very fast. On giant bamboo, *Dendrocalamus giganteus*, growth stresses exist on the surface and the bamboo tissues of culms. The accumulation of growth stress in the woody plants is an unavoidable result of physiological adjustment during growth. However, the highly variable properties of bamboo present the problems in processing and utilization of the culms. The aim of this study is to examine the anatomical characteristics of the culms of *D. giganteus* during the growth and development. The related trends of variation in growth strains are tested and then discussed.

In *D. giganteus*, the major anatomical character of the culms is the numerous vascular bundles scattering inside the ground tissue (Figs. 1A, 2A, 3A, 4A). The length of nodes increases from the base to the middle and then decrease to the top. The diameter and thickness of the culms do not change a lot during the growth and development (Figs. 2B-D, 3B-D, 4B-D). However they decrease from the base to the top. The diameter of vascular bundles decreases from the base to the top but increases from the inner to the middle and then decreases to the outer periphery (Figs. 1A-C). The specific gravity of the culms increases during the growth and also increases from the base to the top. The density of vascular bundles increases from the core to the periphery and from the base to the top. The percentages of vascular bundle areas and fiber areas are significantly higher in the outer parts than in the inner parts. The production of stress is influenced by anatomical characteristics of the tissues. The amount of strain varies during the growth and from the base to the top because of the variation in proportion of vascular bundles and the fibers, and the cell wall layers of fibers along these points.

References:

Kuo-Huang, L.-L., Huang, Y.-S. , Chen, S.-S., and Huang, Y.-R.. 2004. Growth stresses and related anatomical characteristics in coconut palm trees. IAWA Journal. 25: 297-310.

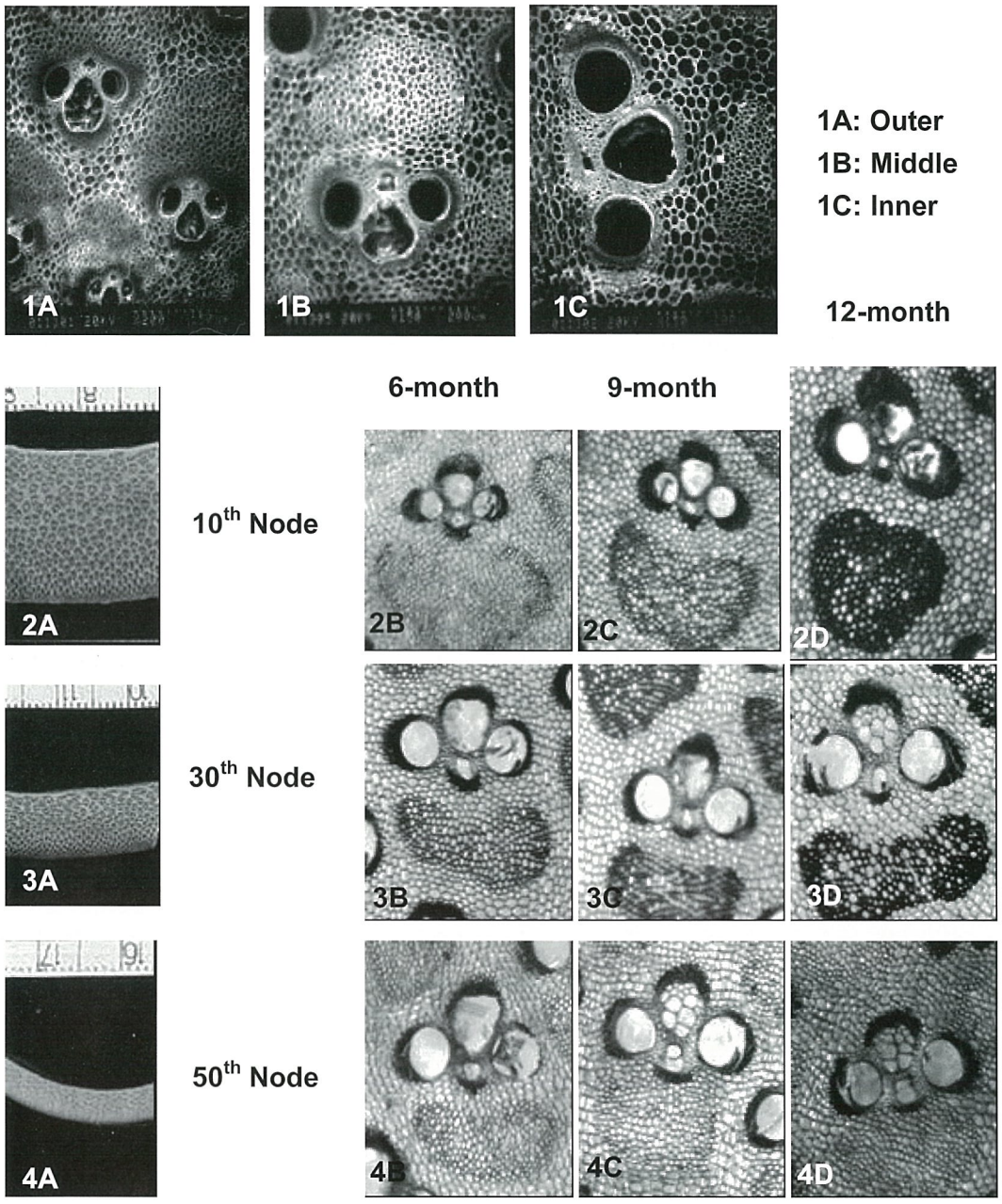

Figures 1-4. The vascular bundles distributed in the ground tissue of culms. (1) Vascular bundle located in A. the outer part, B. the middle part, and C. the inner part. (2) The 10^{th} node of culms, A. part of cross section, B. vascular bundle in the 6-month culms, C. vascular bundle in the 9-month culms, D. vascular bundle in the 12-month culms. (3) The 30^{th} node of culms, A. part of cross section, B. vascular bundle in the 6-month culms, C. vascular bundle in the 9-month culms, D. vascular bundle in the 12-month culms. (4) The 50^{th} node of culms, A. part of cross section, B. vascular bundle in the 6-month culms, C. vascular bundle in the 9-month culms, D. vascular bundle in the 12-month culms.

B-O-6: GALECTIN-1 SUPPORTS IMMORTAL RAT CHONDROCYTE PROLIFERATION ON THE SURFACE OF CHITOSAN-COATED PLGA SCAFFOLD

Chang, Yu-Ying (張鈺嫕)[a]; Chen, Shinn-Jiuun (陳香君)[b]; Tseng, Ching-Shiow (曾清秀)[c]; Tuan, Wei-Cheh (段維杰)[a]; Huang, Rong-Nan (黃榮南)[a]

[a] Department of Life Science and [c]Department of Mechanical Engineering,, National Central Univ. Chung-Li, Taoyuan, Taiwan 32054, ROC

[b] Department of Life Science, College of Life Science, National Taiwan University, Taipei 106, Taiwan

In this study, we investigated the application of Galectin-1 (GAL1) in chitosan-modified PLGA in tissue engineering. The results show that the appearance of chitosan-modified PLGA scaffold was extensively expansive than PLGA after immersing on ddH2O for 2 weeks and water absorption ratio was also 70% higher than PLGA. These results indicated that the chitosan-modified PLGA would be more hydrophilic than PLGA itself. Experimental results also showed that GALl can be efficiently and spontaneously coated on the surface of chitosan-PLGA scaffold to promote the adhesion and proliferation of immortal rat chondrocyte (IRC). IRC adhesion and proliferation on GAL1-chitosan- PLGA scaffold was dose-dependently inhibited by the presence of TDG (the specific inhibitor of GAL1 on CRD) indicating that GAL1 plays a critical role in enhancing IRC cells adhesion on chitosan-PLGA scaffold. IRC growing on GAL-chitosan-PLGA tend to form cell-cell aggregation on the surface, an indicating of tissue differentiation.. In conclusion, the present results suggest that both GAL1 and chitosan play an important role in enhancing IRC cell adhesion and proliferation on PLGA scaffold.

References

[1].D.W. Hutmacher, T. Schantz, I. Zein, J. Biomed. Mater. Res. 55(2001), 203

[2].H. Zhu, J. Ji, , R. Lin, C. Gao, L. Feng, J. Shen,; J. Biomed. Mater. Res. 62 (2002)532

[3] E. P. Moiseeva, E.L. Spring, J.H. Baron, D.P. de Bono, J. Vasc. Res. 36(1999)47

[4]. Y.Y. Chang, S. J. Chen, H. C. Liang, H. W. Sung, C. C. Lin, R. N. Huang, Biomaterials, 25(2004)3603

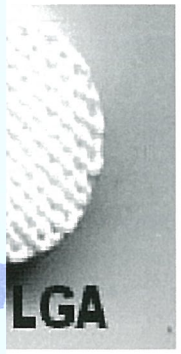

ppearances of PLGA
for 2 h.

itosan-PLGA scaffold.
ld without (A, E) or
M photographed

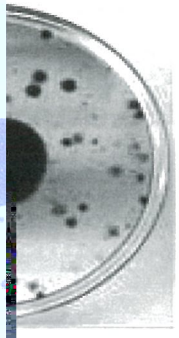

AL1 cells embedded
e plates with or
shed, fixed and

B-O-7: IMMUNOHISTOCHEMICAL AND ULTRASTRUCTURAL STUDIES ON THE VALLATE TASTE BUD IN *DT/DT* AND *DB/DB* MICE

SU, Yu-Jen (蘇昱人); Kung, Hsiu-Ni (龔秀妮); Chang, Chi-Fen (張綺芬);
Lu, Kuo-Shyan (盧國賢)*

Department of Anatomy and Cell Biology, College of Medicine, National Taiwan University, Taipei 100, Taiwan

Recently studies on the taste bud are focused on the neurotransmitters and cell communications [1, 2, 3], but not the morphology, of the taste bud. We reported here the morphological and morphometric studies on two strains of mutant mice, *dt/dt* and *db/db*. The dystonia musculorum *(dt/dt)* is a natural mutant mouse with hereditary sensory neuropathy and results in dystonic movement and severe ataxia after birth. The obese diabetic (*db/db)* mouse, a knock out leptin recptor mutant, displays enhanced neural responses and elevated behavioral preference to sweet stimuli. The sensory function is affected in *dt/dt* mice, and the metabolic activity is disturbed in the *db/db* mice. A comparative study was performed among the wild type, *dt/dt*, and *db/db* mice, to examine the morphology of vallate taste bud at light and electron microscopic level, and distribution and abundance of the PGP-9.5 immunoreactivity in the taste buds of the vallate papilla. Morphometry and quantitative analysis on the distribution of taste buds and their gustatory nerve fibers are also demonstrated.

Compared with wild type mice, the size of vallate papillae is much smaller and the number of taste buds decreased significantly in *dt/dt* mice (94.98±3.1 vs. 58.21±5.12 taste buds/papilla). However, the morphology of vallate papilla and the number of its taste buds in *db/db* mice (98.69±5.06 taste buds/papilla) are not apparently different from those of the wild type. The results from the PGP9.5 immunostaining showed that the nerve innervation in taste bud cells was significantly reduced in *dt/dt* mice, as compared with wild type and *db/db* mice (Fig. 1). Ultrastructural examination confirms the morphological findings at light microscopic level.

We conclude that the sensory deficiency in the mutant *dt/dt* mice affect the morphology and innervations severely of taste buds, however, the metabolic disturbance of the mutant *db/db* mice does interfere the structure and innervation of the taste buds in the vallate lingual papilla.

References

[1] G.F. Lopez, R.F. Krimm, J Neurobiol. 66 (2006) 1033–1043

[2] R.A. Romanov, O.A. Rogachevskaja, M.F. Bystrova, P. Jiang, R.F. Margolskee, S.S. Kolesnikov, EMBO Journal, 26 (2007) 657–667

[3] Y.-J. Huang, Y. Maruyama, G. Dvoryanchikov, E. Pereira, N. Chaudhari, S.D. Roper, PNAS, 104 (2007) 6436-6441

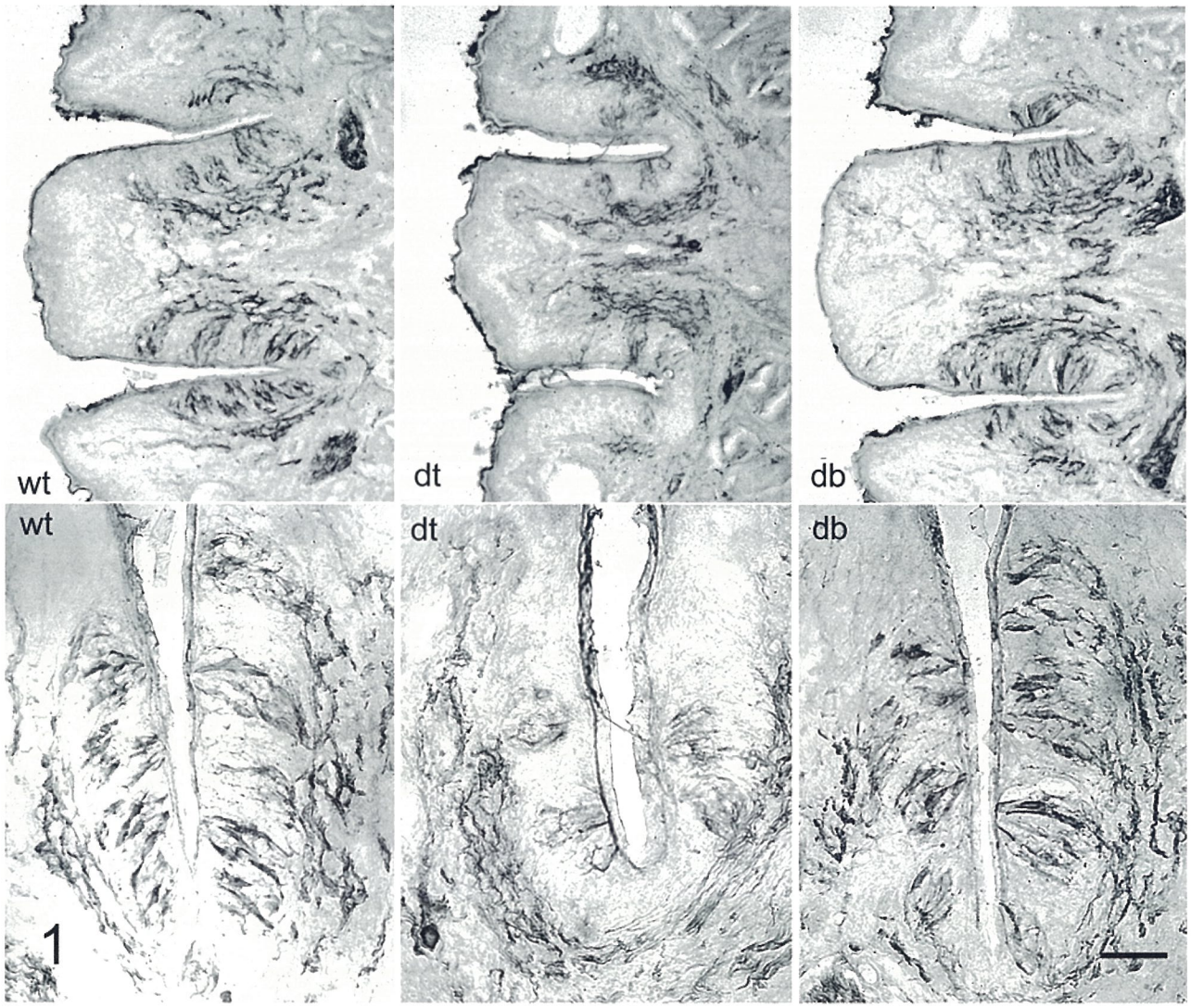

Fig 1. PGP9.5 immunoreactivity of mouse vallate taste bud. wt: wild type (normal control), dt: *dt/dt* mutant mouse, and db: *db/db* mutant mouse. Scale bar = 50 μm.

B-O-8: STATINS INCREASE THROMBOMODULIN EXPRESSION IN HUMAN AORTIC ENDOTHELIAL CELLS WITH OR WITHOUT TUMOR NECROSIS FACTOR-A TREATMENT

HSIEH, Fang-Yu (謝芳瑜)[a]; GUANG, I-I (管奕奕)[a]; WANG, Shu-Huei (王淑慧)[a]; LIN Shing-Jong (林幸榮)[b] ; KU Hung-Hai (古宏海)[c] and CHEN,Yuh-Lien (陳玉怜)[a]

[a] Department of Anatomy and Cell Biology, College of Medicine, National Taiwan University, Taipei 100, Taiwan.

[b] Institute of Clinical Medicine, National Yang-Ming University, Shih-Pai, Taipei 112, Taiwan.

[c] Institute of Anatomy and Cell Biology, National Yang-Ming University, Shih-Pai, Taipei 112, Taiwan.

Statins, 3-hydroxy-3-methylgluataryl coenzyme A reductase inhibitors, not only reduce serum cholesterol but they also improve vascular endothelial function independent of their lipid-lowering effects (1). Expression of functionally active thrombomodulin (TM) on the luminal surface of endothelial cells is critical for vascular thromboresistance (2). We examined the effects of statins on TM expression by human aortic endothelial cells (HAECs) with subsequent tumor necrosis factor-α (TNFα) stimulation and investigated the signaling pathways involved. TNFα treatment attenuated TM expression in HAECs in a time-dependent manner. Statin upregulated TM levels in control and TNFα-treated HAECs (Figs.1, 2). Statins also decreased intercellular adhesion molecule -1 (ICAM-1) expression and the binding of monocytes to TNFα-stimulated HAECs. In TNFα-treated HAECs, statin inhibited Rac1 and Cdc 42 activation and their translocation to the cell membrane. Blocking the transcriptional activation of NF-κB prevented the TNFα-induced downregulation of TM. The statin-induced increase in TM expression in TNFα-treated HAECs was mediated through inhibition of NF-κB activation. These results demonstrated that Statin regulates TM expression by inhibiting the activation of the Rho family proteins, Rac1 and Cdc42, and the transcription factor, NF-κB. The increase in endothelial TM activity in response to statins constitutes a novel pleiotropic (non-lipid-related) effect of this commonly used compound and may be of clinical significance in disorders in which deficient endothelial TM plays a pathophysiological role.

References

[1] S.I. McFarlane, R. Muniyappa, R. Francisco, J.R. Sowers. J Clin Endocrinol Metab. 87(2002)1451

[2] C.T. Esmon. J Thromb Haemost. 1(2003)1343

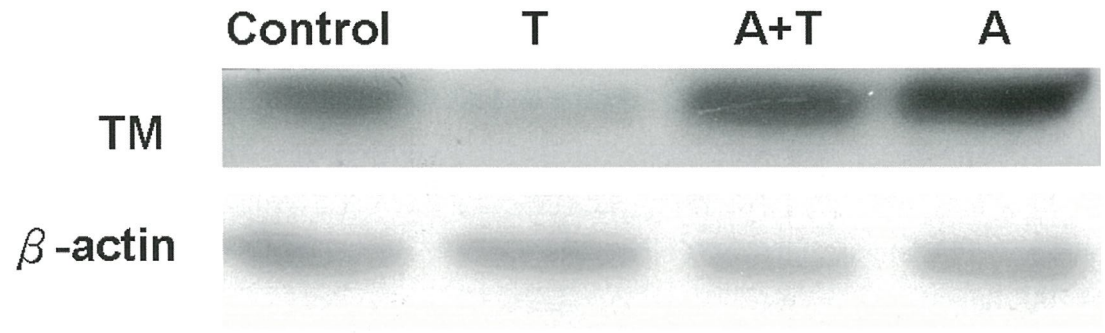

Fig 1. Statin upregulates TM expression in control and TNFα (T)-treated HAECs by Western blotting. HAECs were incubated for 24 h with 10 μM atorvastatin (A), and then the cells incubated with 10 ng/mL of TNFα for 24 h.

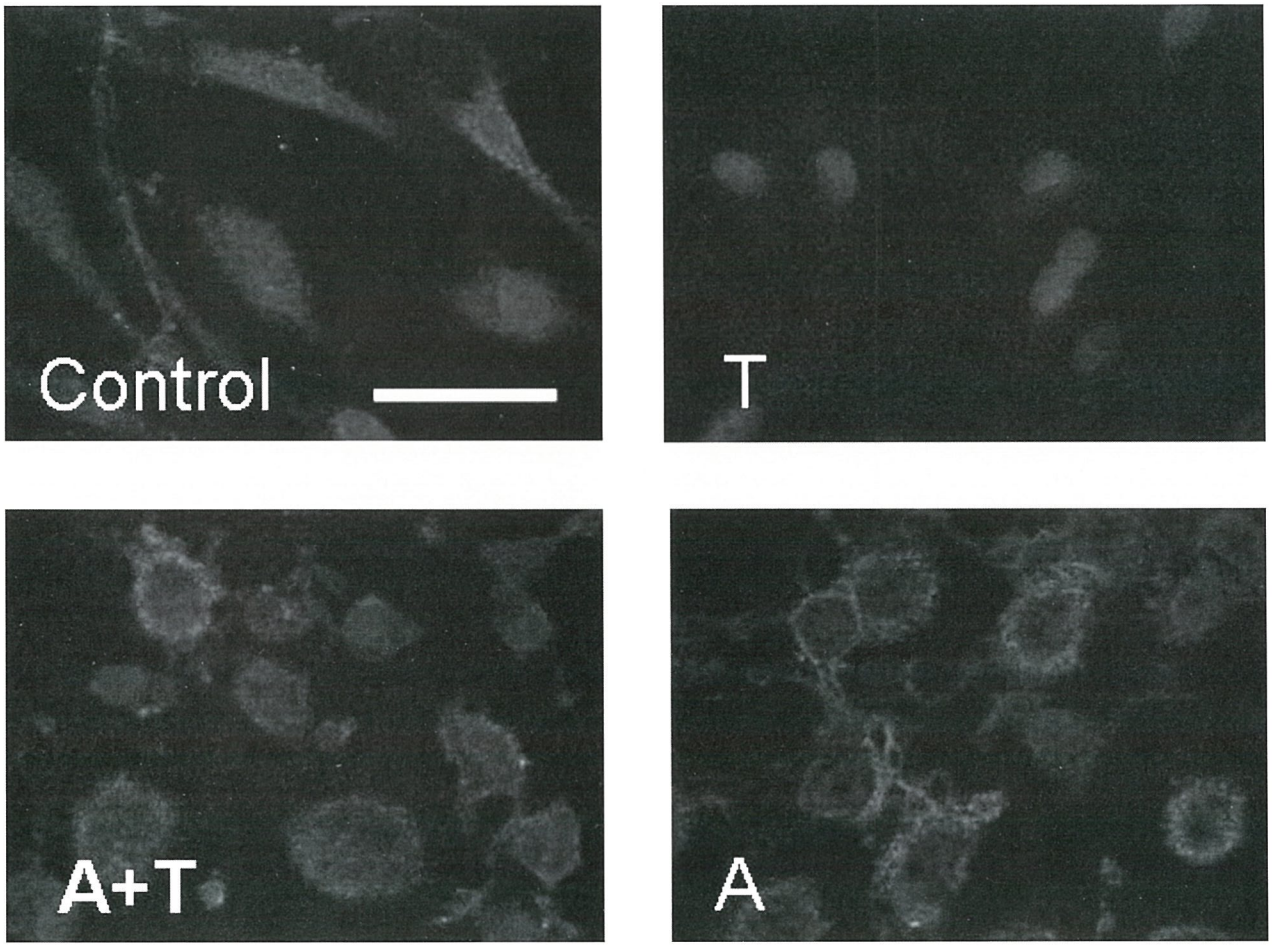

Fig. 2. Confocal microscopic images showing TM expression in control and TNFα (T)-treated HAECs. Distribution of TM was identified with immunofluorescent staining (green color). Scale bar=50 μm

M-P-1: MORPHOLOGY AND DIAMETER CONTROLLED SYNTHESIS OF AG NANOSTRUCTURES WITH A SIMPLE GALVANIC DISPLACEMENT METHOD ON V FOILS

WANG, Chiu-Yen (王秋燕); LU, Ming-Yen (呂明諺) and CHEN, Lih-Juann (陳力俊)

[a]Department of Materials Science and Engineering, National Tsing Hua University, Hsinchu.

High aspect ratio, high yield (> 95 %) and crystalline silver nanowires (NWs) have been prepared with a relatively fast, clean and facile galvanic displacement method on V foils at room temperature.

Figures 1a-c show the SEM images of a variety of Ag nanostructures formed in different concentrations of silver nitrate solution on V foil for 30 min. With the higher concentration (10 mM), the reduced products were plate-like nanodendrites (about 200 nm in thickness). For $AgNO_3$ concentration of 1 mM, the reduced Ag formed a high density of nanowires with more than 100 μm in length and 100 nm in average diameter. Some of the silver particles (30-60 nm) were adsorbed on the nanowire. The naostructures size morphology of winder stairs were formed in a 5 mM silver nitrate solution with size about 150 nm and tens of nanometer at stems and platforms, respectively. An example is shown in figures 1c. The results indicate that the morphology can be tuned via controlling silver concentration. Figure 1d illustrates that the diameter of Ag NWs with reaction temperature could be well-controlled.

The growth of Ag/VO_x core/shell structure includes several steps: (1) conversion of Ag^+(aq) into Ag(s) coinciding with V(s) oxidation to vanadium ion, (2) growth of silver atoms into nanoparticles (NPs), (3) nucleation and growth of Ag NWs extended from the NPs, and (4) V atoms were oxidized to form VO_x at the surface of Ag NWs.

Optical features were studied by UV-visible spectrum. The transverse plasmon mode (at 380 nm) was observed and optical signatures similar to those of bulk silver started to appear, as indicated by a shoulder around 350 nm which could be attributed to the plasmon resonance of bulk silver film. On the other hand, the peak around 410nm was not existed. This observation indicates that the final product synthesized under this condition was silver nanowires, shown in figure 1e.

Different pH values also dramatically influence the growth in the galvanic displacement reaction. The Ag NWs were formed only in solutions with pH values between 4.5 and 3.5. In lower pH solution, huge dendrites of Ag were formed, as shown in figure 1f.

The method is seedless and no external surfactant or polymer as directing agent. The NWs are hundreds of micrometer in length with an average diameter of 20 nm. The diameters of Ag nanowires and morphology of nanostrucrures can be well-controlled by adjusting reaction temperature and silver salt concentration, respectively. The growth mechanism of Ag NWs also has been discussed.

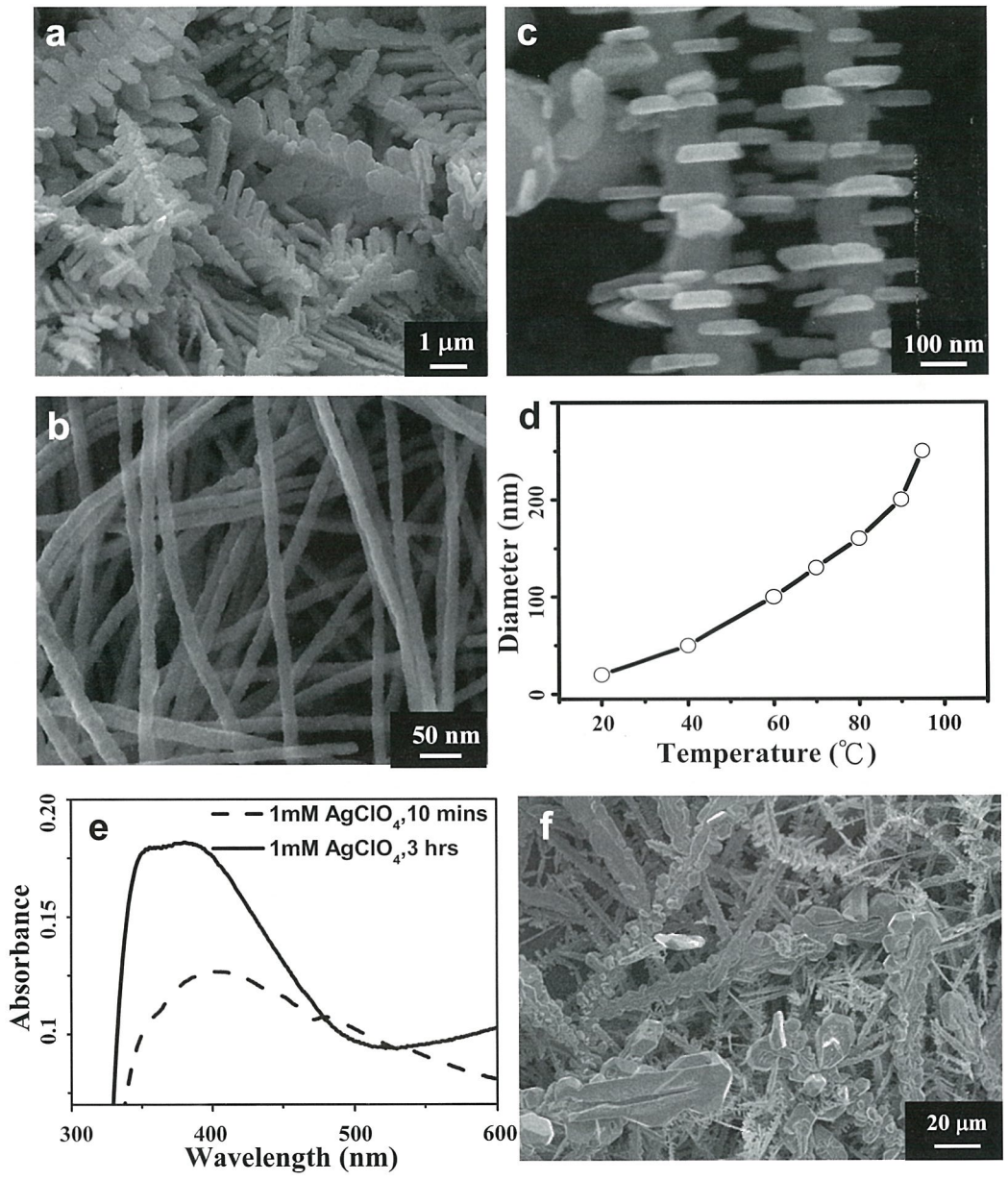

Fig. 1. (a-d) Ag nanostructures and diameter of nanowires are well-controlled by reactant concentration and reaction temperature. (e) Typical UV-visible spectra of Ag nanoparticles and nanowires growth. (f) At low pH value, the morphology of Ag nanostructure is similar to that formed with high reactant concentration.

M-P-2: CONTROLLED GROWTH OF ALIGNED ZNO NANOTOWERS WITH ENHANCED ULTRAVIOLET CATHODOLUMINESCENCE AND FIELD-EMISSION PROPERTIES

CHANG, Yu-Cheng (張育誠) and CHEN, Lih-Juann (陳力俊)

Department of Materials Science and Engineering, National Tsing Hua University, Hsinchu.

Zinc oxide is one of the most promising functional materials owing to its wide direct band gap (3.37 eV) and large exciton bind energy (60 meV). ZnO nanostructures have attracted much attention for its applications in nanodevices such as photodiodes, optical modulator waveguides, ultraviolet laser, photonic crystals, chemical sensors, solar cells and piezo-diode. A novel fabrication technique of aqueous chemical growth (ACG) has been demonstrated to grow ZnO nanostructures and ferric oxide nanorods at low temperature (<100 ℃).

The ability to adopt the non-toxic and bio-friendly reagent to control and to integrate nanostructures as functional 3-D arrays is an important challenge scientists have faced to develop biotechnology and environment. Herein L-ascorbic acid (ascorbic acid for simplicity), which is free from health hazard, has been used to control the morphology of ZnO nanostructures. L-ascorbic acid is a form of ascorbic acid and also called Vitamin C, which is a water-soluble nutrient and essential ingredient for maintaining the human well being. It is used by the body for many purposes. The present study uses appropriate concentration of ascorbic acid and in conjunction with downward growth process to produce very sharp ZnO nanotowers in a short time. The ascorbic acid concentration was varied to modify the degree of lamination in the ZnO nanotowers.

The three kinds of laminated nanotowers with lower than 10 layers, between 10 to 30 layers and more than 30 layers are herein designated as low layer nanotowers (Fig. 1), nanotowers (Fig. 2) and high-rise nanotowers (Fig. 1), respectively. Changing the substrate from ZnO seeds layer to ZnO nanorods layer facilitates the growth of aligned ZnO nanotower arrays. The tight control in alignment, narrowing of tips and degree of lamination of nanostructures is achieved by utilizing the substrate with aligned ZnO nanorods, downward growth method and variation in bio-friendly ascorbic acid in the growth solution. Low turn-on and threshold fields indicate that ZnO nanotowers are promising for the application in field emission microelectronic devices. The ZnO nanotowers exhibit very prominent blue shift (10 nm) of UV emission and almost no green emission attributed to singly ionized oxygen vacancies at room temperature. The enhancement in deep-UV optical properties shall be advantageous in applications for nanoscale light-emitting devices.

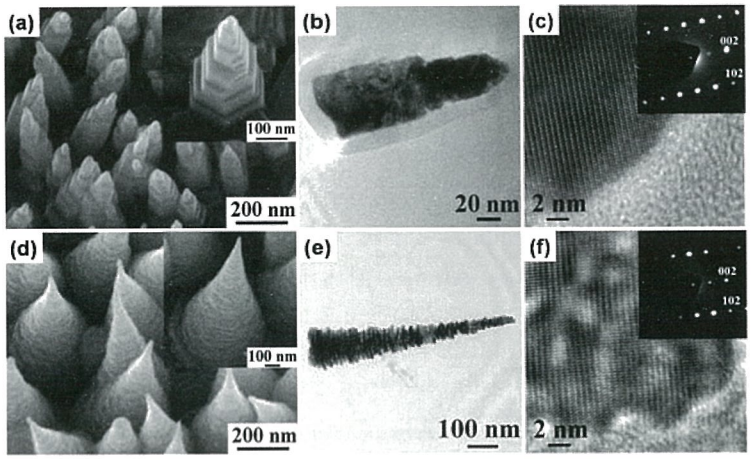

Fig. 1. (a) 20° tilt-view SEM image of the low nanotowers grown on ZnO nanorod layer, inset image is a high magnification SEM image. b) TEM image of a low nanotower in (a). c) HRTEM image and SAED pattern confirming the single-crystallinity of the low nanotower in (b). d) 20° tilt-view SEM image of high-rise nanotowers grown on ZnO nanorod layer, inset image is a high magnification SEM image. e) TEM image of a high-rise nanotower in (d). f) HRTEM image and SAED pattern confirming the single-crystallinity of the high layer nanotower in (e).

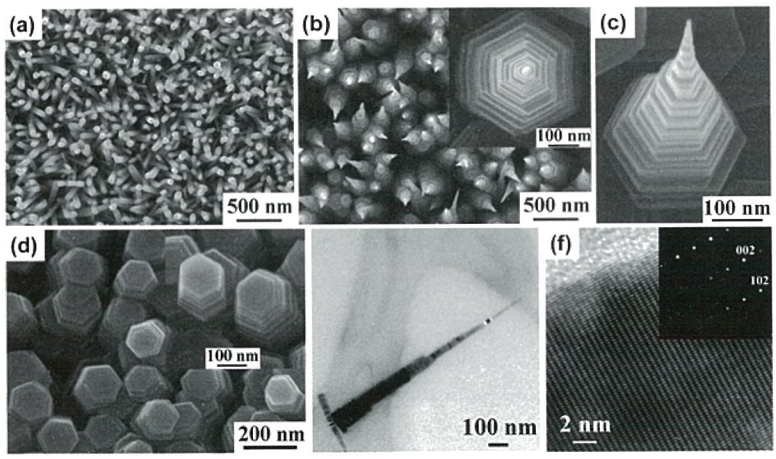

Fig. 2. (a) Top-view SEM image of ZnO nanorods layer grown on Si wafer pre-coated with ZnO seeds film, b) top-view and c) 20° tilt-view SEM images of nanotowers grown on ZnO nanorod layer by the downward growth process. The inset image in (b) is a high magnification SEM image. d) 20° tilt-view SEM image of ZnO nanotowers grown on ZnO nanorod layer by the upward growth process and the inset is a high magnification SEM image. e) TEM image of a ZnO nanotower in (b). f) HRTEM image and corresponding SAED pattern confirming the single-crystallinity of the ZnO nanotower in (e).

M-P-3: AU-FILLED Ga_2O_3 NANOTUBE AND ITS APPLICATION AS HIGH-TEMPERATURE NANOTHERMOMETER

Gong, Nan-Wei (龔南葳); Lu, Ming-Yen (呂明諺); Wang, Chiu-Yen (王秋燕); Chen, Yu (陳瑀) and Chen, Lih-Juann (陳力俊)

Department of Materials Science and Engineering, National Tsing Hua University, Hsin Chu 300, Taiwan

Au-filled β-Ga_2O_3 nanotubes were fabricated through an effective one-step approach. Linear thermal expansion of Au within single crystalline Ga_2O_3 shell was observed through in situ TEM. Since Ga_2O_3 and Au both possess excellent thermal and chemical stability, the structure can be used as a high-temperature nanothermometer up to 1173K within localized region.

The most common types of Au-fillings are shown in figure 1. Au-filled β-Ga_2O_3 nanotubes can be closed at one-end or both-ends. The fillings normally tend to near one end, and in some cases near both ends thus leave a cavity between two segments of Au. To explore the thermal properties of this structure and its possible application as nanothermometer, we used in situ TEM to observe the real time behavior of its thermal activity. We heated the sample from room temperature to 1173K and the structure remained intact. In Fig. 2, it is seen that it exhibits a linear thermal expansion in the range from 773K to 1073K. After the specimen was cooled to room temperature, the fillings retreated to the original position as it was prior to heating. In the calculation of this thermal expansion behavior, we have to take the expansion of Ga_2O_3 nanotube in to consideration. Bulk Au has a linear coefficient of thermal expansion (CTE) of $14\times10^{\square6}(1/K)$. However, in this case the Au filling expressed a CTE of $62.5\times10^{\square6}(1/K)$. The increase in its CTE is attributed to the thermal expansion of outer Ga_2O_3 nanotube (thermal expansion coefficient of Ga_2O_3: $4.6\times10^{\square6}(1/K)$). The expansion distance versus temperature is shown in Fig. 2. By measuring the moving distance intermittently during heating, we can obtain the relationship between distance d (nm) and temperature change to fit the following formula: $T = T_0 + 1.6 \times10^4 \times (d \square d_0) / L_0$, where L_0 is the original length of Au filling and d_0 is the original distance of vacancy within the nanotube both at T_0. Each nanothermometer has a different working range which depends on the vacancy and the original length of Au. For example, the one in Fig. 4 can measure up to 1273K.

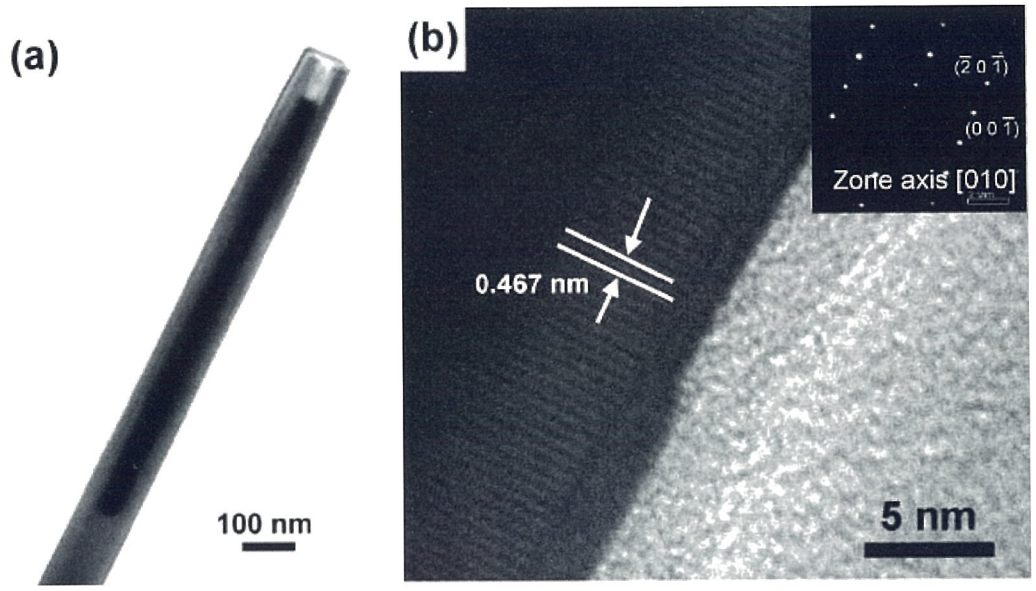

Figure 1. (a) Typical structure of Au-filled β- Ga_2O_3 nanotube. (b) High resolution image of the tube indicates that the β- Ga_2O_3 nanotube is of single-crystal structure.

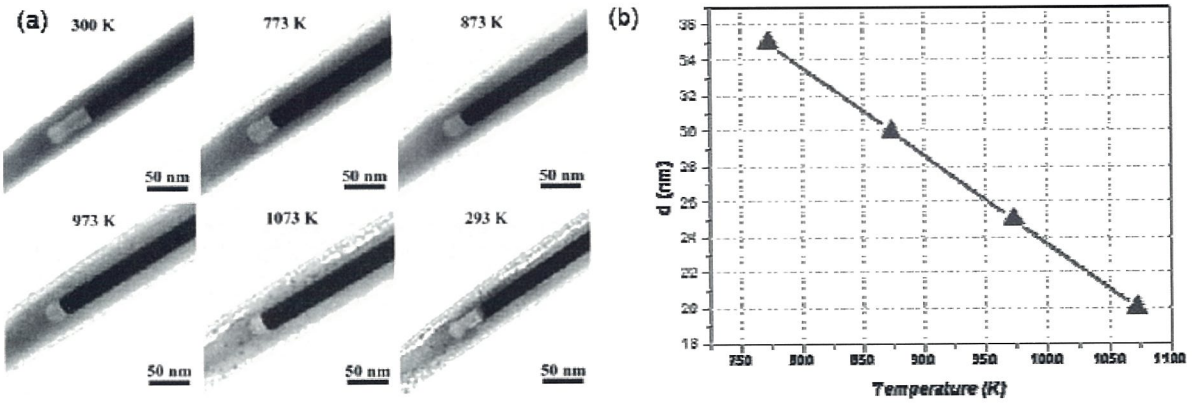

Figure 2. (a) Thermal behavior of Au-filled β- Ga_2O_3 nanotube. A linear thermal expansion can be observed in the range from 773K to 1073K. After the specimen was cooled to room temperature, the fillings retreated to the original position as it was prior to heating. (b) Relationship between distance d (nm) and temperature change is linear and can be expressed with the following formula:

$$T = T_0 + 1.6 \times 10^4 \times (d - d_0) / L_0 .$$

M-P-4: PREPARATION OF 3-D ORDERED POROUS GA2O3 FILMS SYNTHESIZED VIA COLLOIDAL TEMPLATES

WU, Han-Wei (吳漢威); TSAI, Cho-Jen (蔡哲正) and CHEN, Lih-Juann (陳力俊)
Department of Materials Science and Engineering, National Tsing-Hua University, Hsinchu 300, Taiwan.

Materials with two-dimensional (2D) and three-dimensional (3D) ordered structures have attracted considerable attention over the past decade. These structures have an orderly arrangement and a high specific surface area, and they have been found to be promising photonic crystals, advanced catalysts, biosensors, thermal insulation material, membranes, and a variety of other current and future applications [1,2]. Here, highly ordered porous Ga_2O_3 films were prepared on silicon substrates using gallium nitrate hydrate and polystyrene latex spheres as colloidal templates via a facile annealing process in air.

Figures 1(a)-(c) show plan-view SEM images for 2D Ga_2O_3 ordered pore arrays after removal of the templates with different precursor concentrations (0.02, 0.06, and 0.15 M) and heated at 900 °C for 4 h. All of them exhibit a well-defined honeycomb structures. The morphologies of the ordered pore arrays are determined by solution concentration, which is controllable. Figure 1(d) shows the multilayered FCC Ga_2O_3 ordered porous films. The pores are highly ordered in a hexagonal array. The holes connecting the pores are clearly visible and confirm the three dimensional ordering of the structure. In some case, large-area square symmetry of ordered porous Ga_2O_3 films was synthesized as shown in Fig. 1(e).

Figures 2(a)-(d) show the cross-section images of multilayer Ga_2O_3 ordered porous films with 5, 10, 15 and 20 μl of polystyrene (PS) spheres in aqueous solution, respectively. The images show that 3, 5, 8, and 11 layers of Ga_2O_3 ordered porous films are formed. Increase of layers of Ga_2O_3 ordered porous films with volume of PS spheres aqueous solution is clearly observed. Figures 2(e)-(g) show the SEM images of multilayer Ga_2O_3 ordered porous films after removal of the templates with different precursor concentrations (0.02, 0.06, and 0.15 M) by annealing at 900 °C for 4 h in air. The results indicated that the higher concentration of $Ga(NO_3)_{3(aq)}$ solution lead to the thicker skeleton and lower surface-to-volume ratio.

The sensing properties of 3-D ordered porous Ga_2O_3 structure on silicon substrates were investigated. The 3-D ordered porous structure has a high specific surface area and promotes the gas sensitivity of Ga_2O_3 in detecting NO_2 at 200 °C. This ordered porous structure is promising for sensing, photonic and optoelectronic applications.

References

[1] S. H. Park and Younan Xia, Adv. Mater. 10 (1998) 1045.
[2] Judith E. G. J. Wijnhoven and Willem L. Vos, Science 281(1998) 802.

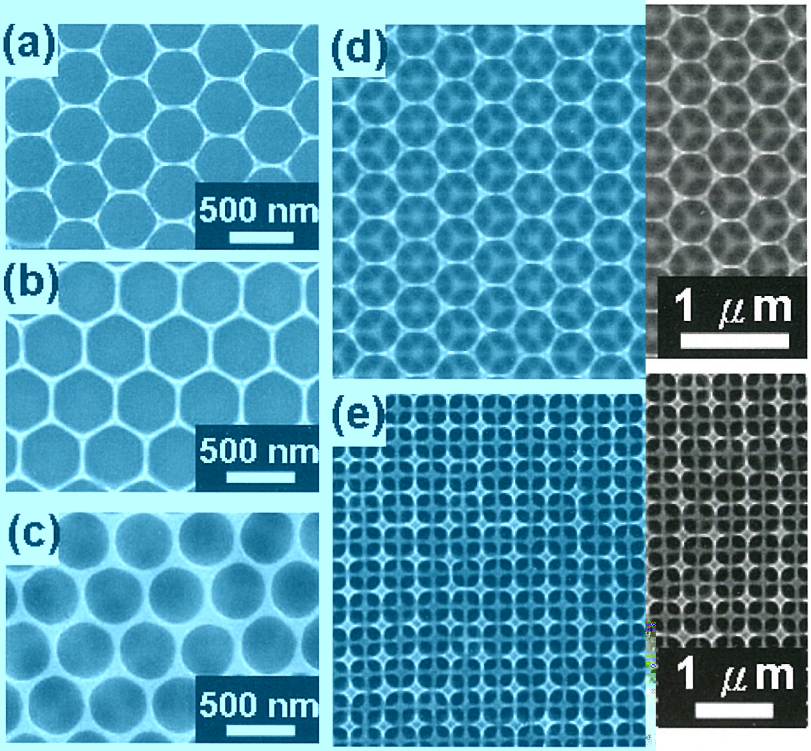

Fig. 1(a)-(c) Plan-view SEM images for Ga_2O_3 ordered pore array
precursor solution; (d) and (e) Plan-view SEM images for large-area

with 0.02, 0.06, and 0.15 M
Ga_2O_3 ordered porous films.

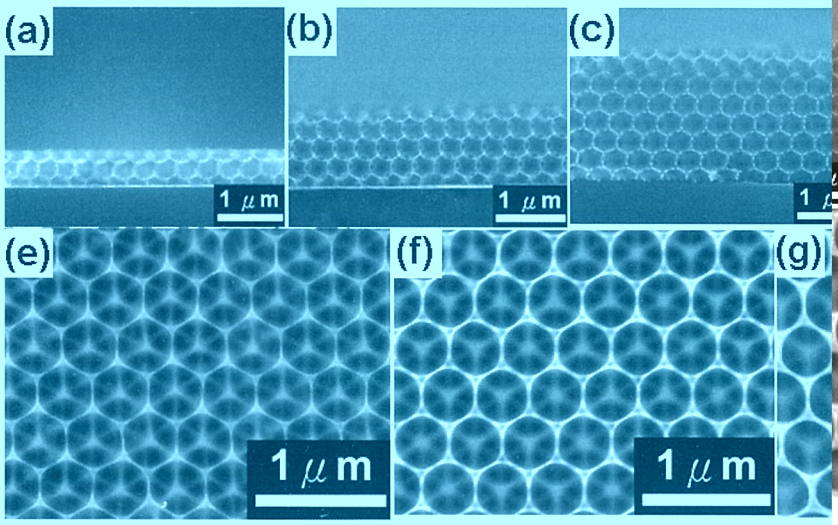

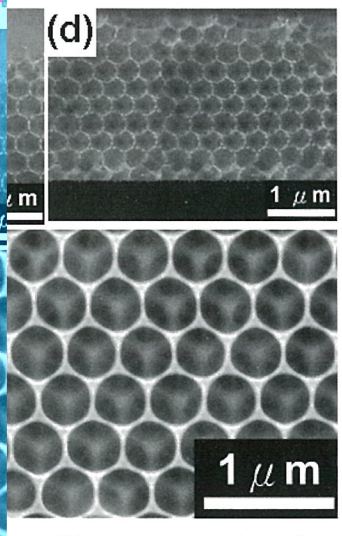

Fig. 2(a)-(d) Cross-section images of multilayer Ga_2O_3 ordered poro
15, and 20 μl of polystyrene (PS) spheres aqueous solution as te
Cross-section images of multilayer Ga_2O_3 ordered porous films prep
M $Ga(NO_3)_{3(aq)}$ solutions, respectively.

ous films prepared with 5, 10,
emplates, respectively; (e)-(g)
ared with 0.02, 0.06, and 0.15

M-P-5: THE MICRO-FABRICATED ELECTROSTATIC ZERNIKE PHASE PLATE FOR PHASE CONTRAST IMAGING IN TEM

WANG, Wan Jhih(王婉雅)[1]; CHUANG, Y. J.[1]; HUANG, S. H.[1]; HSU, C. H.[1]; TSENG, F. G.[1,2]; KAI, J. J.[1] and CHEN, F. R.[1]

[1]Department of Engineering and System Science, National Tsing Hua University, Taiwan,

[2]Division of Mechanics, Research Center for Applied Sciences, Academia Sinica, Taiwan,

Since its high spatial resolution, the transmission electron microscope (TEM) has revolutionized the fields of solid state, materials and biological sciences. However, a more stringent limitation of some specimens, so called weak-phase objects are difficult to image because they interact only weakly with the incident electron beam. For example, thin unstained biological specimens, consisting mainly of light elements (C, O, N, H), thin amorphous films etc. [1] Hence, the phase contrast mechanism plays an important role in the observation of weak-phase objects of high resolution TEM (HRTEM).

Usually, the phase contrast in TEM is realized by defocusing of the objective lens. As a result, the resolution of image decreases dramatically. The carbon film Zernike phase plate, consisting of a thin carbon film with small hole positioned in the center of the back focal plane of objective lens, has been proposed [2]. However, the incoherent scattering caused by the carbon film limits the use of it in HRTEM. In this paper, we successfully fabricate the Electrostatic Zernike Phase Plate (EZPP) by MEMS technology and demonstrate its functionality in TEM.

The EZPP device is a 5-layered ring structure with two suspension beams as shown in Fig. 1. It consists of three Au electrodes and two PECVD Si_3N_4 dielectric insulators. Gold is chosen as the electrode material for its stability to bear the high energy electron beam bombardment in TEM and fast discharge. The image of the micro fabricated EZPP device is shown in Fig. 2. The top and bottom electrodes are connected outside the ring to confine the electrostatic field in the central hole as electric potential applying on middle and top/bottom electrodes.

The operation mechanism of EZPP is shown in fig.3. After coherent electron beam passing through the specimen, the direct beam proceeds parallel to incident beam, while the scattered beam has an angle to the incident direction. The EZPP device is placed in the back focal plane of objective lens in TEM and constructs an electrostatic field in central hole by applying an electric potential to middle electrode and grounding the top and bottom electrodes. The electrostatic field shifts the phase of direct beam to increase its intensity in image. Therefore, the intensity difference between direct and scattered beam gets larger, the contrast of image can be increased effectively [4].

To validate the functionality of the EZPP device, two samples, Nodavirus and NMOS, were used for imaging. Fig. 4 shows the TEM image of Nodavirus with EZPP "off" and "on" with 1.5 volts. By analyzing, the image contrast with EZPP on is increased 4.1% higher than off. The capsid of virus becomes clear. The improvement of image quality enables the observation of detailed structure in biological specimens more clearly. Fig. 5 shows the TEM image of gate structures in NMOS with EZPP off and on. As EZPP is off, the composition of gate oxide, $SiON_x$ and SiO_2, can not be distinguished clearly due to similar atomic composition. But with EZPP on, the contrast between $SiON_x$ and SiO_2 layers increases and the boundary of two layers can be clearly defined. The EZPP device not only increases the contrast of TEM images without loss of image reality but also improves the analysis of specimens composed of light and similar elements. The realization of EZPP paves the way towards phase contrast imaging in TEM.

Corresponding author: Wan Jhih Wang, Department of Engineering and System Science, National Tsing Hua university, 101, Sec. 2 Kuangfu Rd., Hsinchu 30013, Taiwan, Tel: +886-3-5715131 ext. 34282, E-mail: g943107@oz.nthu.edu.tw.

REFERENCES:

[1] O. Scherez, "The theoretical resolution limit of the electron microscope", J. Appl. Phys., vol. 20, pp. 20-29, 1949.

[2] F. Zernike, "Phase-contrast, a new method for microscopic observation of transparent objects.", Physica, vol. 9, pp. 686-698, 1942.

[3] H. Boersch, "Über die Kontraste von Atomen im Elektronenmikroskop", Z. Naturforsch. A, vol. 2A, pp. 615-633, 1947.

[4] P. R. Buseck, J. M. Cowley, and L. Eyring. *High-Resolution Transmission Electron Microscopy and Associated Techniques*. Oxford University, New York, 1992.

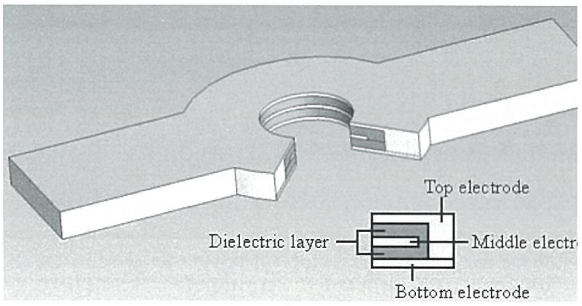

Figure 1. EZPP is a 5-layer-ring structure. The layers from bottom up are bottom electrode-dielectric-middle electrode– dielectric - top electrode.

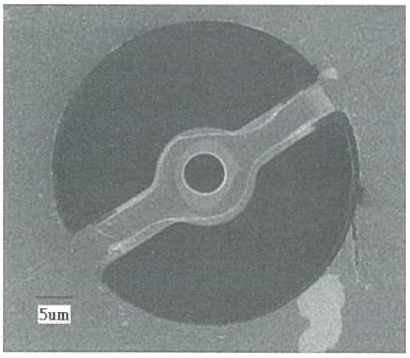

Figure 2.The image of EZPP after opening the central hole by FIB. It ensures the circularity of the hole and the symmetry of electrostatic field.

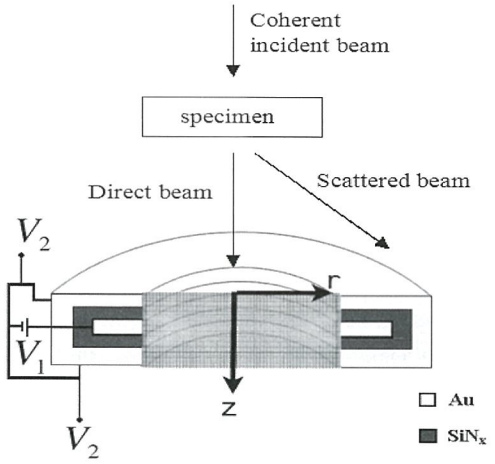

Figure 3. After passing the specimen, the direct beam process parallel to incident beam, while the scattered beam has an angle to the incident direction. EZPP construct an electrostatic field that shifts the phase of direct beam, while the scattered beam isn't influenced.
V_1:applying voltage, V_2:ground.

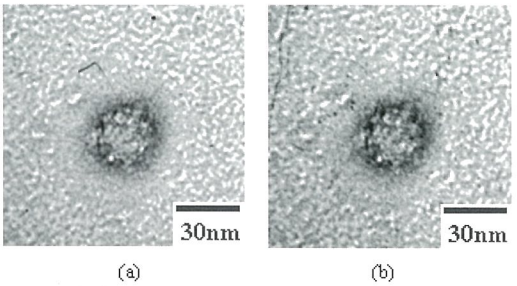

Figure 4. TEM images of Nodavirus *with EZPP (a)"off" and (b)"on", applied voltage 1.5V. The shell of virus composed of light elements becomes clear, which allows the detail structure of virus observed. The contrast of image with EZPP on increases 4.1% than off.*

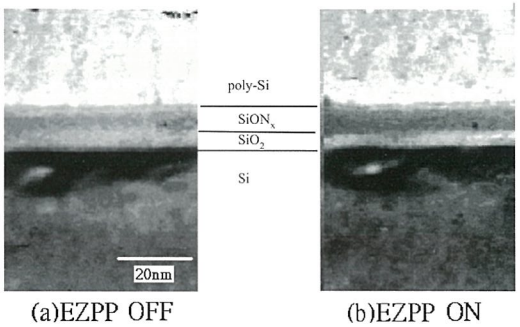

Figure 5. TEM images of NMOS structure with EZPP(a)"off" and (b)"on" ,applied voltage 2V. $SiON_x$ and SiO_2 layers are of similar atomic compositions, the contrast of image is poor with EZPP off. With EZPP on the boundary of layers can be exactly defined, and the thickness of layers can be measured precisely.

M-P-6: THE STUDY OF NANO-CRYSTALLOGRAPH BY COHERENT ELECTRON DIFFRACTION IMAGING

FENG, Chi-Kai(馮祺凱)[1], Dronyak Roman[1,2], CHEN, Fu-Rong[1,2], KAI, Ji-Jung[1]

[1]Department of Engineering and System Science, National Tsing Hua University, Hsinchu

[2] National Synchrotron Radiation Research Center, Hsinchu

The coherent diffractive imaging (CDI) technique offers a promising path toward characterization of the individual non-periodic and near-periodic isolated nanostructures at the atomic resolution[1]. In this aberration-free microscopy, the complex exit surface wavefunction can be recovered from the over-sampled far-field diffraction pattern using iterative algorithms. We have recorded the image (Fig.1) and diffraction pattern (Fig2) of the individual MgO nano-particle with a size of about 24nm with a crystallographic orientation [001] along the incident electron beam. The FEG-TEM (JEOL 2010F) was operated at 200keV accelerating voltage in the nano-area electron diffraction regime. For the reconstruction we utilized the phase-retrieval algorithm[2] with dynamically defined support[3]. Fig 3 shows the shape image of the MgO nano-particle reconstructed from one Bragg peak(200). Figure 4 shows the phase and modulus of the reconstructed wave function. This result is in agreement with the high-resolution image of the particle.

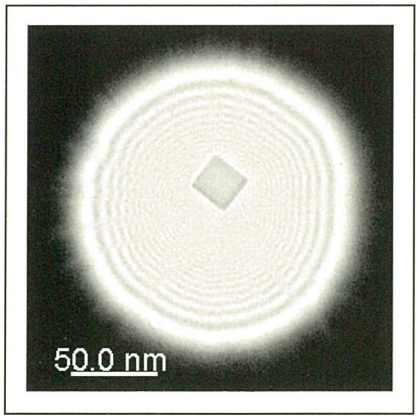

Fig.1 The image of the isolated Magnesium Oxide nano-particle, obtained using a parallel electron probe.

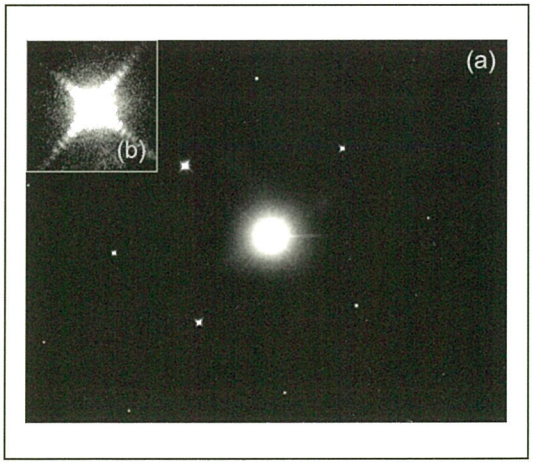

Fig.2(a) Recorded diffraction pattern from MgO nanoparticle near the zone axis of [001]. (b) Enlarged image of the Bragg peak (200) .

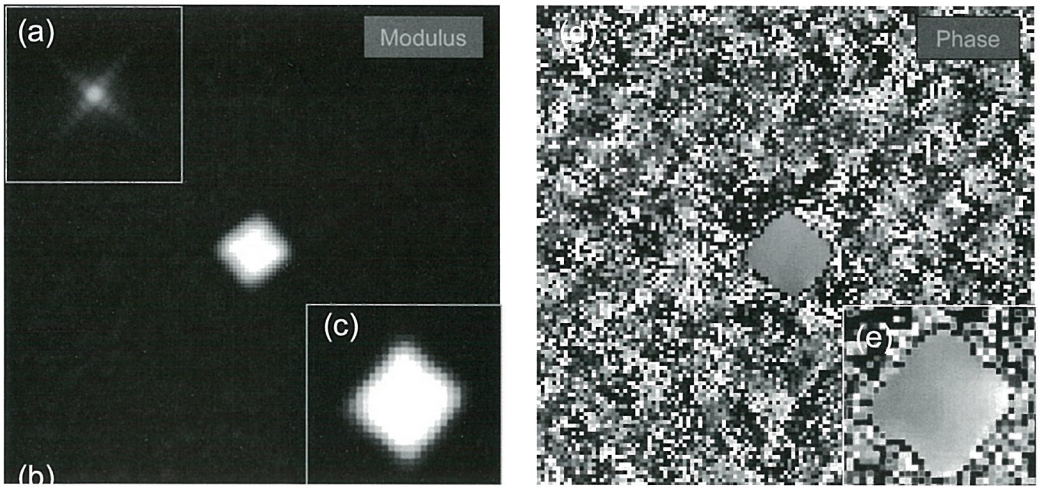

Fig3 (a) Bragg Peak (200) of the MgO diffraction pattern (b~c) Modulus and (d~e) phase of MgO shape reconstruction image from one Bragg peak (200).

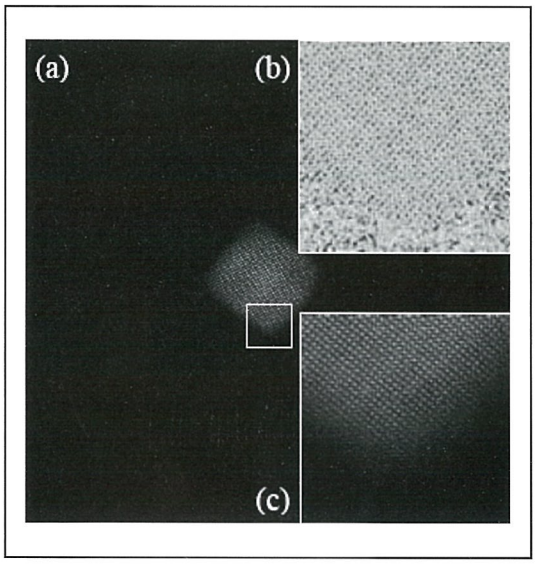

Fig.4 Reconstructed modulus of the exit wavefunction. (b) Enlarged image of the phase and (c) modulus of the wavefunction from the selected region.

Reference :

[1] J. M. Zuo, I. A. Vartanyants, M. Gao, R. Zhang, and L. A. Nagahara, Science 300, 1419 (2003)

[2] Elser V. (2003). J. Opt. Soc. Am. A 20, 40

[3] G.Oszlányi, and A. Sütő, Acta Cryst. A **60**, 134 (2004)

M-P-7: VALENCE STATE MAP OF IRON OXIDE THIN FILM OBTAINED FROM ELECTRON SPECTROSCOPY IMAGING SERIES

CHEN, Ko-Feng[1*], KAI, Ji-Jung[1] and CHEN, Fu-Rong[1,2]

[1]Center for Electron Microscopy, Department of Engineering and System Science, National Tsing-Hua University, HsinChu 30013, Taiwan.

[2]National Synchrotron Radiation Research Center, HsinChu, 30076, Taiwan.

[*]*Correspondence: d913135@oz.nthu.edu.tw*

A set of signal processing methods for electron spectroscopic images (ESI) series has been successfully developed for the mapping of sp^2/sp^3 ratio [1] , dielectric function[2] and energy bandgap[3]. In this study, it was applied to the valence state map of an iron oxide thin film (Fe/α-Fe_2O_3). Two problems, under-sampling and a convolution effect, associated with extraction of the image-spectrum from the core loss image series were overcome by using cubic polynomial interpolation and a maximum entropy deconvolution method (MEM). The reconstructed image-spectrum obtained from the ESI series images has a quality as good as that of conventional electron energy-loss spectroscopy spectra (Fig. 1). The L_3/L_2 ratio of the reconstructed ESI spectrum is determined to be 3.30±0.30 and 5.0±0.30 for Fe and α-Fe_2O_3 respectively. The L_3/L_2 ratio mapping shows an accurate correspondence across the Cu/Fe/α-Fe_2O_3 area (Fig. 2). The effect of de-localization and chromatic aberration on the resolution of ESI is discussed and is estimated to be about 2 nm for the case of L_3/L_2 ratio mapping. This paper demonstrates the applicability of ESI for valence state mapping of the iron-oxide system.

Reference

[1] S. C. Lo, J. J. Kai, F. R. Chen, J. Electron Microsc., 50(6), p497 (2001).

[2] J. Y. Yan, J. J. Kai, F. R. Chen, J. Electron Microsc., 51(6), p391 (2002).

[3] J. S. Tsai, J. J. Kai, L. Chang, F. R. Chen, J. Electron Microsc., 53(4), p371(2004).

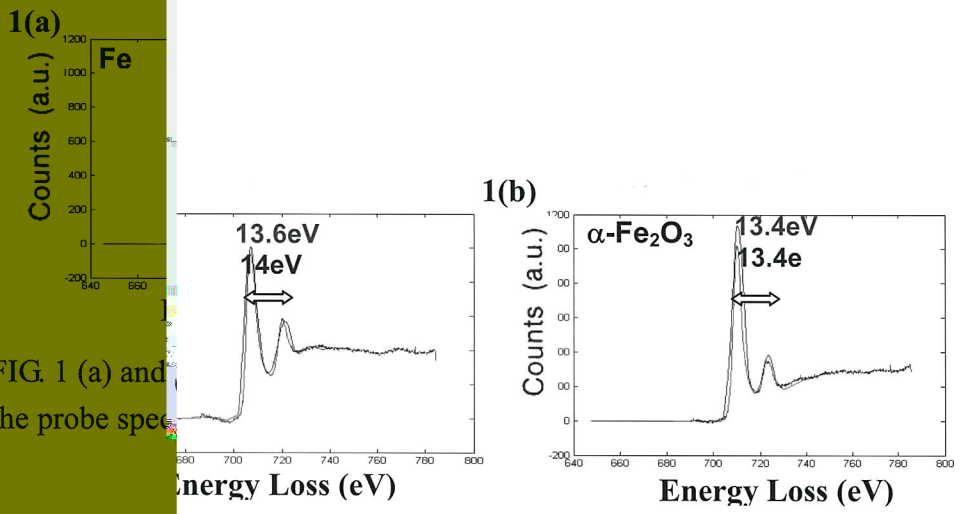

FIG. 1 (a) and
the probe spe
(b) are spectra of Fe and α-Fe_2O_3 respectively. The blue line is
trum and the red line is the ESI signal-processed spectrum.

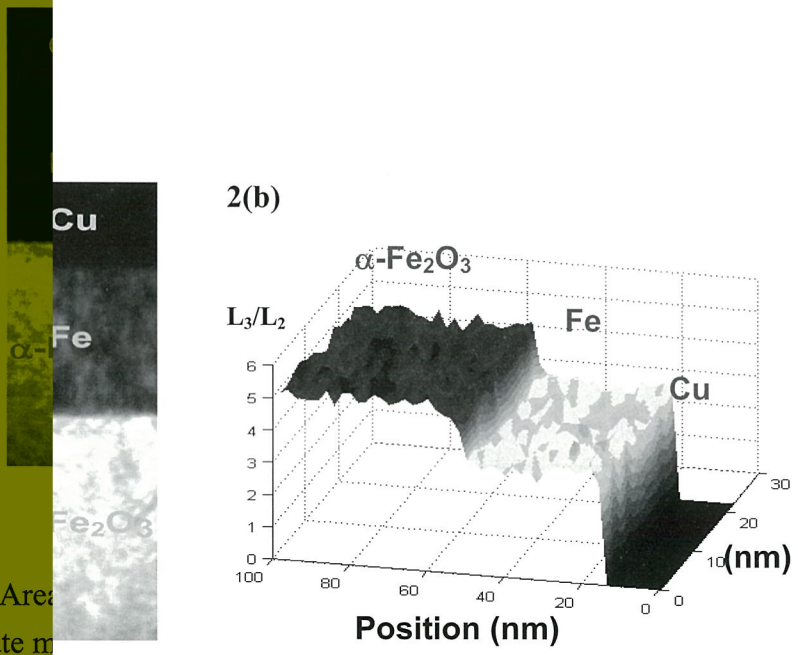

FIG. 2(a) Area
valence state m
a selected for the valence state mapping. In (b) we show the
ap corresponding to (a).

M-P-8: ANNEALING EFFECT ON ELECTROCHROMIC PROPERTIES OF TUNGSTEN OXIDE NANOWIRES

LIAO, Chia-Ching(廖家慶), CHEN, Fu-Rong and KAI, Ji-Jung

Center for Electron Microscopy, Department of Engineering and System Science, National Tsing-Hua University, Hsinchu

The transition metal oxides have drawn much attention from scientists in recent years when they are applied as electrochromic materials. Their potential applications include several technological areas, such as smart windows, self-dimming rear mirror, electrochromic display, sensor etc [1-3]. Among a variety of the transition metal oxides, tungsten oxide is found to be the most efficient candidate for electrochromic applications. The electrochromic performance of tungsten oxide, reversible coloration under double injection of ions and electrons, strongly depends on its nature and microstructure.

The chromatic properties of WO_{3-x} films strongly depend on stoichiometry of the tungsten oxide films (i.e., oxygen vacancies) that are very sensitive to the conditions of deposition and specifically to atmosphere used and the temperature. In vacuum deposition methods, as-deposited film is blue due to the oxygen deficiencies. Generally, WO_{3-x} films have a metallic aspect for $x > 0.5$. The appearance of the films is blue for x in the 0.3-0.5 range and it becomes transparent if x is below 0.3. However, after annealing, the appearance will change to a higher optical transmittance due to the fact that more W^{6+} will be created in the films.

In this study, we discuss the annealing effect on the optical and electrochemical properties of thermally evaporated tungsten oxide nanowire films on transparent conducting substrates. The transmittance of the annealed WO_{3-x} nanowire films could be increased by creating more W^{6+} in the virgin nanowire films. The morphology and structure of the nanowire films still maintained the same if the annealing temperature was up to 500 °C. The optical and electrochemical properties of the WO_{3-x} nanowire films can be greatly enhanced by heat treatment, but the coloration/bleaching time only slightly increased because of a small augmentation of resistance of the transparent conducting thin films and WO_{3-x} nanowires.

Reference:

[1] R. D. Rauh, Electrochimica Acta 44 (1999) 3165-3176

[2] K. Bange and T. Gambke, Adv. Mater. 2 (1990) 10-16

[3] K. Yamanaka, J. J. Appl. Phys. 26 (1987) 1884-1890

Figure 1. SEM images of the WO_{3-x} nanowire films: (a) as-deposited; (b) annealed at 500 °C 1h; (c) annealed at 600 °C 1h.

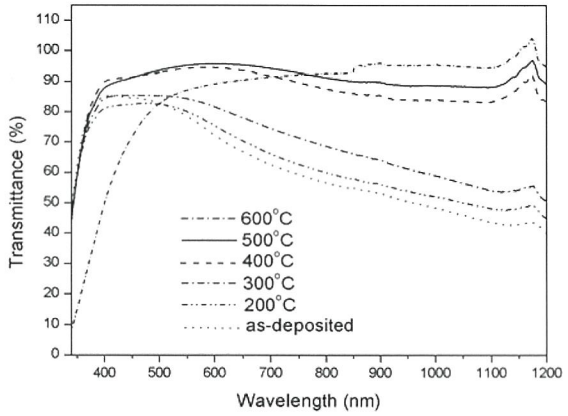

Figure 2. Transmittance spectra of the virgin WO_{3-x} nanowire films: as-deposited and annealed at 200, 300, 400, 500 and 600 °C between wavelength of 340 and 1200 nm.

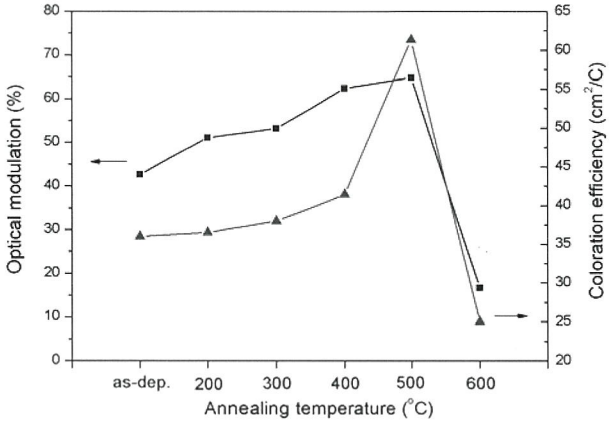

Figure 3. Relative optical modulation and coloration efficiency at 700 nm wavelength of the as-deposited WO_{3-x} nanowire film and the annealed WO_{3-x} nanowire films.

M-P-9: TEM STUDY OF NANOCRYSTALLINE ZrN_xO_y THIN FILM

LIU, Yee-Lang[a], HUANG, Ja-Hong[a], CHEN, Fu-Rong[a] ,and KAI, Ji-Jung[a]

[a]Center for Electron Microscopy, Department of Engineering and System Science, National Tsing-Hua University, Hsinchu, Taiwan. 30043, R.O.C.

Varying oxygen flow rate ranging nanocrystalline ZrN_xO_y thin films were deposed on p-type (100) Si substrates using hollow cathode discharge ion-plating system[1]. The oxygen content of the thin film was determined using X-ray photoelectron spectroscopy (XPS), increased with increasing oxygen flow rate. As the oxygen content increased, the color of the ZrN_xO_y thin film changed from golden yellow to blue anf then slate blue, and the microstructure observed scanning electron microscopy (SEM) varied from columnar structure to finer grains and finally flat and featureless structure. Phase separation of ZrN_xO_y to ZrN and monoclinic ZrO_2 was found from X-ray diffraction (XRD) patterns when the oxygen content was higher than 9.7 at. %. The element content variation with oxygen rate is shown as Fig. 1.

This study using a serial TEM dark field images to locate the position of ZrN and ZrO_2 nanocrystals in the ZrN_xO_y thin film. Fig. 2 is the diffraction pattern of ZrN_xO_y thin film as condition 2 in Fig. 1, contains 30 at.% ZrO_2 in structure. We take a serial dark field image from ZrO_2 (111) and ZrN (111) plane to collect the distribution in the specimen. And then we use DigitalMicrograph (DM) to combine the images into one to figure out the distribution of ZrN and ZrO_2 in the ZrN_xO_y thin film, shown as Fig. 3 (a) and (b).

In Fig. 3(a), we can see the ZrN has an average size of 20~35 nm and the ZrO_2 has an average size as 3~8 nm in 3 (b). We can combine these two pictures into one, shown as Fig. 3(c). In this figure, ZrO_2 nano grain surrounding around ZrN grain, compare with the result of XPS as Fig. 1. The oxygen content in this condition is not enough to produce ZrO_2 to surrounding each grain from the grain boundary of ZrN nanocrystal, and then several grains combine into a cluster to release excess oxygen and produce ZrO_2 particle at the boundary of the cluster.

Reference

[1] J-H. Huang *et al.*, Surface & Coating Technology 201 (2007) 6404-6413

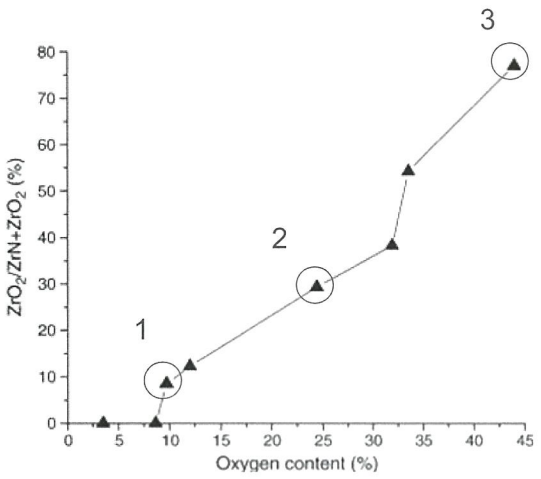

Fig.1 The variation of element contents with O_2 flow rate.

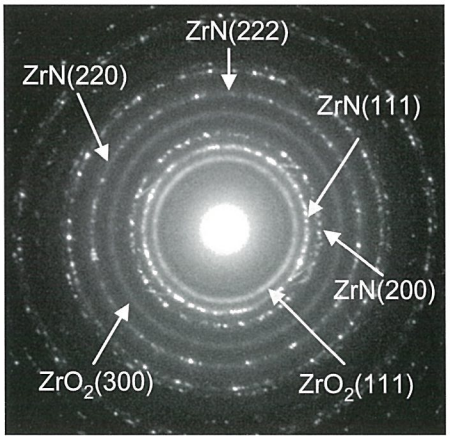

Fig. 2 Diffection pattern of ZrN_xO_y thin film

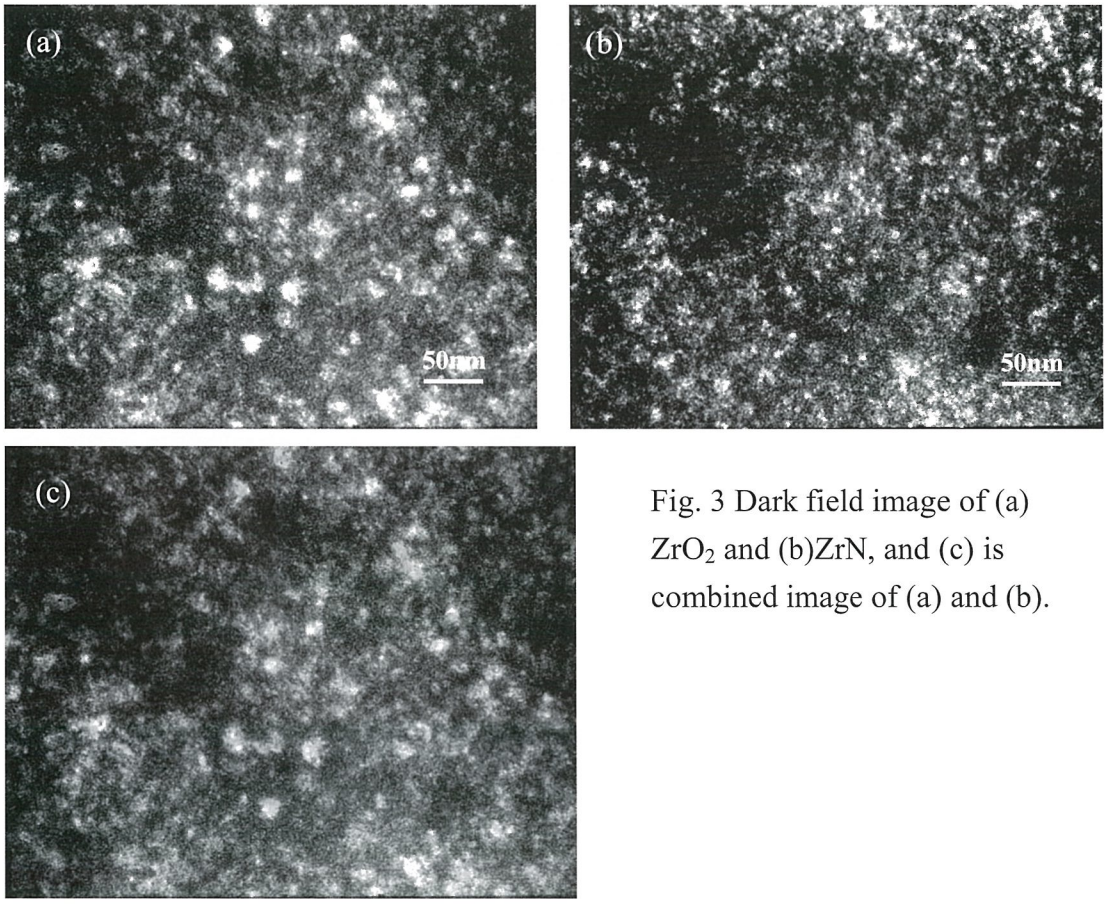

Fig. 3 Dark field image of (a) ZrO_2 and (b)ZrN, and (c) is combined image of (a) and (b).

M-P-10: Observation of V-defects in multiple InGaN/GaN quantum wells

TSAI, H. L.[a]*, WANG, T. Y.[a], YANG, J. R.[a] KUO, T. W.[b], FENG, Z. C.[b] and LI, Alan G.[c]

[a] Department of Materials Science & Engineering, National Taiwan University, Taipei, Taiwan. 106, R.O.C.
[b] Graduate Institute of Electro-Optical Engineering and Department of Electrical Engineering, National Taiwan University, Taipei, Taiwan. 106, R.O.C.
[c]ShenZhen Fangda GuoKe Optronics Technical Co. Ltd., FangDa Town, Longjing, Xili, Nanshan, ShenZhen, China 518055.

Recent developments in wide band-gap Ⅲ-V nitride compound semiconductors have led to the commercial production of blue/green light-emitting diodes (LEDs), but there are still many problems caused by use of the sapphire substrate. The large lattice mismatch and thermal expansion coefficient difference between GaN and sapphire lead to the defect material, with huge densities of several defects such as threading dislocations (TDs), stacking faults (SF), and V-defect. The main structure of LED used in this study consists of a 50 nm-thick InGaN electron emitter layer, a 1 nm-thick GaN tunneling barrier layer, and a 8-period InGaN(2.5 nm)/GaN(7.5 nm) active region, which is called the asymmetric resonance tunneling(CART) structure. The structure can indeed significantly increase the LED output intensity. HAADF-STEM provided undoubted evidence that V defects in the multiple QW have the thin six-walled structure with InGaN/GaN $\{10\bar{1}1\}$ layers. The detailed structure of the observed V defects is discussed on the basis of the formation mechanism of V defects which was proposed taking into account the growth kinetics of the GaN crystal and a masking effect of In atoms segregated around the threading dislocation. We can deposit strain layer superlattice to decrease the density of threading dislocations to reach to the surface, and then decrease the density of the V-defects. By increasing the deposition temperature of active region can also suppress the formation of V-defects.

Reference

[1]M. Shiojiri, C. C. Chuo, J. T. Hsu, J. R. Yang and H. Saijo, J. Appl. Phys. **99**(2006)073505.
[2]C. H. Chen, Y. K. Su, S. J. Chang, G. C. Chi, J. K. Sheu, J. F. Chen, C. H. Liu and Y. H. Liaw, IEEE electron device lett. 23(2002)130.

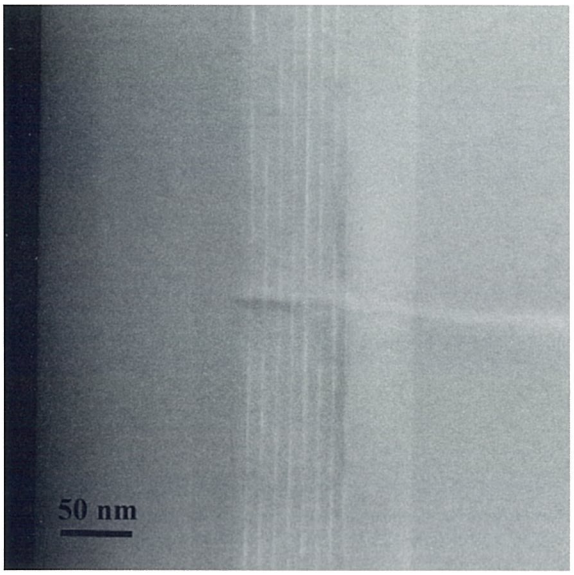

Fig.1 The main structure of the active region in the LED observed by HAADF-STEM.

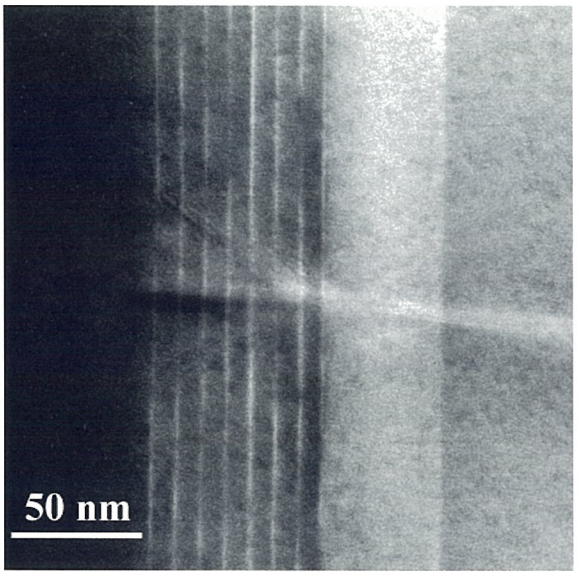

Fig.2 HAADF-STEM image of V defects in InGaN/InGaN MQWs

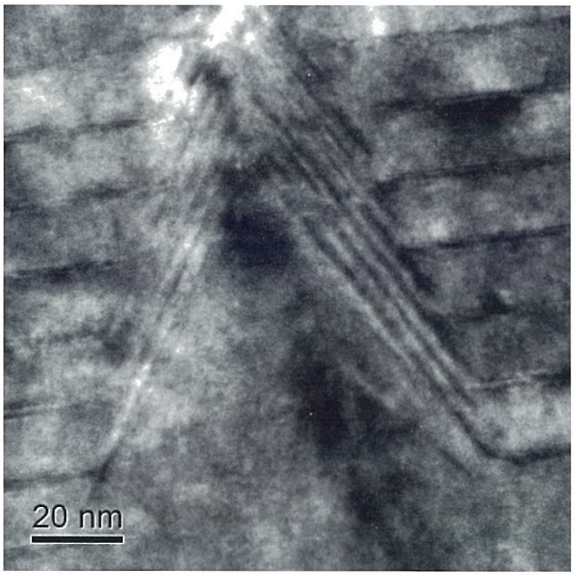

Fig.3 CTEM image of V defects in InGaN/InGaN MQWs

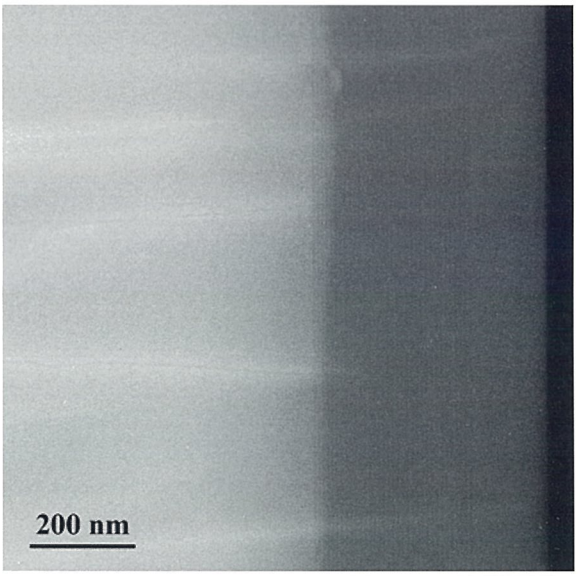

Fig.4 HAADF-STEM image of 34 period AlGaN/GaN SLSs.

Property of Nano-Composite Prussian Based Thin Film

CHEN, Fu-Rong and KAI, Ji-Jung
nt of Engineering and System Science, National Tsing-Hua

e and more important because it possesses low power ial to be applied to e-paper. However, slow response is technology, and other performances, like contrast, . Our present work is to synchronously improve the Prussian Blue (PB) by applying the concept of used in electrochromic devices (ECDs) as a sole ode, especially in complementary tungsten oxide uses H^+ or Li^+ based electrolyte, whose ion radius and WO_3 film may fail rapidly owing to dissolution in H^+ trolytes are expected to have better electrochromic use the radius of hydrated K^+ is smaller than that of why K^+ based electrolytes were utilized by almost WO_3 with PB, a polymer electrolyte prepared from PO_4 and KH_2PO_4 was introduced into WO_3-PB ECD electrolyte contains both H^+ and K^+ ions; the former with WO_3 and PB respectively. Li^+ based WO_3-PB , 4], however improvements on electrochromic ctrolyte system was not yet reported. We present an Blue (NPB) film to synchronously improve the Prussian Blue (PB) film by applying the concept of indium tin oxide (ITO) nano-particles (3.0+/-1.0Ω, o gain larger operative reaction surface area in Li^+ n.

(1991) 203-207
. Chem. Soc., 104 (1982) 4767-4772
d H. Nishii, U.S. Patent No. 4,773,741 (1988)
Kase, Y. Maeda, U.S. Patent No 4,645,307 (1987)

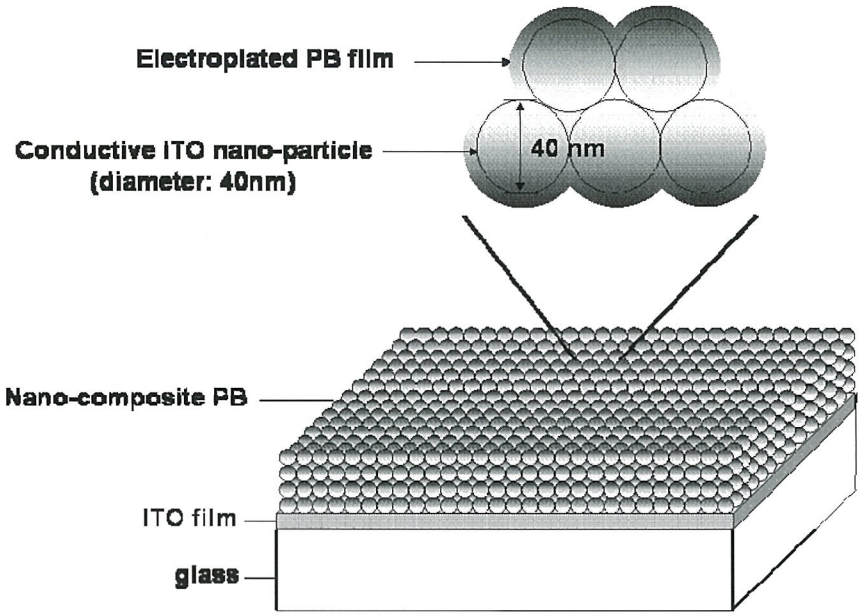

Figure 1. Conceptual structure of nano-composite PB (NPB) film. The NPB film consists of random arrangement of ITO nano-particles covered with electrodeposited PB. Each ITO nano-particle contacts with its neighboring particles, thus electrons have sufficient pathways to move through the porous film.

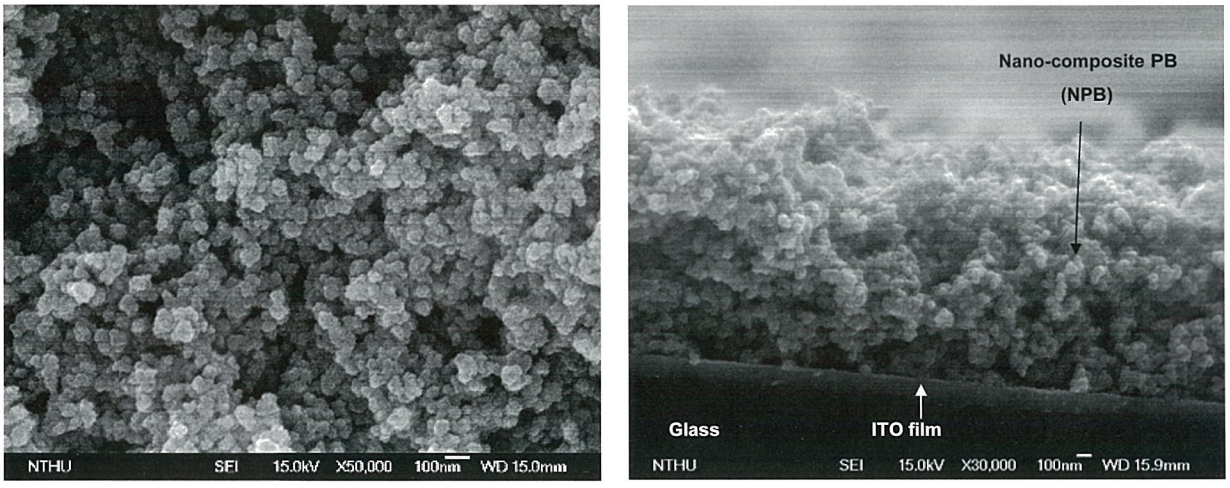

(a) (b)

Figure 2. SEM images of PB film electroplated onto pre-coated ITO nano-particle layer (sample 2). (a) top view at 50,000X, (b) cross-sectional view at 30,000X.

M-P-12: STEM-EELS INVESTIGATION OF AU NANOPEAPODS EMBEDDED IN SILICA

WU, Chien-Ting (吳建霆)[a], CHEN, Chun-Wei[a], CHEN, Kuei-Hsien[b], CHEN, Li-Chyong[c], CHU, Ming-Wen[c], CHEN, Cheng-Hsuan[c]

[a]Dept. of Material Science and Engineering, National Taiwan University, Taiwan
[b]Institute of Atomic and Molecular Sciences, Academia Sinica, Taipei, Taiwan
[c]Center for Condensed Matter Sciences, National Taiwan University, Taiwan

Noble-metal nanoparticles embedded in dielectric matrices show nonlinear and fast optical response near the surface-plasmon-resonance (SPR) frequency due to their enhanced third-order optical susceptibilities and have been applied in optical switching devices [1,2]. In our previous work, we had grown a self-organized photosensitive gold nanoparticle chain encapsulated inside a silica dielectric nanowire. Such a hybrid peapod nanowire shows pronounced SPR absorption and the device exhibits a wavelength-dependent photo-response in electrical resistance [3]. It is of great importance to study the microstructure and electronic structure of the nanocomposite in order to fully understand the optical response of the hybrid nanowire. Here we report STEM-EELS studies of the hybrid nanowire.

Our EELS studies show that the gold nanoparticles embedded in the nanowire are actually phase-separated into pure gold and silicon. The position-dependent EELS spectra of the hybrid nanowire are shown in Figure 1. Figure 1(a) is a typical STEM image exhibiting the Z contrast. The intensity line profile across a Au nanoparticle (red line in 1(a)) is shown in figure 1-(b) and the corresponding position-dependent EELS spectra are displayed in figure 1-(c) and (d). From the characteristic the EELS spectra of bulk plasmon and interband transitions, we conclude that the peapods embedded in SiO_x are phase-separated into Au and Si under the present growth condition. The surface plasmon of Au at 2.4eV is also observed and it presence could be detected at a distance more than 10nm outside the Au surface edge in the SiO_x matrices. The investigation of the coupling of the surface plasmon of Au as a function of the NP distance is currently in progress.

References

[1] F. Hache, D. Ricard and C. Flytzanis, J. Opt. Soc. Am. B **3,** 1647–1655 (1986).
[2] R. F. Haglund, et al., Opt. Lett. **18,** 373–375 (1993).
[3] M. S. Hu, L. C. Chen, et al., Nature Materials, 5, 102, (2006)

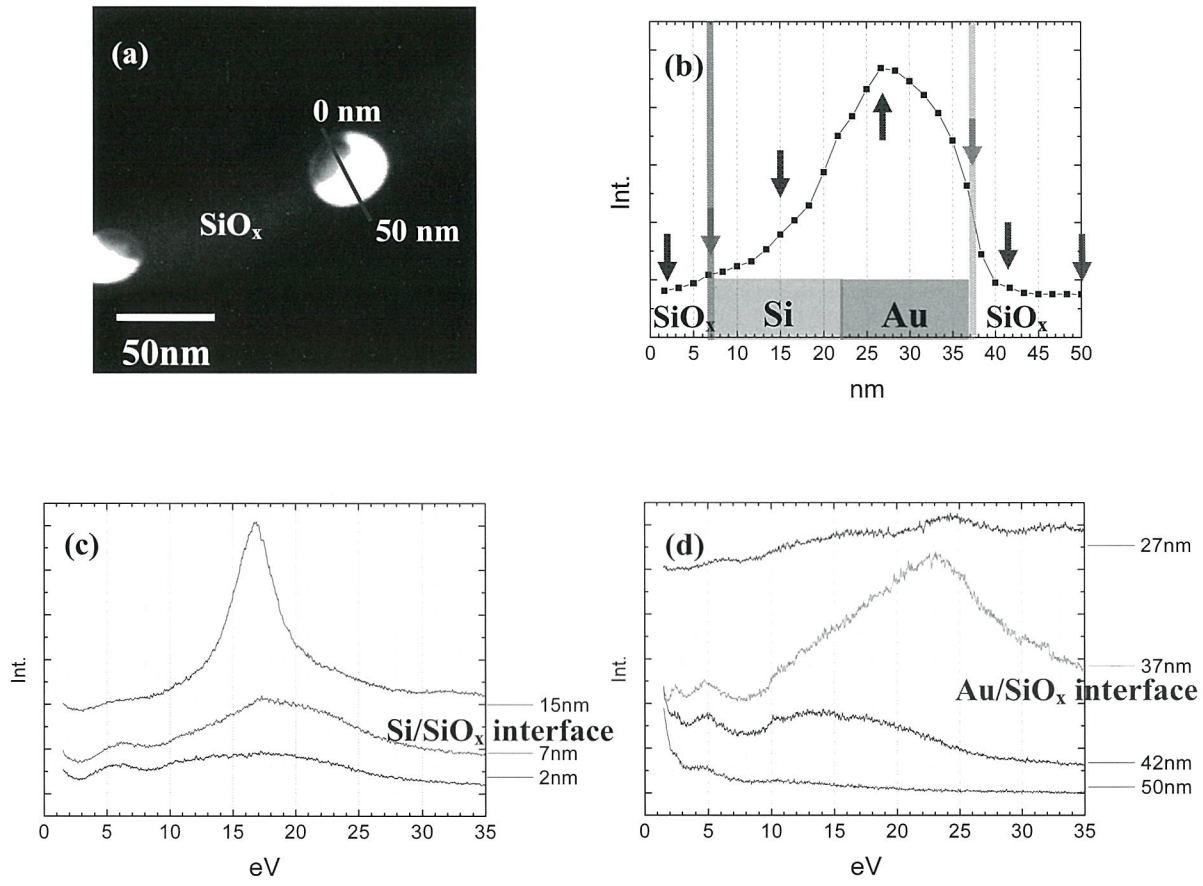

Fig 1 The STEM image and EELS spectra with position relative line profile of the hybrid nanowire.

M-P-13: ELECTRONIC MICROSCOPY STUDY OF EPITAXIAL GROWTH OF GALLIUM NITRIDE ON PATTERNED SAPPHIRE SUBSTRATES

CHEN, Hou-Guang (陳厚光)[1] ; CHANG, LI(張立)[2], WU, Yue-Han (吳岳翰)[2]; KO, TS (柯宗憲)[3]; LU, Tien-Chang (盧廷昌)[3]; KUO, Hao-Chung (郭浩宗)[3] and WANG, Shing-Chung (王興宗)

[1)]Department of Materials Science and Engineering, I-Shou University, Kaohsiunng, Taiwan 840

[2)]Department of Materials Science and Engineering, National Chiao Tung University, Hsinchu, Taiwan 300

[3)]Department of Photonics & Institute of Electro-Optical Engineering, National Chiao Tung University, Hsinchu 300, Taiwan

GaN and other related III-nitride base semiconductor are the promising materials for applications in light-emitting devices covering the ultraviolet and full visible range of the electromagnetic spectrum. Due to large lattice mismatch between GaN and sapphire substrates, highly defective GaN films are always formed by conventional MOCVD process. In this paper, we demonstrate that GaN grown on novel patterned r-plane sapphire substrates with asymmetric inclined facets can have a very low defect density in GaN epi-layer without re-growth process.

GaN stripes grown on the striped pattern of sapphire can be observed in Fig. 1 (a). The SEM image shows that each period of GaN stripe consists of two crystallites terminating different faces. The microstructure of the GaN stripe was studied by TEM. Fig.1 (b) shows one complete GaN stripe, with the corresponding selected-area electron diffraction pattern in Fig. 1 (c). The striped mesa is along [11-20] with two etched sides in {0001} and {1-101} faces, as shown in Fig. 1 (d). GaN grown on both etched facets exhibit different crystallographic relationships with sapphire substrate which are $(1\text{-}102)_{sapphire}//(11\text{-}20)_{GaN}$ and $[11\text{-}20]_{sapphire}//[\text{-}1100]_{GaN}$, and $(0001)_{sapphire}//(0001)_{GaN}$ and $[11\text{-}20]_{sapphire}//[\text{-}1100]_{GaN}$, respectively. The region above the sapphire striped mesa contains a very high density of defects, such as threading dislocations (TDs) and stacking faults (SFs) which are usually observed in epitaxial growth of a-plane GaN on r-plane sapphire. However, the defect density in GaN I is reduced with the distance from the mesa in the lateral direction. Examination of the neighboring crystallite GaN II shows that the top surface parallel to the r-palne of sapphire is (11-22) facet with a narrow width, while the rest two inclined facets are (11-20) and (0001) planes. GaN II contains lower densities of defects. The dislocation densities can be significantly reduced through lateral epitaxial growth mechanism from the inclined lateral faces of mesas. The low dislocation density ($\sim 10^7$ cm^{-2}) of non-polar GaN epitaxy can be achieved by metalorganic chemical vapor deposition.

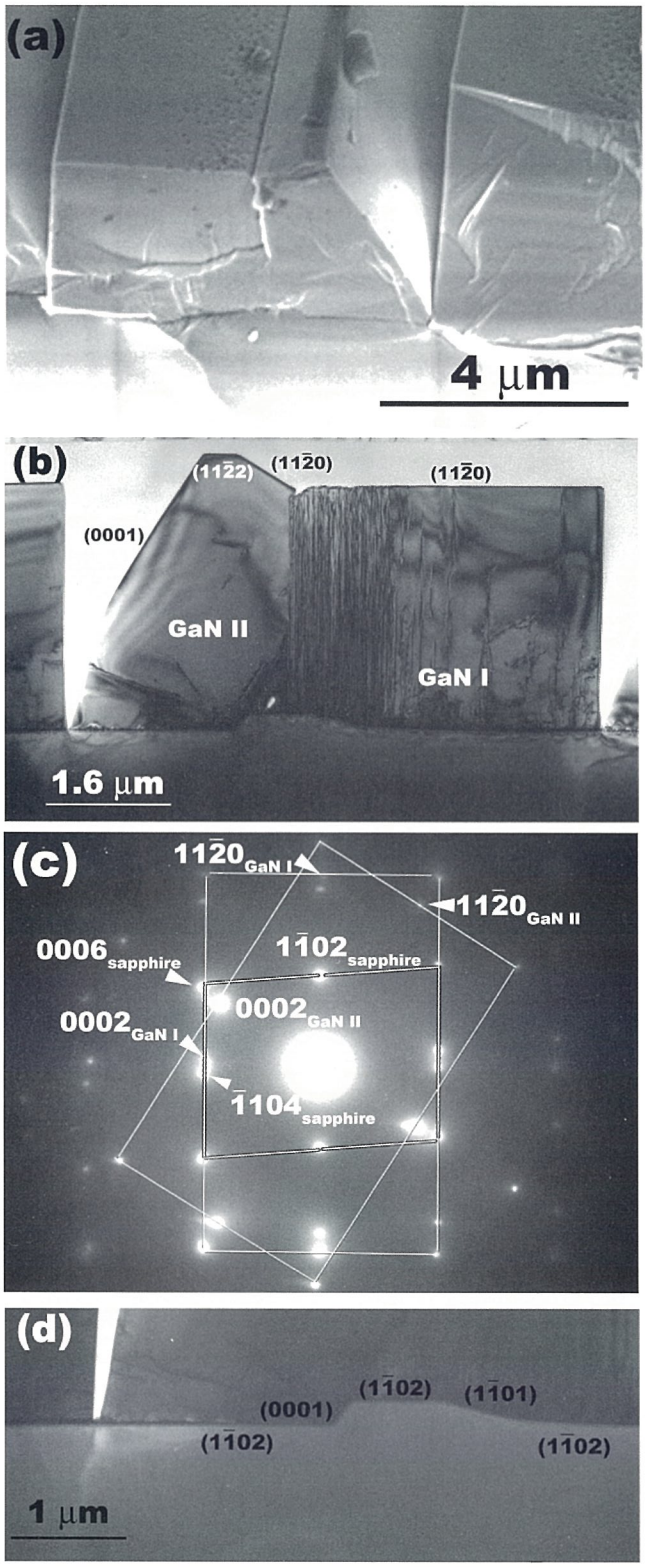

FIG. 1(a) Cross-section SEM image taken in tilted view showing that each GaN stripe consists of two crystallites with facets in different oreintations. (b) Bright-field (BF) TEM image showing one complete GaN stripe. (c) Selected-area electron diffraction pattern corresponding to (b). (d) Enlarged image of sapphire striped mesa.

M-P-14: INVESTIGATION OF THE HIGH-ORDER-LAUE-ZONE LINES' SPLITTING BY KINEMATICAL CBED SIMULATION

KO, Yu-Feng(葛裕逢)[1,2]; LI, CHANG[2]; CHU, HongYuan[1] and LEE, Jon C.[1]

1. Taiwan Semiconductor Manufacturing Company, Ltd, Hsinchu, Taiwan.
2. Department of Materials Science and Engineering, National Chiao Tung University, Hsinchu, Taiwan.

Convergent Beam Electron Diffraction (CBED) as an effective tool of strain measurement with high spatial resolution has been applied to semiconductor materials for a long time. Recently, the splitting HOLZ (High-Order-Laue-Zone) lines in the Si case have been present as a challenge for interpretation though many works have reported the splitting phenomena of the HOLZ lines. Until now, the exact root cause of the HOLZ lines' splitting remains uncovered (1-3). This work addresses a simple methodology to verify the root cause qualitatively. Several important features are identified by visual observation on the acquired CBED patterns. The most important characteristic among these features is that the splitting HOLZ lines can be divided into two groups according to their contrast. One group consists of solid and black HOLZ lines, and the other group includes faint and grey HOLZ lines. The HOLZ lines in each group can be regarded as belonging to one individual CBED pattern, that is, the CBED with splitting HOLZ lines consists of two superposed patterns without splitting HOLZ lines. Reverse process could be inferred from this suggestion. Then two phases of kinematical simulation of the HOLZ lines in the bright-field disc are implemented, and three criteria are introduced to evaluate the results of the CBED simulation in comparison with experimental data. The results of the kinematical simulation of the HOLZ lines show that the uniaxial rotation of the unit cell is the most significant parameter to describe the main features of the splitting HOLZ lines. In other words, The kinematical simulation of the HOLZ lines of the CBED can qualitatively verify that the dominant factor for the splitting HOLZ lines is uniaxial rotation due to sample bending, followed by variation of lattice parameters.

(1). Chuvilin, A. et al. J. Elec. Micr, 54(6): 515-517, 2005.
(2). Armigliatoa, A. et al., J. Appl. Phys., 99(6): 064504, 2006.
(3). Houdellier, F. et al. Ultramicroscopy, 106: 951-959, 2006.

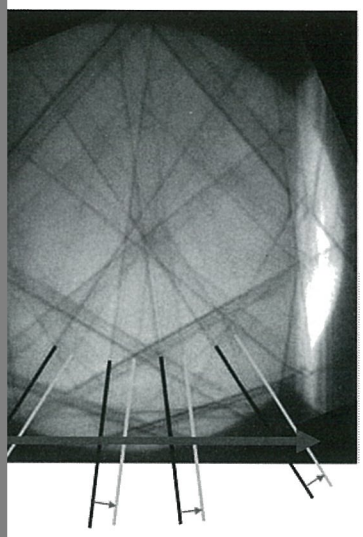

n an unstressed region in Si substrate. (b)
ssed region in Si close to the Si/SiGe

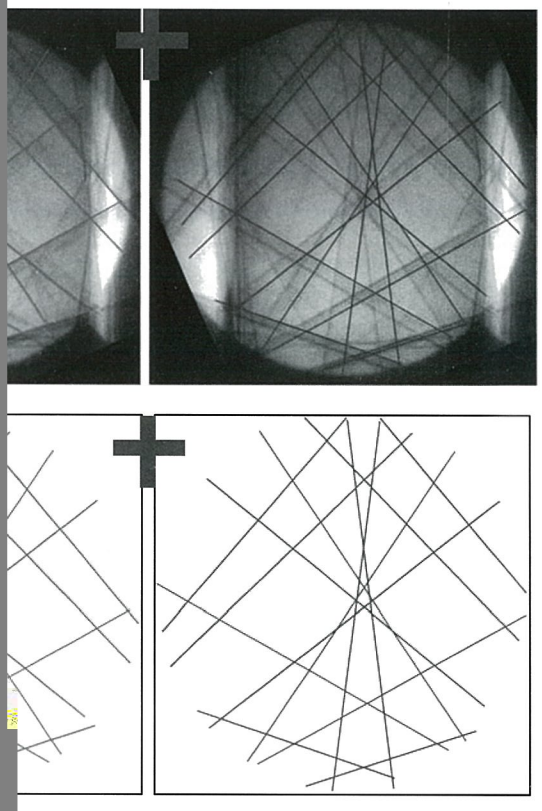

o two groups of lattices 1 and 2. (b) Two
eters of lattices 1 and 2 are combined

M-P-15: The pH Effect to the Phosphate-permanganate Conversion Coating on the AZ31 Magnesium Alloys

CHU, Y. R. (褚喻仁), LI, W. J. and LIN, C. S.(林招松)

Department of Materials Science and Engineering, National Taiwan University, Taipei 106 Taiwan

Abstract

Magnesium alloys have emerged as a highly regarded material in the applications where the weight of the structure is a primary concern. Conversion coating treatment is the most commonly used method to improve the corrosion resistance of magnesium alloys, because of the simplicity in the treatment and the adhesion enhancement for the subsequent painting. Among the numerous systems, the phosphate-permanganate system, so far a promising choice to be the replacement for hexavalent chromate conversion coating, exhibits corrosion resistance comparable to the hexavalent chromate counterpart.

In this study, phosphate-permanganate conversion coating was performed on AZ31 magnesium alloy, with emphasis on the effect of solution pH. It was found (Experimental results indicate) that the solution pH markedly influenced the microstructure and properties of the coating, especially the surface morphology. The color of the coating was, in order, dark brown, golden yellow and light yellow as the solution pH was increased from 4.4 to 6.9. Cracks were commonly seen on the various samples and likely to be induced by dehydration during post-immersion drying process. Increasing solution pH resulted in the coating with smaller cracks and better corrosion resistance. Another striking effect that the solution pH had was the formation of crystal-like precipitates in the solution with pH exceeding 5.7

Cross-sectional TEM further revealed that the coating formed in lower pHs, i.e. around 4, was mainly composed of a porous layer directly contacting the magnesium substrate and cellular overlay. In the solution with higher pHs, the coating was thinner, whereas its microstructure became more complex. With the microstructure gathered in mind, the effect of solution pH on the growth mechanism of the coating was discussed in details.

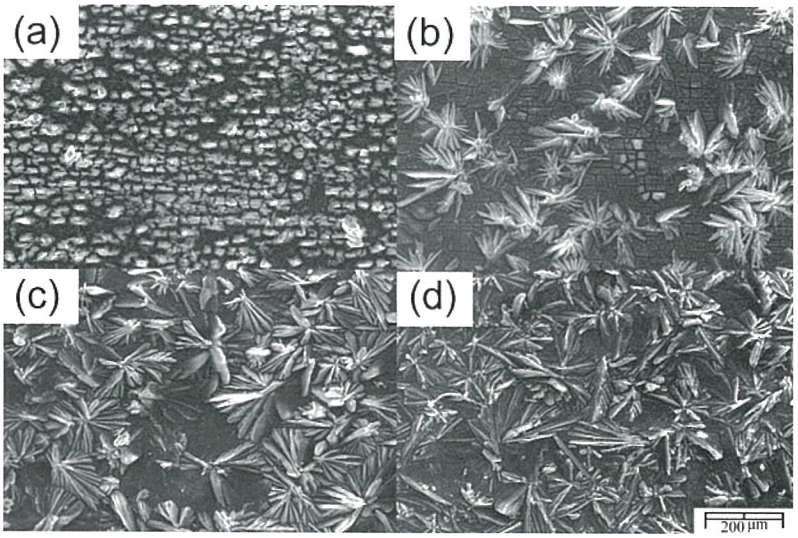

Figure 1 Surface morphology of the coating formed under (a) pH 4.4 (b) pH 5.7 (c) pH 6.3 (d) pH 6.9.

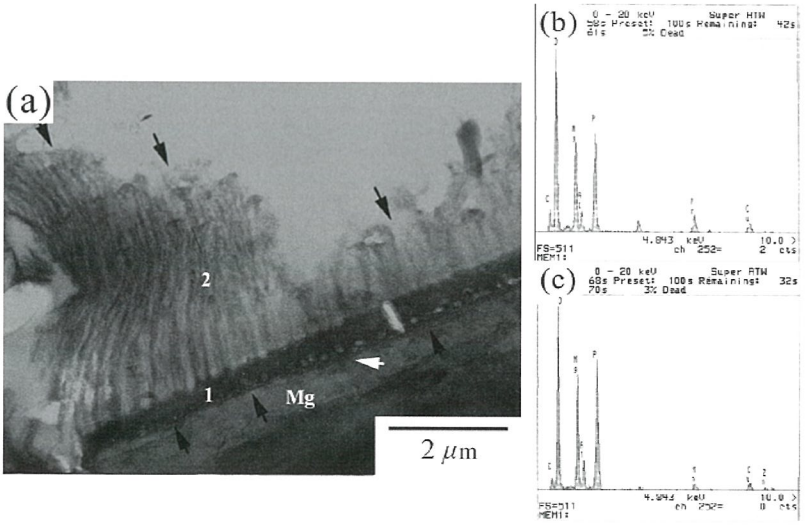

Figure 2 Cross-sectional TEM image and EDS analysis of the coating formed in the lower pH.

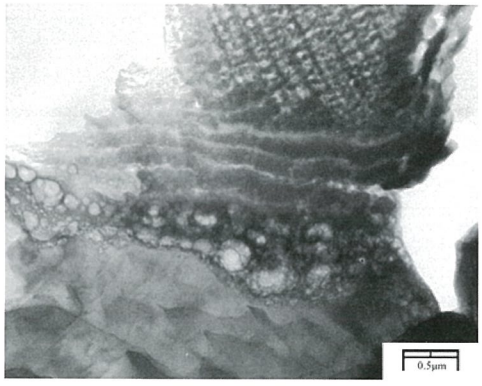

Figure 3 Cross-sectional TEM image of the coating formed in the pH 5.7.

M-P-16: In-situ TEM heating zinc-zinc oxide core-shell nanowires

CHEN, Yen-Chih(陳彥志); TU, Chia-Hao(涂嘉豪) and LIU,Chuan-Pu (劉全璞)

Department of Materials Science and Engineering, National Cheng-Kung University, Tainan, Taiwan 701

In this work, we first used thermal evaporation method to synthesize zinc-zinc oxide (Zn-ZnO) core-shell nanowires. The diameter of the Zn-ZnO nanowire shown in Fig.1 is about 100 nm where the thickness of core and shell is 80 and 20 nm, respectively. The Zn-ZnO core-shell nanowires are single crystal with certain crystallographic relationship from the TEM diffraction pattern in Fig 2. Subsequently, in-situ heating of the nanowire was performed in a JEOL 2010 TEM with a heating holder up to 450 ºC (10℃/min). Figure 3 are a few snapshots of TEM bright-field images recorded at different temperature. The Zn-ZnO core-shell nanowire remained unchanged until 350 ºC. When temperature was raised to 400 ºC in Fig 3 (a), we can observe that a portion of the tip collapsed and Zn core started to evaporate from the nanowire via this tip as indicated by the arrow. When we continued heating this nanowire to 450 ºC in Fig 3 (b), we can find that the nanowire became a ZnO nanotube due to the complete Zn shell evaporation during this period. The entire process involved the Zn phase transformation from solid to liquid and thus the morphology of the front end of the core. When temperature was cooled to room temperature an interesting phenomenon happened as to re-deposition of Zn nanoparticles on the ZnO core surface. The typical size of the nanoparticles is around 15 nm from the TEM image in Fig. 3(c). While some of the nanoparticles show uniform contrast, some of the nanoparticles exhibit strong diffraction contrast as representing by the arrow, indicating that the Zn nanoparticle epitaxially grown on the ZnO shell. How this occurs and related physical properties are still under study. However, this interesting process to grow epitaxial nanoparticles may be applied on other material nanoparticle fabrication and this nanostructure may have potential applications to optoelectronic and nano-scale devices.

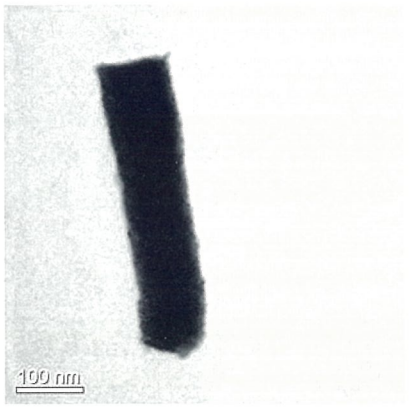

Fig.1: TEM bright-field image of the as-synthesized Zn-ZnO core-shell nanowire.

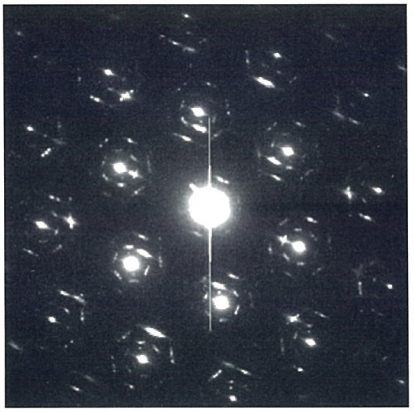

Fig.2: TEM diffraction pattern of the nanowire shown in Fig.1.

Fig.3: TEM bright-field images of the Zn-ZnO core-shell nanowire during in- situ heating and colloing when temperature is (a) at 400 ℃, showing the tip collapse; (b) at 450 ℃, showing only a ZnO tube left behind from Zn evaporation; and (c) cooled back to room temperature, showing the Zn nanoparticle formed on the ZnO core surface.

M-P-17: $Pd_{40}Ni_{40}P_{20}$ 非晶合金在 350-450 °C 空氣下之氧化行為研究

任一飛、謝心心、何日新、陳妍蓉、開物*

The-Oxidation of a $Pd_{40}Ni_{40}P_{20}$ Bulk Amorphous Alloy at 350-450°C in Dry Air.

JEN, I-Fei ; HSIEH, Hsin-Hsin ; Ho, Jih-Hsin ; CHEN, Yen-Jung and KAI, Wu*
Institute of Materials Engineering, National Taiwan Ocean University
*聯絡作者：wkai@mail.ntou.edu.tw 基隆市中正區北寧路二號

摘要

本研究探討鈀基 $Pd_{40}Ni_{40}P_{20}$ 非晶合金在 350-450°C 空氣下的氧化行為。研究結果顯示，鈀基非晶合金之氧化動力學在 350-450°C 中遵守拋物線型定律，且氧化速率隨溫度上升而加快；由穿透電鏡分析得知，鈀基非晶合金氧化後主要生成單一的氧化鎳(NiO)層，並在氧化層下方有鈀磷的富集層生成，顯示氧化物的生成主要是由鎳離子外擴散所致。此外，由 XRD 分析得知，非晶合金在 390°C 氧化 10 分鐘後基材即有 Pd_3P、Ni_3P 及 Ni_2Pd_2P 三種結晶相生成，顯示非晶合金基材於氧化初期已有結晶相變化的發生。

關鍵字：鈀基非晶合晶；拋物線型定律；富集層；氧化鎳。

Abstract

The oxidation behavior of a $Pd_{40}Ni_{40}P_{20}$ (in at.%) bulk-metallic glass (BMG) was studied over the temperature range of 350-450°C in dry air. The oxidation kinetics of the BMG alloy generally followed the parabolic rate law, with its oxidation rates increased with temperature. Based on TEM analyses, an exclusive NiO-layer formed on the BMG surface after the oxidation, and a Pd-rich layer formed beneath the scales. After short-term oxidation at 390°C for 10 min, the amorphous substrate was transformed into three crystalline phases of Pd_3P, Ni_3P, and Ni_2Pd_2P. Indicaticy the occurrence of the substrate phase-transformation at the initial-stage oxidation.

Keywords： Pd-based BMG； parabolic rate law； enriched zone； NiO.

國科會編號：NSC 95-2218-E-110-006

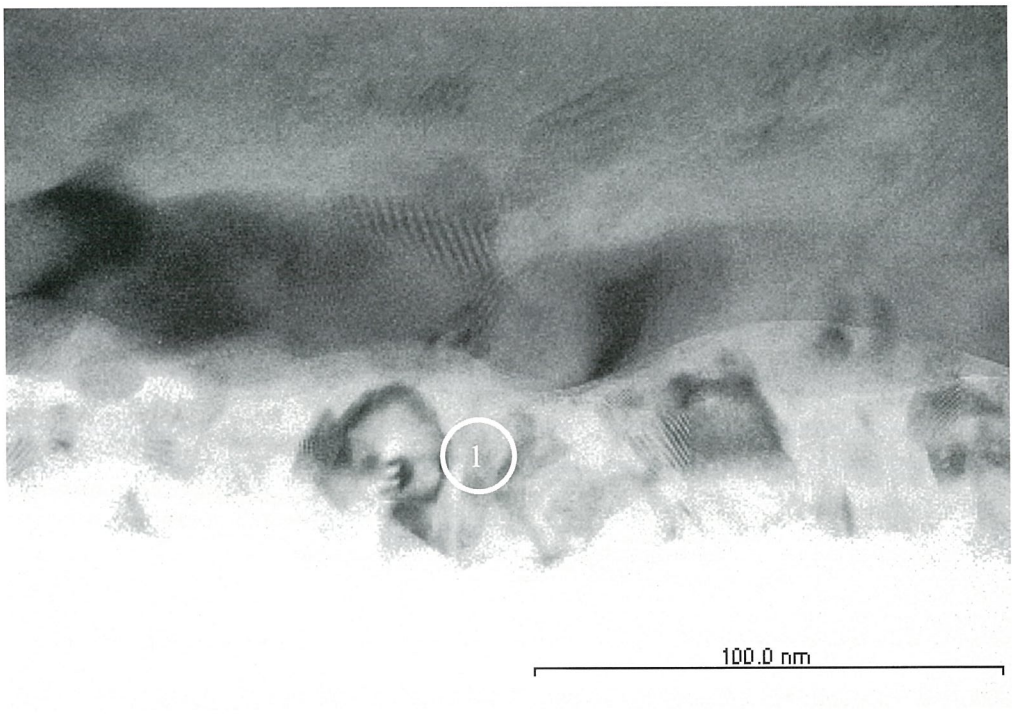

(a)

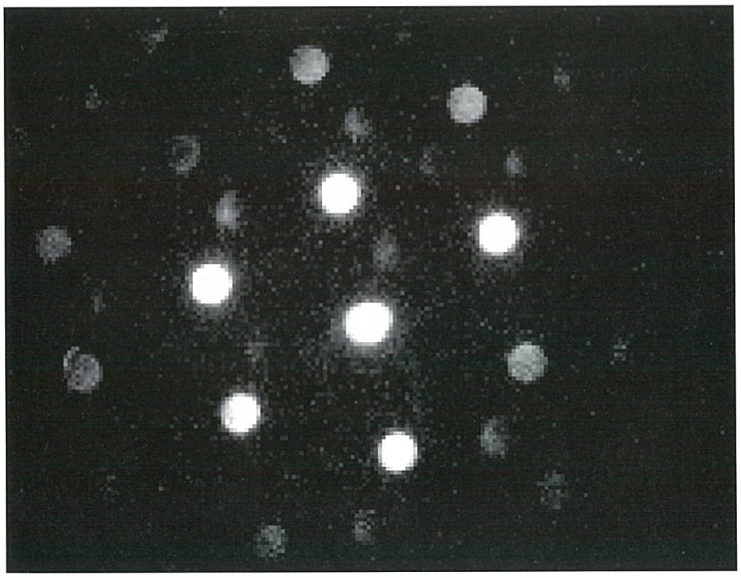

(b)

Fig. (a) TEM cross-section of the scales formed on the Pd-BMG oxidized for 48 h at 420°C, (b) SAD of region 1.

(img 0417_01.tif & 0417_05.tif)

TRUCTURE EVOLUTION OF A Ti-Mo CONTAINING STEEL

芳歆); Chen, Chih-Yuan (陳志遠); Li, Wei-Chi (李威志); Chang,
siao-Tzu (張孝慈) and Yang, Jern-Ren (楊哲人)
ience and Engineering, National Taiwan University, Taipei 100,

rmation involves a series of nucleation events and then partition of
to surrounding austenite matrix, which can generate bainite ferrite
amounts of sub-units [1]. Two main strengthening methods can be
fectively, namely tiny grains (i.e. sub-units) and high density of
ed austenite after bainite transformation can be divided into two
retained austenite and blocky retained austenite. It is generally
ky retained austenite would transform into martensite during the
cess, which could generate hard and brittle marteniste. Bhadeshia has
three methods to reduce the quantity of blocky retained austenite in
is generally accepted that reducing carbon content of austenite by
tly and powerful method to attain this goal, and would be the subject

composition of present steel is based on the
2Ti-0.2Mo (wt%). The specimen was heated into 1200℃ for 3 min,
to 550℃ for isothermal aging treatment with 5 min, 10 min, and 60
1 shows martensite microstructure obtaining form the quenching
at the partition of carbon atoms into the retained austenite during the
s can enrich of carbon content in the retained austenite, which can
rteniste during the quenching process. Fig. 2 reveals the carbides near
which can grow by pipeline diffusion of carbon atoms through a lot of
e more microalloy carbide precipitation in the austenite region can be
blocky retained austenite. Beside precipitation in the austenite region,
y elements would be precipitated at dislocation in the bainite ferrite
h the bainite ferrite matrix effectively. Fig. 3 presents the nano-sized
location and with the three variants of B-N OR between carbide and
pearlite structure in the steel after longer time aging (60min). It is
te structures would be generated from decomposition of blocky and

, Acta Metall., 1980, Vol. 28, pp. 1103-1114.
, Bainite in Steels, IOM Communication, 2001, 2nd edn, pp.375.

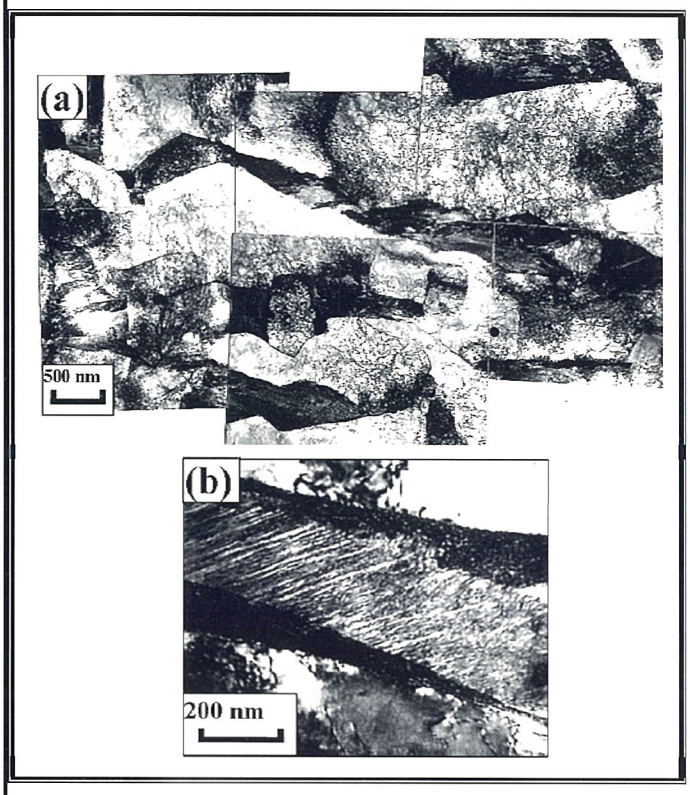

Fig. 1.TEM showing martensite obtained from retained austenite after aging at 550℃, 60min.

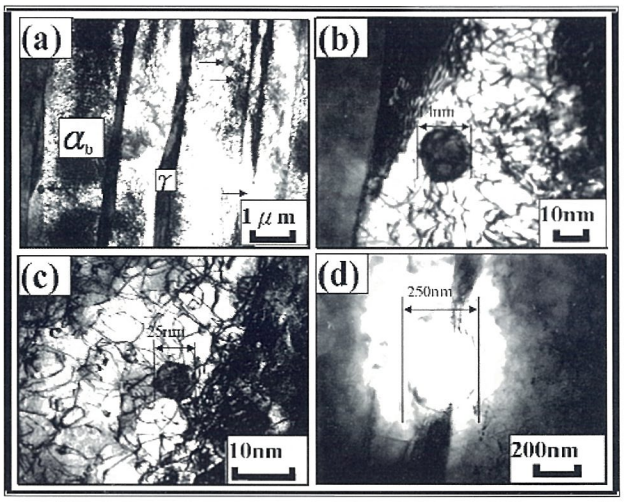

Fig. 2. TEM image showing spherical carbide Nucleating at dislocation near austenite.

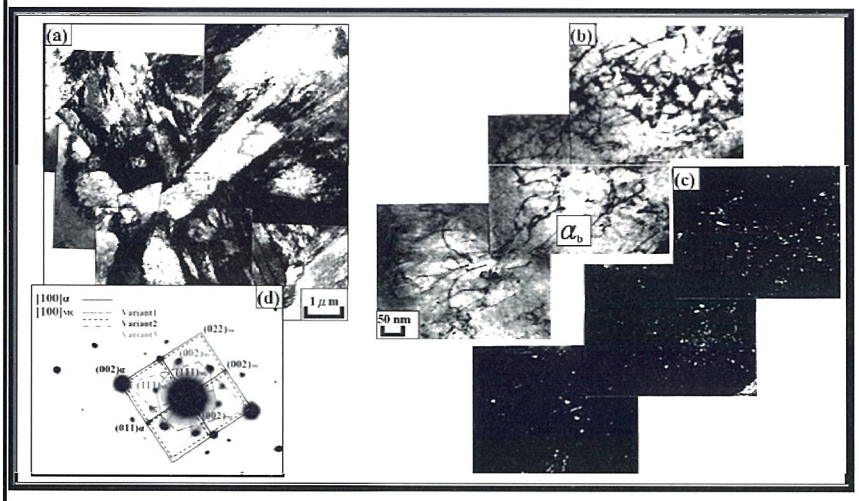

Fig. 3. TEM image showing nano-sized carbide precipitation at dislocation

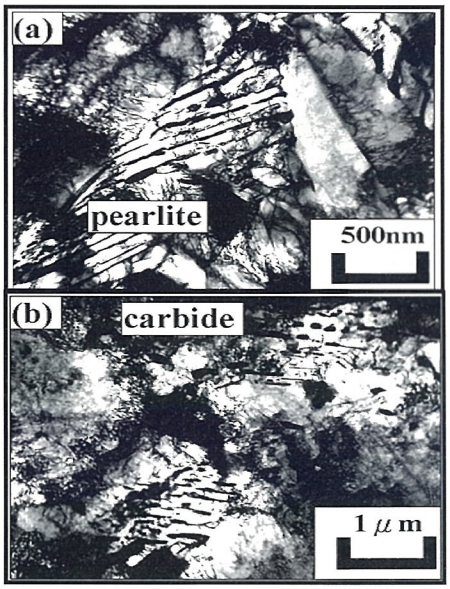

Fig. 4. Decomposition of blocky and film retained austenite during isothermal aging

M-P-19: TEM INVESTIGATION ON A GALVANEALLED DUAL PHASE STEEL

Kao, Fang-Hsin (高芳歆); Chen, Chih-Yuan (陳志遠) and Yang, Jern-Ren (楊哲人)

Institute of Materials Science and Engineering, National Taiwan University, Taipei 100, Taiwan.

It has been attracted attentation in developing advanced high strength steel (AHSS) for automobile industry to reduce vehicle weigh, save fuel efficiency, and protect passenger safety [1]. Among these AHSS steels, dual phase steel has excellent mechanical property such as high tensile strength, good elongation, and continuous yielding phenomenon, which leads to their vast usage in the out panel of vehicle. On the other hand in order to increase the corrosion resistance of dual phase steel, the galvanealled treatment usually applied in the dual phase steel. The coated Zn layer will become microalloying with the iron matrix and form different types of intermetallic phases among them [2]. The objective of present study is to investigate the microstructure characteristic of galvannealed dual phase steel.

The chemical composition of the present steel is based on the Fe-0.1C-0.01Si-1.5Mn-0.05Mo-0.01P-0.07S(wt%). On the other hand the manufacture process for the galvannealed dual phase steel does not show here due to intellectual property. Fig.1 has shown the SEM microstructure of the galvannealed dual phase steel. Ferrite and martensite has been occurred in the whole microstructure, and the martensite is located within ferrite matrix, which happens mainly due to the thermo-mechanical process. The thickness of coated Zn layer is about 5-10μm, which is expected to possess excellent anti-corrosion property. The twinned martensite appearing in the fig.2 is a result due to partition of carbon atoms from ferrite region during the intercritical treatment. Fig. 3 has revealed the dislocation network occurring in the ferrite grain, which implies the dislocation climbing as well as gliding in the ferrite during the intercritical treatment process. It is expected that smaller ferrite grains would be generated in the hot deformation process, and the remnant dislocation would be annihilated by the following heat treatment process. A distinct ellipsoid precipitate has been observed in the present study, which indicates some precipitation phenomenon happening in the treatment process. However, lack of crystallography and chemical composition data of precipitate restricts the understanding of the precipitate. Therefore it needs some further work to reveal the precipitation behavior of this precipitate. On the other hand the more precise and detail microstructure of coated Zn layer should be analyzed in the near further work.

Reference

1. T. Senuma, Canadian Metallurgiacl Quarterly, Vol. 43, no. 1, 2004, pp. 1-12.
2. T. Nakamori et. al., ISIJ Inter., 1995, Vol. 35, No.12, pp. 1494-1501.

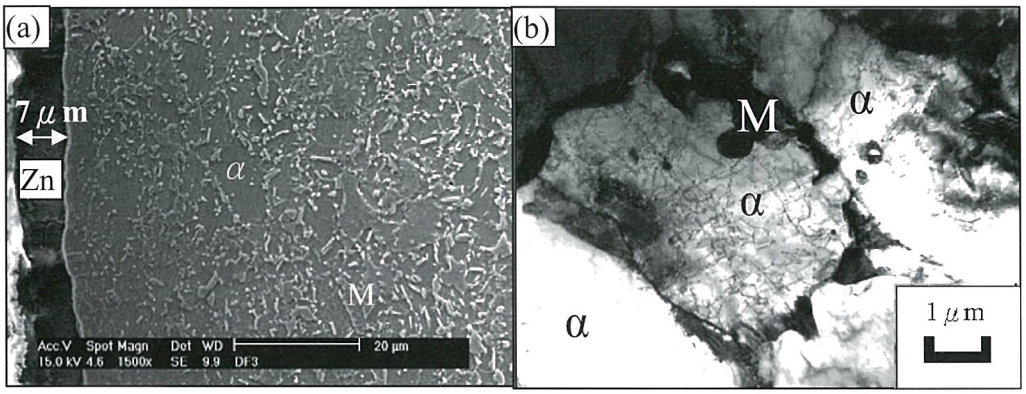

Fig. 1. (a) SEM revealing the microstructure of galvannealed dual phase steel, and (b) TEM image

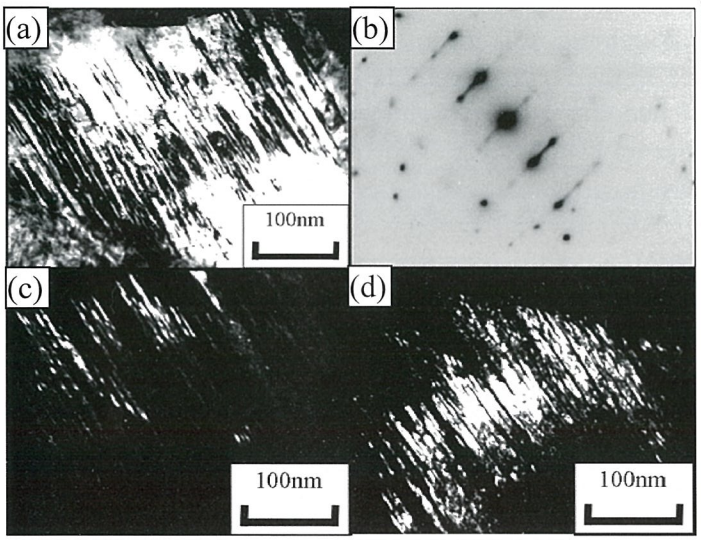

Fig. 2. (a) Twinned martensite image appearing in the retained austenite (b) DP, and (c-d)corresponding dark field image

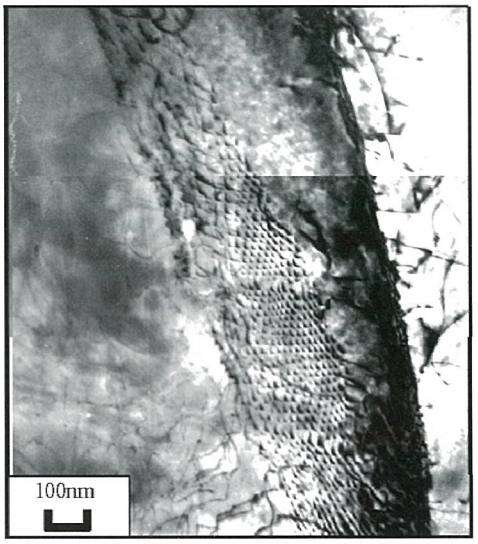

Fig. 3. TEM image showing dislocation network appearing in the ferrite boundary.

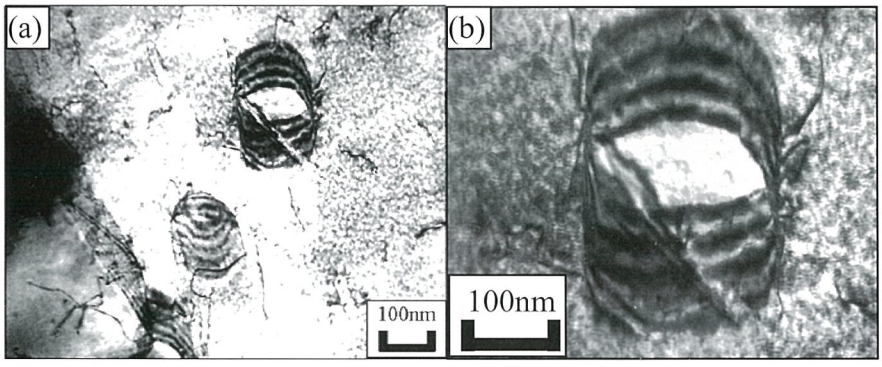

Fig. 4. (a) TEM image revealing precipitates and (b) enlargement TEM image.

M-P-20: THE EFFECT OF INTERRUPTED COOLING TEMPERATURE ON THE PRECIPITATION BEHAVIOR IN THE NOVEL HSLA STEEL

Chen, Chih-Yuan (陳志遠); Kao, Fang-Hsin (高芳歆); Hsu, Cheng-Hsun (許正勳); Li, Xi-Yi (李欣怡) and Yang, Jern-Ren (楊哲人)

Institute of Materials Science and Engineering, National Taiwan University, Taipei 100, Taiwan.

The concept of nano-sized carbide precipitation strengthening in the hot rolled strip has attracted much attention in recent years [1]. However, a lot of microalloying elements would lost in the manufacture processes such as soaking, hot rolling, etc., and it thus reduces the amount of microalloying elements that can be precipitated in the ferrite matrix [2]. Among overall thermo-mechanical process parameters, the coiling temperature is the most important one, which has a large influence determining the precipitation status in the hot rolled strip. Therefore the objective of present study is to investigate the precipitation status and related strengthening effect in the interrupted cooling experiment at fixed cooling rate.

The chemical composition of present steel is based on Fe-0.1C-1.5Mn-0.1Si-0.2Ti-0.2Mo (wt%). The steel was heated to 1200℃ for 3min, directly cooled to interrupted cooling temperatures with cooling rate of 20℃/s, and then directly cooled to room temperature with a fixed cooling rate of 0.5℃/s. The temperature range of interrupted cooling experiment is between 620℃~700℃ In order to realize the effect of hot deformation on the precipitation behavior in the hot rolled strip, the hot deformation structures are investigated in the present study. Figures1-2 have shown the TEM microstructure of steel after interrupted cooling experiments with and without hot deformation. The type of nano-sized carbides in the present research would be supersaturated precipitation carbides and adapt three variants of B-N OR. As the higher migration rate of ledge cannot nucleate interface precipitation carbide, the remaining microalloy elements would be precipitated in the ferrite matrix. Figure 3 presents the variation of microhardness with interrupted cooling temperature, which can be attributed by three different strengthening mechanisms. The decline of microhardness with interrupted temperature in the region I can be explained as follows: the fewer time existing before next phase transformation occurring makes the incomplete precipitation of microalloy carbides in the ferrite matrix and thus reduces the hardening effect. On the contrary, although the higher interrupted cooling temperature can create fully precipitation of microalloy carbide, the large size of carbide reduces the microhardness of ferrite with interrupted cooling temperatures.

1. T. Senuma, Canadian Metallurgical Quarterly, Vol. 43, no. 1, 2004, pp. 1-12.
2. R. D. K. Misra et. al., Materials Science and Technology, 2001, Vol.17, p. 1119.

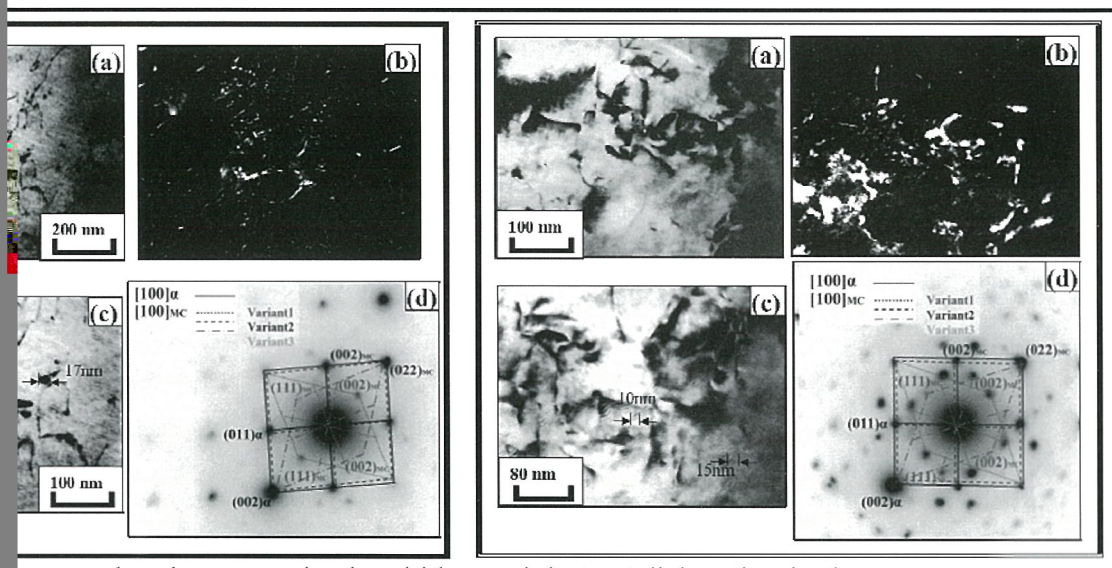

mages showing nano-sized carbide precipitate at dislocation in the
eformation condition when the interrupted cooling temperature at (a) 700℃,
) 680℃

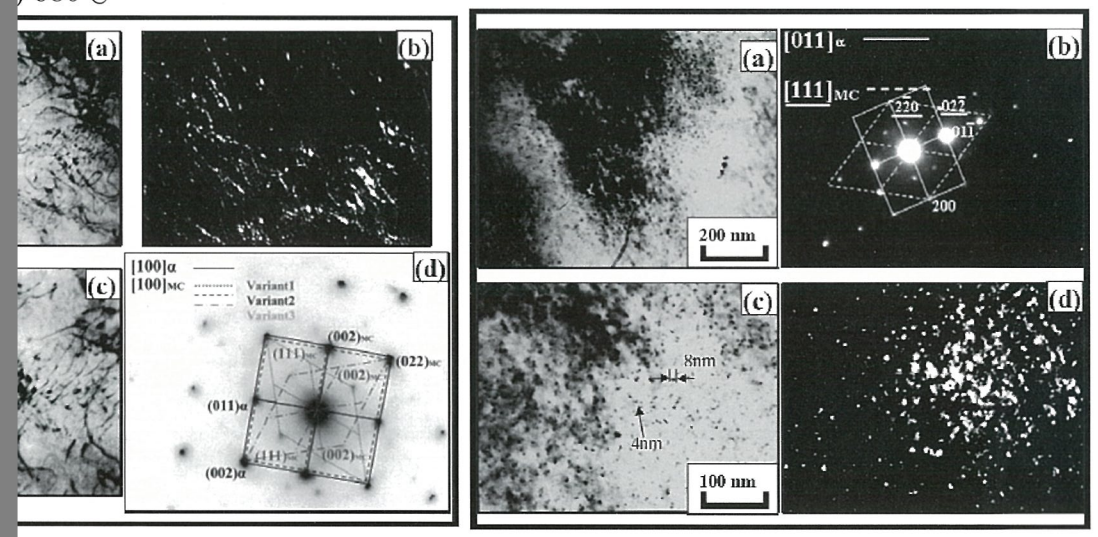

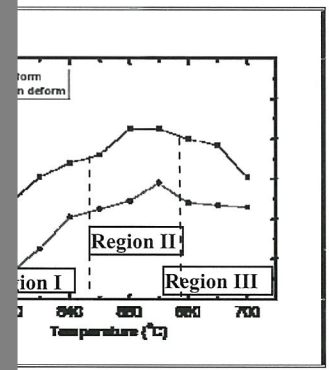

Fig. 3. Microhardnes testing result revealing the variation of hardness with interrupted cooling temperature at different modes, which can be divided into three stages with different strengthening mechanisms.

M-P-21: EFFECT OF NANOCRYSTAL ON THE MEMORY CHARACTERISTICS OF HIGH-κ HfAlO CHARGE TRAPPING LAYERS FOR NANO-SCALE NON-VOLATILE MEMORY DEVICE APPLICATIONS

WANG, T.Y.(王廷玉)[1], S. Maikap[2], YANG, J.R.(楊哲人)[1]
[1]Department of Material Science Engineering, National Taiwan University, Taipei, Taiwan.
[2]Department of Electronic Engineering, Chang Gung University, Tao-Yuan, Taiwan.

Abstract

A HfAlO charge trapping layer with an Al_2O_3 blocking oxide in metal-Al_2O_3-high-κ-SiO_2-Si (MAHOS) structure has been proposed. The high-κ HfO_2 and Al_2O_3 films were formed by atomic layer deposition (ALD). The thickness of HfAlO charge trapping layer was ~10 nm. Then, the Al_2O_3 blocking oxide with a thickness of ~10 nm was deposited in-situ on HfAlO charge trapping layers. To get high charge trapping characteristics as well as large hysteresis memory window, the post deposition annealing (PDA) treatment at 900°C for 1 min in N2 ambient has been performed. The microstructure characteristics of memory devices were carried out using FEI Tecnai F30 field emission gun TEM equipped with EDS detector for high-resolution image and compositional analysis.

The HfAlO charge trapping layers with an Al_2O_3 blocking oxide have large memory window with an excellent retention characteristics. The superior memory characteristics of the HfAlO charge trapping layers can be attribute to charge storage in the nano-grains and it can be used in the semiconductor market for future high-performance nano-scale flash memory device applications.

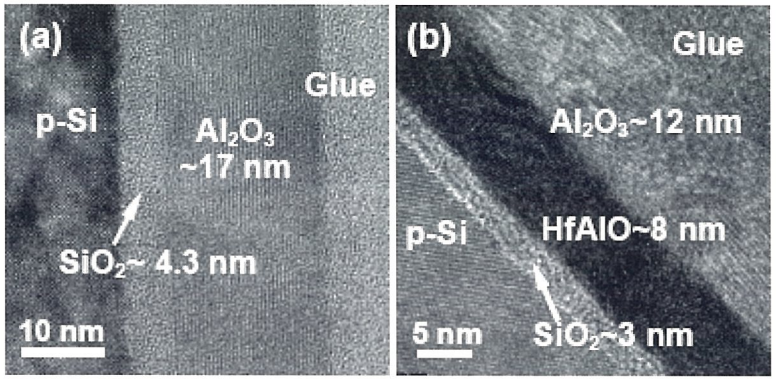

Fig. 1 Cross-sectional TEM images of (a) pure Al2O3 and (b) HfAlO charge trapping layers with an Al2O3 blocking oxide.

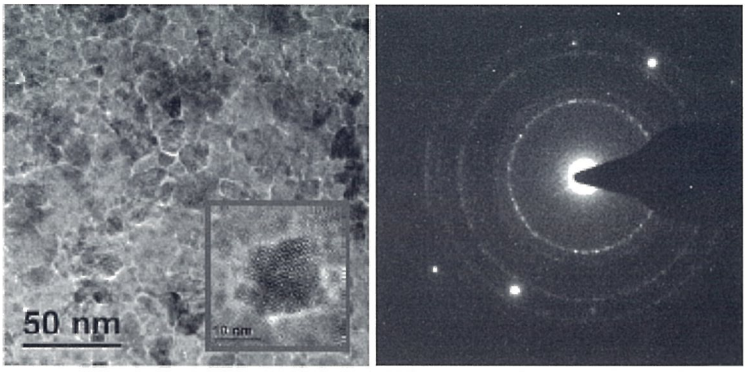

Fig. 2 Plan view TEM and its diffraction pattern on HfAlO layer in p-Si/SiO_2/HfAlO/Al_2O_3 structure shows nano-grains. A single nano-grain is observed in HfAlO layer in the inset.

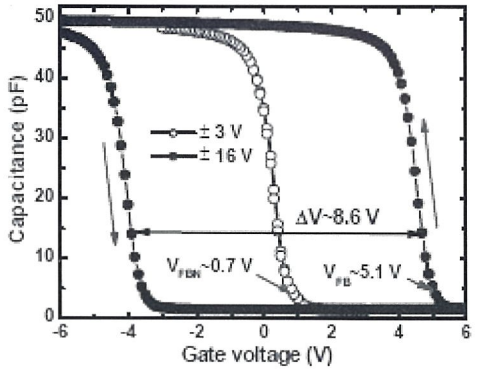

Fig. 3 A large C-V (1MHz) hysteresis memory window is observed for HfAlO charge trapping layer. The hold time was 100 ms during C-V measurement.

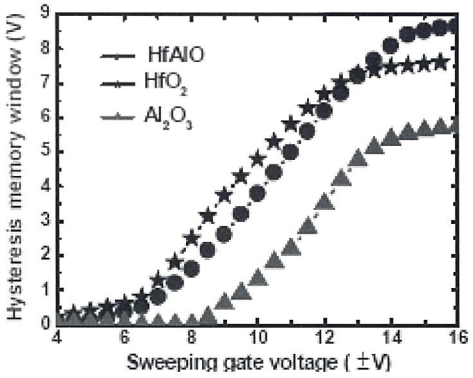

Fig. 4 Hysteresis memory window versus sweeping gate voltage for all memory

M-P-22: NEW CHALLENGES ON TRANSMISSION ELECTRON MICROSCOPY FOR NEW GENERATION GaN-BASED LIGHTTING DEVICES

FENG, Zhe Chuan (馮哲川)[a]; TSAI, Hong-Lin (蔡鴻麟)[b], YANG, Jer-Ren (楊哲人)[b]
[a] Graduate Institute of Electro-Optical Engineering & Department of Electrical Engineering, [b] Department of Materials Science & Engineering, National Taiwan University, Taipei, 106-17 Taiwan, ROC.

Research and developments on GaN-based compound semiconductors and devices for optoelectronic and electronic applications have been very active in recent years. A great deal of breakthroughs have been achieved in recent years for their materials growth and device manufactures in versatile applications of blue-UV and visible light emitting diode (LED), laser diode (LD) and other optoelectronic and electronic devices [1]. It is promising to achieve energy-saving and environmentally friendly solid-state light sources from GaN-based quantum structural materials [2].

InGaN/GaN multiple quantum wells are the key components of these commercial devices emitting green, blue, near-UV, and white light, acting as the active layer, which can exhibit intense photoluminescence (PL) and electroluminescence (EL) despite of a high dislocation and defects density existed, and have advantages such as lowering the threshold current density for LDs and reducing the device sensitivity to temperature. However, the mechanism of luminescence from InGaN/GaN is not yet well-understood and the physical origin of efficient light generation in this material system is unveiled incompletely, and there are still a lot of puzzling phenomena whose origin has yet to be explored, which is very important, not only from the viewpoint of physical interest but also in designing practical device [2-3].

It has been suggested by many authors that its remarkable efficiency results from the carrier localization effect caused by In-fluctuation in QW, or phase-segregation effects, related to spinodal decomposition. The formed nm-scale quantum-dot (QD)-like structures lead to exciton localization in InGaN.

High resolution transmission electron microscopy (HRTEM) is a key technology in study these structural features associated with the luminescence mechanisms. We have identified the interfaces between InGaN and GaN layers in the high quality MQWs being abrupt and the In-rich precipitates caused by alloy fluctuation appeared as the regions with a dark contrast can be attributed to the In-poor region. A HRTEM cross-sectional low magnified high-angle annular dark field (HAADF) STEM image technique can applied to expose better the main features in InGaN/GaN MQWs.

Figure 1 shows a HRTEM image from a MOCVD-grown InGaN-GaN MQW LEDs. The interfaces between GaN and InGaN layers in QWs are abrupt. The In-rich precipitates can be seen, which are caused by alloy fluctuation appeared in the regions with a dark contrast. The HR image shows no threading dislocation at this area, but some strain field around the well.

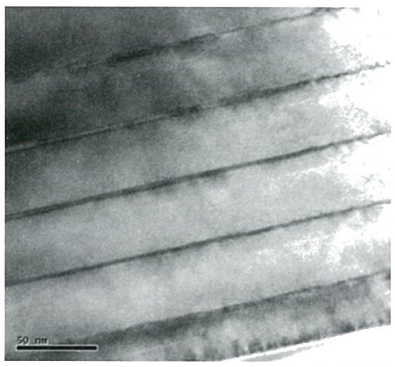
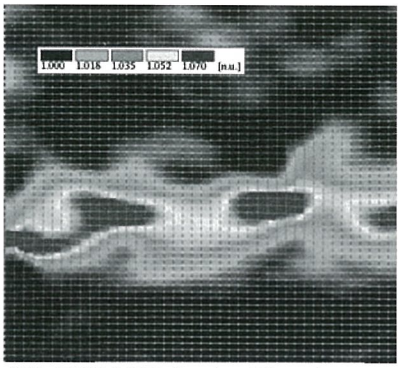

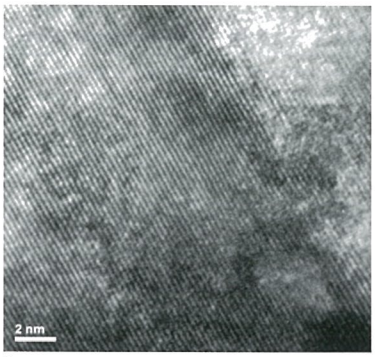

Fig. 1. HRTEM images from an InGaN-GaN MQW LED (scale: 50-nm) --- left.
Fig. 2. TEM DALI images of an InGaN QW -- middle.
Fig. 3. HRTEM image from an InGaN MQW LED (scale: 2-nm) -- right.

Figure 2 shows the TEM digital analysis of lattice images (DALI), obtained from cross-section HRTEM. To avoid specimen degradation during electron-beam irradiation, the exposure time before image recording was kept smaller than 1 min. They exhibit the color-coded map of the local In-concentration inside QW structure, and the inhomogeneity of the QW layer, thickness, indium composition and well-to-well. The quantum dot (QD) - like structures around the In-rich areas are formed, which is the cause of strong luminescence from InGaN/GaN MQWs.

Figure 3 exhibits a HRTEM from another LED on a QW area, with the In-clustering seen clearly. These nano-structural or QDs features are closely correlated with results from HRXRD, and optical data.

There appears a hot discussion on the mechanism or origin of luminescence from InGaN/GaN [2,4,5]. C. J. Humphreys and co-authors have suggested [4] that the contrast observed in many HRTEM images is to a large extent a consequence of exposure to the electron beam and is not due to the presence of In-clustering, that strong luminescence from the carrier localization is possible due to monolayer well width fluctuations with a lateral scale of about 2 nm. They also postulate [5], by observing the gross well-width fluctuations in single InGaN/GaN QWs and interlinking strips of InGaN with In-rich centers, that excitons are localized at these In-rich regions preventing them reaching threading dislocations.

Our work provides new insights of physics on the luminescence mechanism of InGaN/GaN MQWs. Our HRXRD data [3] showed fine oscillation corresponding to atomic layer variation of ~3Å, which might question on the mechanisms from Humphreys et al [4,5].

The exploration and investigation on GaN-based quantum structures would raise new challenges for the TEM technology and new developments.

References

[1] Zhe Chuan Feng, ed., GaN-Based Materials: Growth and Characterization, Imperial College Press, London, 2006.
[2] S. M. de S. Pereira, K. P. O'Donnell and E. J. da C. Alves, Advanced Functional Mat. 17 (2007)37.
[3] Z. C. Feng, B. Xue, P. Chen, J. Lin, W. Lu, N. Li and I. T. Ferguson, Proc. SPIE 6321(2006) 63210H.
[4] M. J. Galtrey, R. A. Oliver, M. J. Kappers, C. J. Humphreys, D. J. Stokes, P. H. Clifton and A. Cerezo, Appl. Phys. Lett. 90(2007)061903.
[5] N. K. van der Laak, R. A. Oliver, M. J. Kappers and C. J. Humphreys, Appl. Phys. Lett. 90(2007)121911.

M-P-23: **TREATMENTS FOR ENHANCING CHEMICAL AND PHYSICAL PROPERTIES OF ANODIC TITANIUM OXIDE FILM**

CHEN, M. T.(陳懋德), Liu, J. H.() and Lin C. S. (林招松)

Department of Materials Science and Engineering, National Taiwan University, Taipei 106 Taiwan

Anodic oxidation of titanium in the specific electrolyte containing calcium and phosphorus compounds can prepare a calcium- and phosphorus-containing oxide film, which results in further formation of crystallized hydroxylapatite after hydrothermal treatment. Beside, previous researches also indicated that during the galvanostatic anodizing process, the chemical contents of the anodic films could be enhanced when increasing the anodizing voltage. More hydroxylapatite can be fabricated with richer contents of calcium and phosphorus in the anodic film. Surface roughness of the anodic film, which has major effects on the behavior of cell growth after being implanted in human body, can also be optimized with higher anodizing voltage because of the phenomenon of micro-arc oxidation during anodizing[1-4].

However, beside the chemical contents and the surface roughness of the anodic film, other mechanical properties of the anodic film should be another important concern. When increasing the anodizing voltage, the anodic film would have some better properties, but the adhesion of the anodic film with the substrate would decrease on the contrary. It is because that a pore-containing layer and a crater-containing layer were formed prior to and during micro-oxidation[5]. Both layers would result in some interior defects in the anodic film and cause the anodic film be peeled off after implantation.

In order to prevent this side effect, some treatments to enhance the properties of the anodic film without the relatively higher anodizing voltage were designed in this study. A biomimetically-formed film was desired to be coated as the overlay via immersion in simulated body fluid (SBF). Formation of hydroxylapatite on the anodic film was directly related to the existence of triorthophosphate ions[6]. However, diorthophosphate ion, but not triorthophosphate ion is the dominant phase in SBF[7]. In this case, alkali- and heat-treatment before SBF immersion was designed to accelerate the reactions in SBF. It was considered that a high pH zone was formed near the surface of the anodic film when it was immersed in SBF.

Reference

1. Ishizawa H and Ogino M, *J Biomed Mater Res.*, **29**, 65 (1995).
2. Ishizawa H and Ogino M, *J Biomed Mater Res.*, **29**, 1071 (1995).
3. Fini M, Cigada A, Rondeli G, Chiesa R, Giardino R, Giavaresi G, Aldini N, Torricelli P and Vicentini B, *Biomaterials*, **20**, 1587 (1999)
4. Takebe J, Itoh S, Okada J and Ishibashi K, *J Biomed Mater Res.*, **51**, 398 (2000).
5. Lin CS, Chen MT and Liu JH, accepted from *J Biomed Mater Res.*, (2007).
6. Lu X and Leng Y, *Biomaterials*, **26**, 1097 (2005).
7. Pourbaix M, *Atlas of Electrochemical Equilibria in Aqueous Solutions, 2nd ed.*, NACE, Houston, Texas (1974).

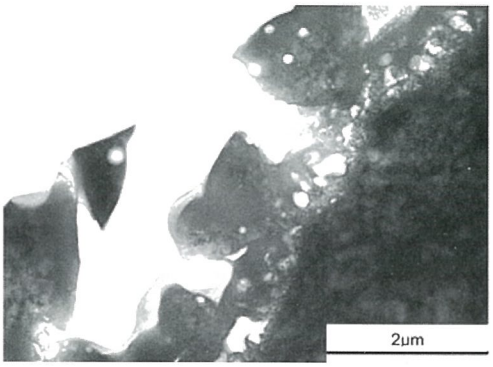

Figure 1 Cross-sectional TEM image of the anodized specimen.

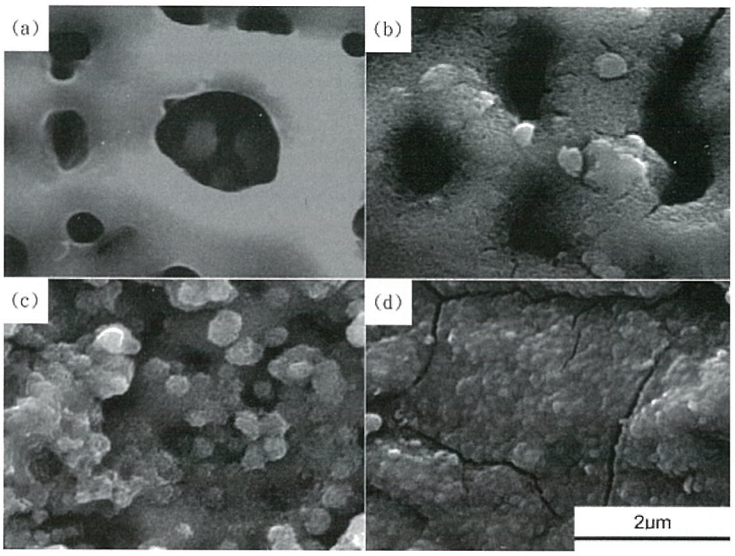

Figure 2 Surface morphologies of the (a) anodized specimen and being performed in order of (b) alkali- and heat-treatment, (c) reverse pulse plating and (d) SBF immersion.

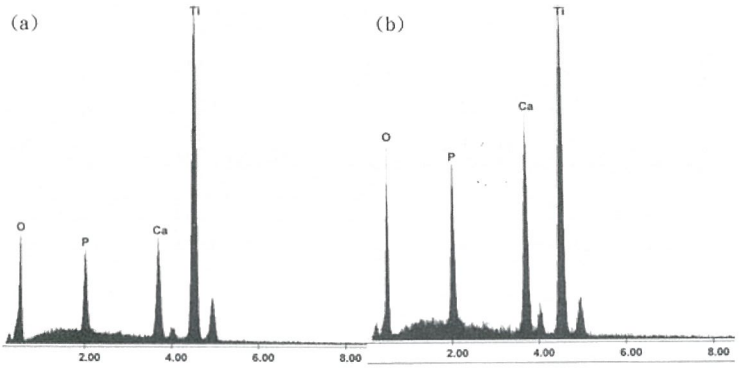

Figure 3 EDS spectrums taken from (a) as-anodized titanium specimen and (b) the titanium specimen performed with alkali- and heat-treatment and SBF immersion

B-P-1: THE AUTONOMOUS NOTCH SIGNAL PATHWAY IS ACTIVATED BY BAICALIN AND BAICALEIN BUT IS SUPPRESSED BY NICLOSAMIDE IN K562 CELLS

WANG, An-Ming (王安民); LEE, Shao-Pei (李紹珮); LIAO, Wan-Ru (廖婉如) and YEH, Tien-Shun (葉添順)

Institute of Anatomy and Cell Biology, School of Medicine, National Yang-Ming University, Taipei 112, Taiwan.

Notch signal pathway plays important roles in a wild variety of cellular processes. Therefore, the aberrant transduction of Notch signaling contributes to many diseases and cancers of human. The Notch receptor intracellular domain, the activated form of Notch receptor, is extremely difficult to detect in normal cells. However, it can elicit biological effects at a very low protein concentration. In the present study, a cell-based luciferase reporter gene assay was established in K562 cells to screen drugs which modulate endogenous CBF1-dependent Notch signal pathway. Using this system, we found that the luciferase activity of CBF1-dependent reporter gene was activated by baicalin and baicalein but was suppressed by niclosamide. The treatment with baicalin, baicalein, and niclosamide affected the mRNA expression of Notch1 receptor to modulate the endogenous Notch signaling in K562 cells. Additionally, erythroid differentiation of K562 cells was suppressed by baicalin and baicalein but was promoted by niclosamide. By colony-forming assay in soft agar, the colony number was decreased after the treatment with baicalin and baicalein in K562 cells, but was not affected in the presence of niclosamide. Taken together, the endogenous Notch signal pathway is modulated in K562 cells by baicalin, baicalein, and niclosamide. The modulation of Notch signaling after the treatment with these drugs may affect erythroid differentiation and ability of colony formation in K562 cells. Therefore, this system could be beneficial for the screening of drugs with the potential to treat Notch signal pathway-associated diseases for therapeutic purposes.

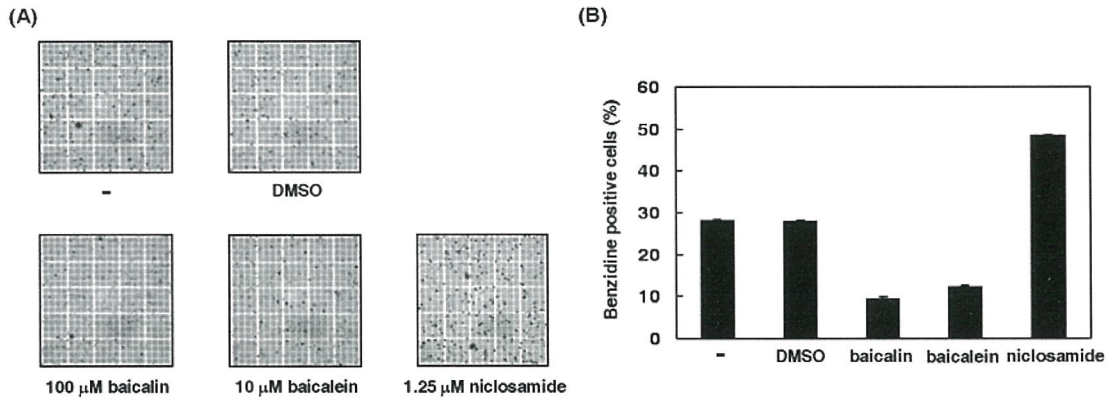

Fig. 1. The erythroid differentiation of K562 cells is suppressed by baicalin and baicalein and is enhanced by niclosamide. Scale bar = 0.2 mm

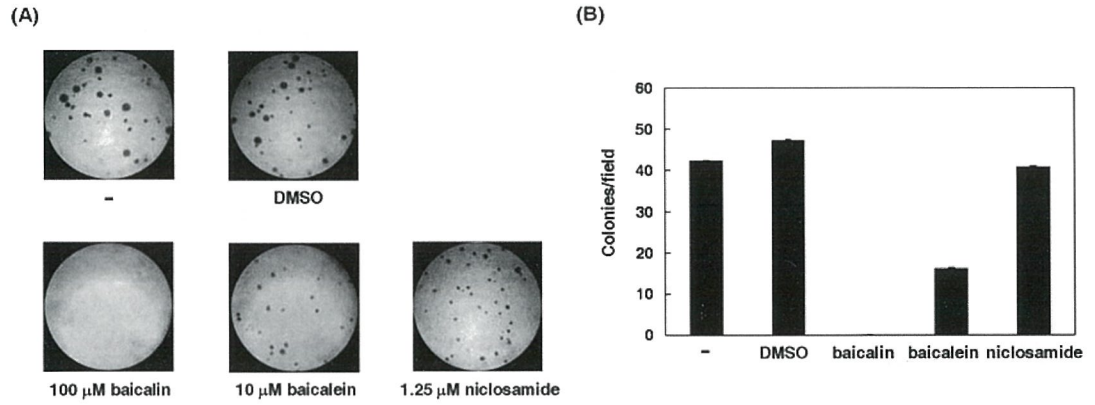

Fig. 2. The ability of colony formation in K562 cells is suppressed by baicalin and baicalein, but not niclosamide. Scale bar = 1.0 mm

B-P-2: NEOVASCULARIZATION AND MORPHOLOGICAL CHANGES IN THE PRENATAL DEVELOPING AND LASER INDUCED RATS

LU, Min (呂旻)[a]; CHEN, Yu-Lin (陳羽琳)[a]; YANG, Chen-Chang (楊正昌)[a]; CHEN, Yi-Ting (陳宜婷)[a]; YANG, Chang-Shu (楊昌叔)[b] and YU,Shang-Ming (游祥明)[a]

[a]Institute of Anatomy and Cell Biology, National Yang-Ming University,

[b]Department of Ophthalmology, Taipei Veterans General Hospital

Age-related macular degeneration (ARMD) is a pathologic change in the macula with age progressed and causes severe visual loss and even blindness. There are two types of ARMD, the dry form and wet form. The dry form comes from drusen formation and accumulation between RPE and Bruch's membrane; the wet form comes from the choroidal neovasculorization (CNV) resulting in the hemorrhage and scar formation. In this study, we use the didode laser applying on the eyes of the Brown Norway rats to investigate the formation of the neovascularization. Under the ophthalmoscope, FITC-Dextran with 10% gelatin perfusion are used to observe the lesions and the morphological change of blood vessels after the laser administration. The animals were sacrificed at 2, 4, 7, 10, 14 and 28 days after laser injury and embedded with paraffin for morphologic investigations of the retina and the choroid. The lesioned site revealed a distinct boundary accompanying with a hemorrhage at the start of laser injury. The lesioned areas became diffused and gradually reduced their sizes at postlesion day 7. At postlesion day14, the contour of the newly-formed blood vessels became more discernible than those of postlesion day 7. Under the light microscopy, there was the leakage of the erythrocyte from the blood vessel of the choroids invading into their adjacent area at postlesioned day 2. At postlesioned day 4, an accumulation of the erythrocyte was replaced by a small amount firbrocyte. At postlesioned day 7, some of the firbrovascular tissue became basophilia in the H.E. stained sections. The large pigmented cells occurred in the firbrovascular tissue. At postlesioned day 10, a distinct blood vessel were found in the firbrovascular tissue. Till the 28 day, more vessels were formed and the RPE appeared to form a barrier between the fibrovascular tissue and the retina.

References

[1] O. Strauss. Physiol Rev. 85(2005)845

[2] P.F. Lopez, B.D. Sippy, H.M. Lambert, A.B.Thach and D.R.Hilton. Invest Opthaloml Vis Sci. 37(1996)855

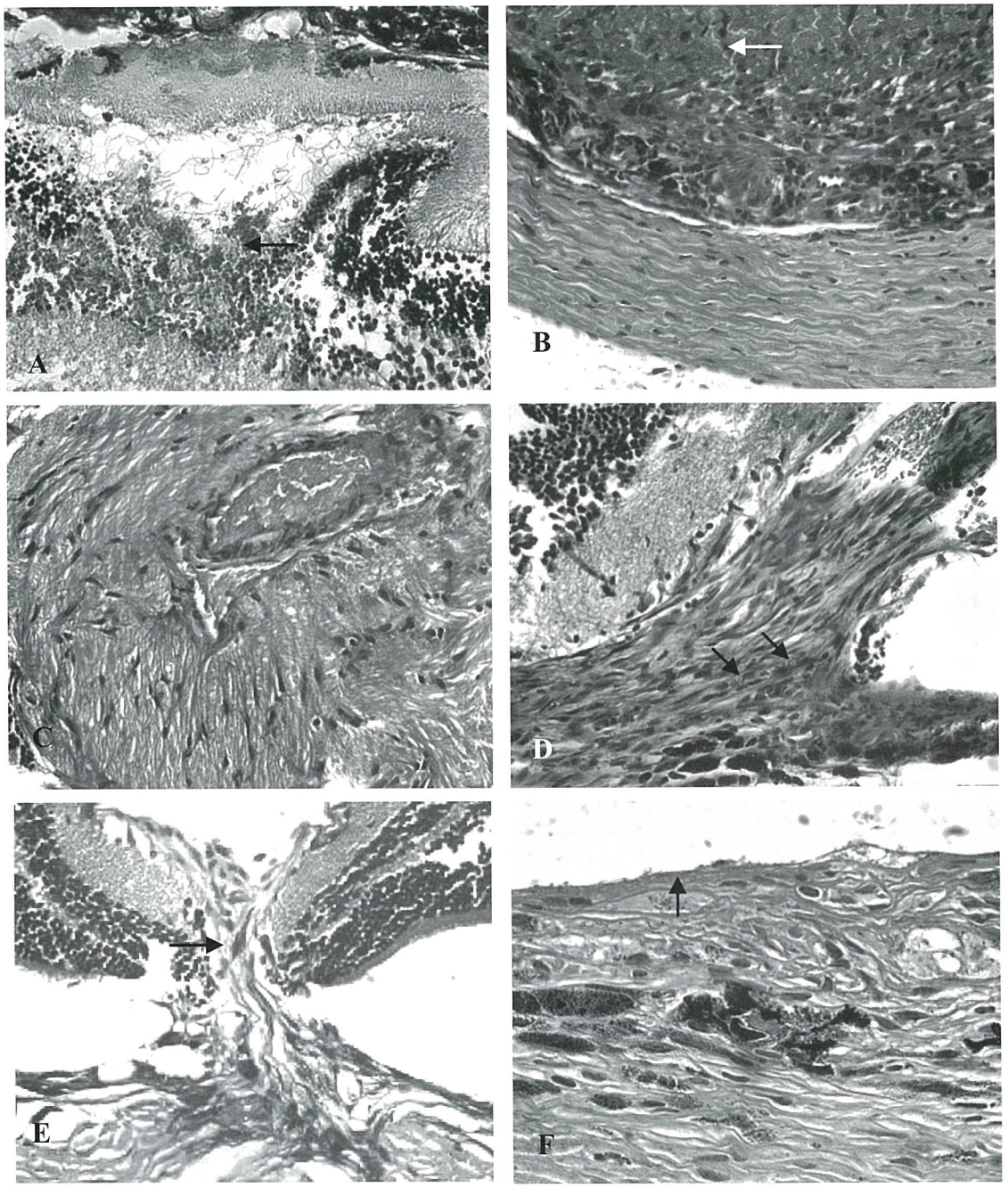

Fig. Form A (postlesioned day 2) to F (postlesioned day 28) revealed the morphological changes after laser application.

B-P-3: THE APPLICATION OF THE MESENCHYMAL STEM CELLS IN WHARTON'S JELLY OF THE HUMAN UMBILICAL CORD ON TREATMENT FOR ISCHEMIA/REPERFUSION STROKE OF RAT

LIN, Yu-Ching (林于晴) ; FU, Yu-Show (傅毓秀)
Institute of Anatomy and Cell Biology, National Yang-Ming University, Shih-Pai, Taipei 112, Taiwan.

Stroke is a leading cause of death and disability. But, despite intensive research, few treatment options exist. A promising strategy for the treatment of stroke is transplantation of stem cells. We have shown that human umbilical mesenchymal cells in Wharton's jelly (HUMSCs) possess stem cell properties. We previously demonstrated that 87% of HUMSCs could be induced to differentiate into neurons, expressing neurofilament, functional mRNAs responsible for the syntheses of subunits of the kainate receptor and glutamate decarboxylase and generating an inward current in response to evocation by glutamate. HUMSCs can be easily obtained and processed, compared to embryonic and bone marrow stem cells. We also found that the transformed HUMSCs in the striatum were still viable 4 months after transplantation without the need for immunological suppression, suggesting that HUMSCs might be a good stem cell source for transplantation.

In this study, we test the potential of transplantation of HUMSCs in the ischemic brain. In our preliminary data, transplanted HUMSCs survived robustly in rat ischemic brain, and significantly decreased the infracted brain area. Furthermore, the behavioral assay and underlying mechanism will also be investigated.

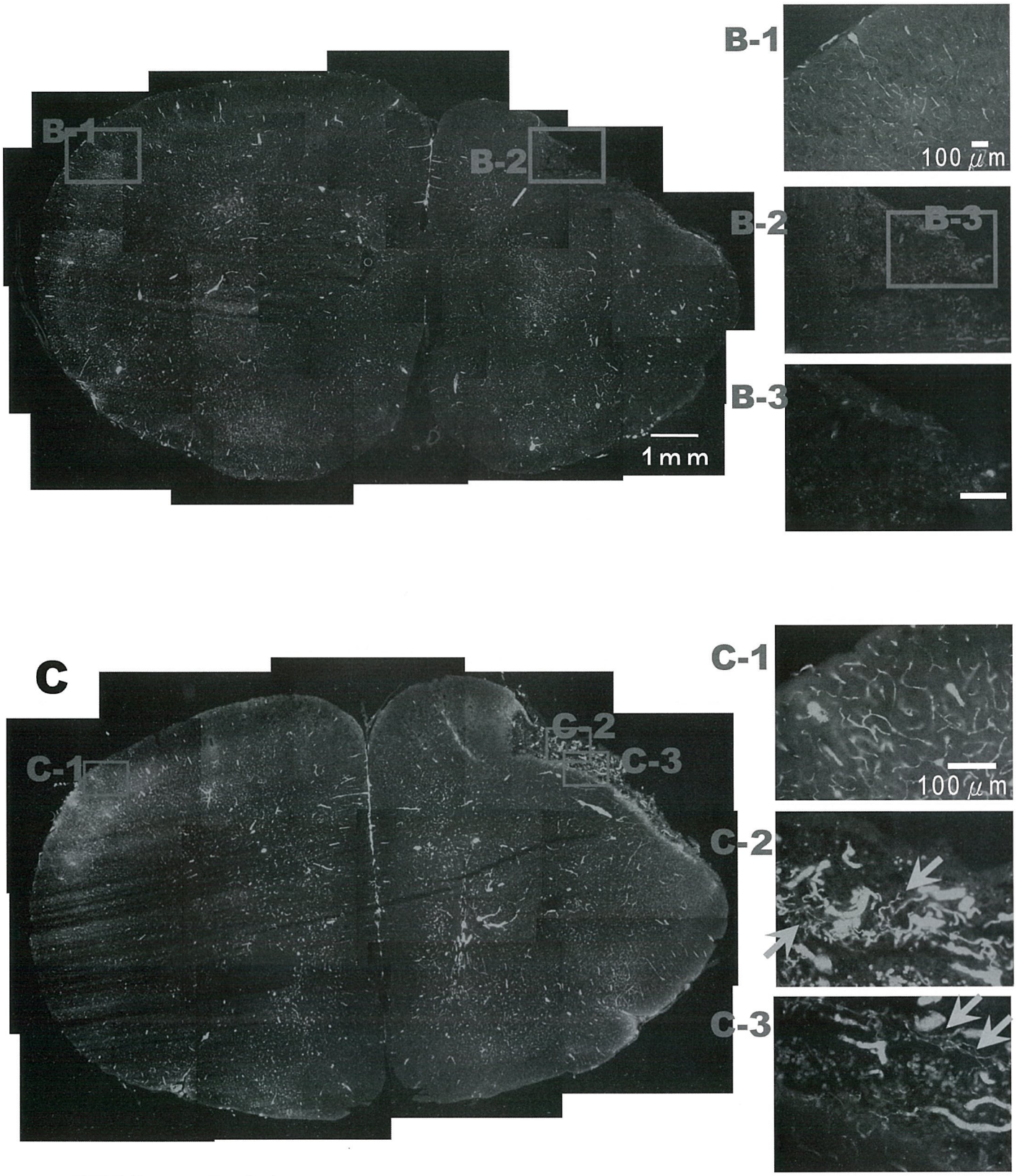

FITC-Dextran Perfusion

B-P-4: THE STUDY OF STAMINATE AND HERMAPHRODITE FLOWERS ON FLORAL DEVELOPMENT AND MICROSPOGENSIS IN *KOELRETERIA HENRYI* DUMMER (SAPINDACEAE)

Lin, Chiou-Huey (林秋惠)[a]；Su-Hwa Chen(陳淑華)[b]

[a]Inst. Ecology and Evolutionary Biology. National Taiwan University. Taipei 100, Taiwan.

[b]Dept. Life Science, National Taiwan University. Taipei 100, Taiwan.

Koelreuteria henryi Dummer (Sapindaceae) is a deciduous tree and endemic to Taiwan. This species has been widely cultivated as road tree. It is andromonoecious system with staminate and hermaphrodite flowers on the same plant, fertile and steril pollen grains were produced respectively. In this study, with the aids of LM, TEM, SEM and histochemical observations, it is attempted to reveal (1) the floral initiation and sex expression in per inflorescence; (2) the similarity and dissimilarity in pollen morphology, pollen viability and cytoplasmic content in staminate and hermaphrodite flowers; (3) the cellular and organellar transformations during the microsporogenesis; and (4) the anther and pollen wall configuration at anthesis.

The early flower buds have both the stamen and pistil primordia. that all flowers' sex differentiation in K. henryi are potentially bisexual and only at the final stage of development sex organs could be define.

Although the pollen grains from hermaphrodite flowers exhibited ca. 15.3 % viability when tested with FCR reaction, no pollen grain germinated in vitro. In constrast, those pollen grains from the staminate flowers have higher germination rate (76.8 %) tested in vitro. The results of histochemical staining show that there is a remarkable difference in storage compounds between sterile and fertile pollen grains. In the former, lipids globules with fewer starch grains are detected in the cytoplasm, while in the latter, only lipid globules are detectable.

The secretory tapetum has two organelles involved in production of lipid droplets were endoplasmic reticulum (ER) (Fig. A) and elaioplast (Fig. B). At maturation stage, the plastoglobules (Fig. C) are released from elaioplasts and coalesced with oleosomes to form the pollenkitt (Fig. D) mass deposited on the exine.

In the intine (I) of aperture, three strata can be made out (Fig. E). Sterile pollen grains have thickness intine and exine in the aperture uaually un-disappeared (Fig. F).

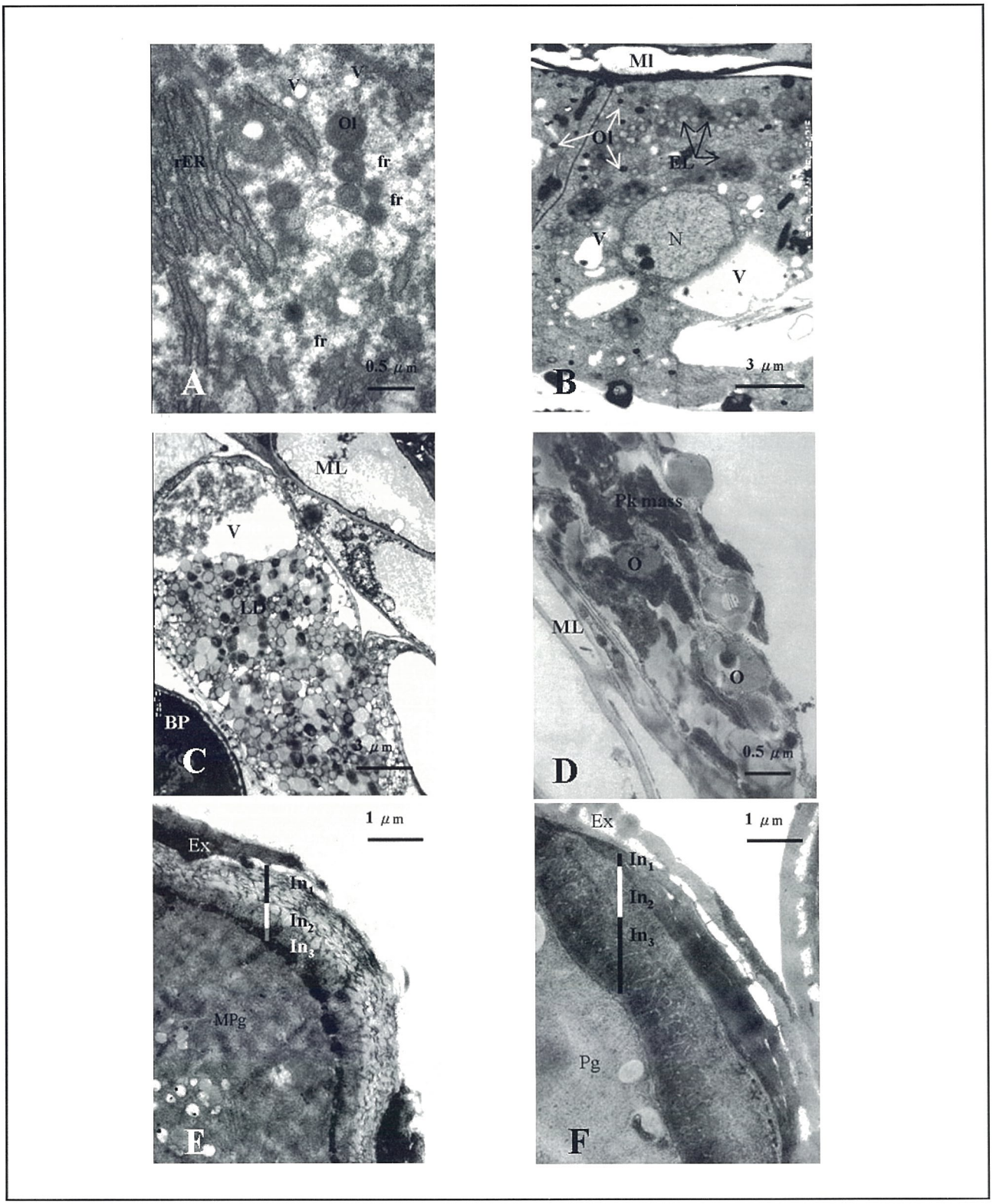
V
V
Ol
rER
fr
fr
fr
0.5 μm
A
Ml
Ol
EL
V
N
V
3 μm
B
ML
V
LD
BP
3 μm
C
Pk mass
O
ML
O
0.5 μm
D
1 μm
Ex
In1
In2
In3
MPg
E
Ex
1 μm
In1
In2
In3
Pg
F

B-P-5: INVOLVEMENT OF ENDOPLASMIC RETICULUM STRESS-MEDIATED SIGNALS IN β-LAPACHONE-INDUCED APOPTOSIS

KE, Ying-Ru (柯穎如)[a]; Lien, Yi-Chen (連宜珍) and CHAU, Yat-Pang (周逸鵬)[a]
[a]Institute of Anatomy and Cell Biology, School of Medicine, National Yang-Ming University, Shih-Pai, Taipei 112, Taiwan.

β-Lapachone, an *o*-naphthoquinone, induces various carcinoma cells to undergo apoptosis, but the mechanism is poorly understood. In the present study, we found that the β-lapachone-induced apoptosis of DU145 human prostate carcinoma cells was associated with endoplasmic reticulum (ER) stress, as shown by increased intracellular calcium levels and induction of GRP-78 and GADD-153 proteins, suggesting that the ER is a target of β-lapachone. β-Lapachone-induced DU145 cell apoptosis was dose-dependent and accompanied by cleavage of procaspase-12 and phosphorylation of p38, ERK, and JNK, followed by activation of the executioner caspases, caspase-7 and calpain. However, pretreatment with the general caspase inhibitor, z-VAD-FMK, or calpain inhibitors, including ALLM or ALLN, failed to prevent β-lapachone-induced apoptotic cell death. Blocking the enzyme activity of NQO1 with dicoumarol, a known NQO1 inhibitor, or preventing an increase in intracellular calcium levels using BAPTA-AM, an intracellular calcium chelator, substantially inhibited the MAPK phosphorylation, abolished the activation of calpain, caspase-12, and caspase-7, and provided significant protection of β-lapachone-treated cells. These findings show that β–lapachone-induced ER stress and MAP kinase phosphorylation is a novel signaling pathway underlying the molecular mechanism of the anticancer effect of β-lapachone.

References

[1] Don, M.J., Chang, Y.H., Chen, K.K., Ho, L.K., Chau, Y.P. Mol. Pharmacol. 2001, (59) 784-794.

[2] Rao, R.V., Peel, A., Logvinova, A., del Rio, G., Hermel, E, Yokota, T., Goldsmith, P.C., Ellerby L M, Ellerby H.M., Bredesen, D.E. FEBS Lett. 2002, (514) 122-128.

[3] Reinicke, K.E., Bey, E.A., Bentle, M.S., Pink, J.J., Ingalls, S.T., Hoppel, C.L., Misico, R.I,, Arzac, G.M., Burton, G., Bornmann, W.G., Sutton, D., Gao, J., Boothman, D.A.. Clin. Cancer Res. 2005, (11) 3055-3064.

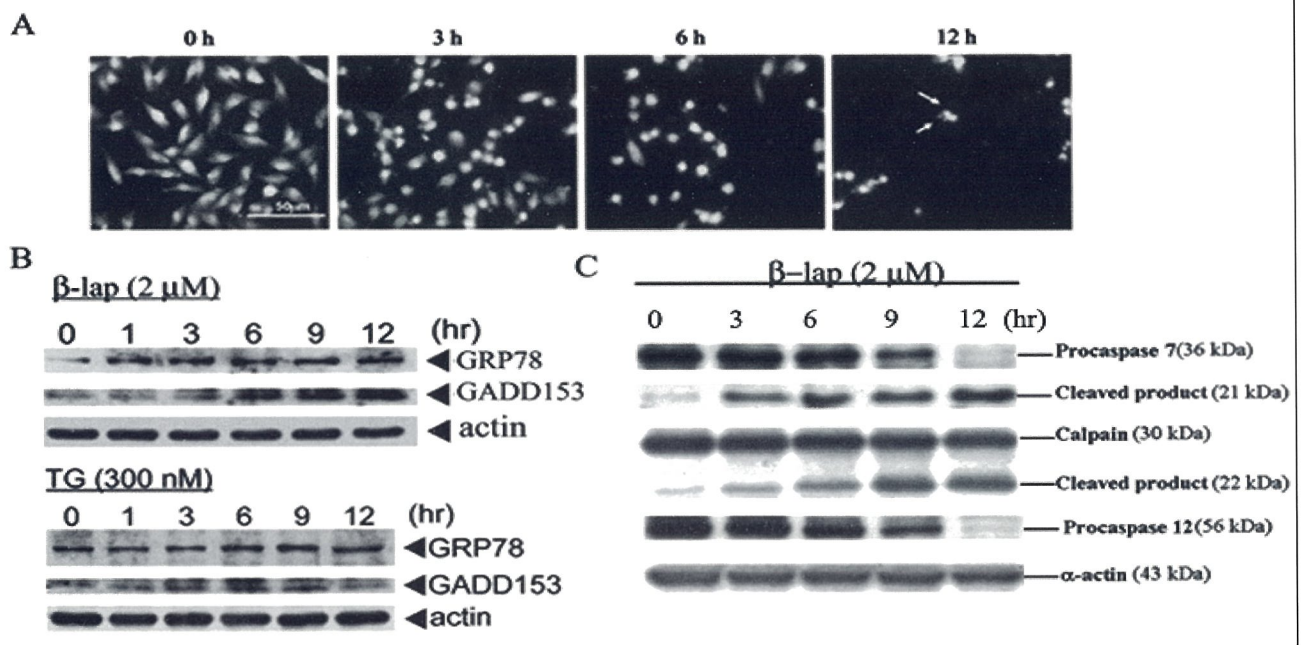

Fig. 1. **Involvement of ER stress–mediated apoptotic signals in β-lapachone-induced cell death of DU145 cells.** (A) Light microscopic photographs of acridine orange-stained DU145 cells after treatment with 2 μM β-lapachone for the indicated time. Note that nuclear blebbing (arrows) is seen after 12 h of β-lapachone treatment. (B) Immunoblot analyses of the expression of GRP-78 and GADD-153 in β-lapachone-treated DU145cells. Cells were treated for the indicated time with 2 μM β-lapachone, then analyzed by Western blot analysis with anti-GRP-78 or anti-GADD-153 antibodies (upper panel). The lower panel shows DU145 cells treated with 300 nM thapsigargin for 0-12 h as a positive control. (C) Immunoblot analysis of the activation of procaspase-7, calpain, and procaspase-12 in cells treated with 2 μM β-lapachone for 0-12 h.

B-P-6: TRANS-DIFFERENTIATION OF HUMAN MESENCHYMAL STEM CELLS IN WHARTON'S JELLY INTO INSULIN-PRODUCING CELLS

HSU, Hsin-Chih (許馨之)；Wang, Hwai-Shi（王懷詩）
Institute of Anatomy and Cell Biology, National Yang-Ming University, Taipei, Taiwan, R.O.C

Diabetes mellitus (DM) is a metabolic disorder that the body fails to effectively utilize or control postprandial blood glucose levels. It is characterized by persistent hyperglycemia. The World Health Organization recognizes three main forms of diabetes: type 1, type 2, and gestational diabetes (occurring during pregnancy). Type 1 is usually due to autoimmune destruction of the pancreatic β cells which produce insulin. Type 2 is characterized by tissue-wide insulin resistance and varies widely; it sometimes progresses to loss of β cell function. Gestational diabetes is similar to type 2 diabetes. Recently, the therapies for diabetes patients are limited in using drugs or injecting insulin directly. Even using the latest technique, islet transplantation, insulin independency could only be achieved for periods no longer than 3 years. Moreover, this therapy for type 1 diabetes is limited by the scarcity of donors.

Many studies show that the stem cells from different source could differentiate into β cells. Mesenchymal stem cells (MSCs) from human bone marrow, embryonic stem cell, liver, spleen, adipose tissue, and pancreas were shown to adopt a pancreatic endocrine phenotype in vitro and to reverse diabetes in an animal model. Accordingly, in this study, we investigate whether MSCs in Wharton's jelly【figure 1】could differentiate into insulin producing cells. At present, by using Western blotting and immunocytochemistry methods, increase expression of insulin、C-peptide and glucagon【figure 3】 were found in cultured cells under defined conditions after 10 days. We also observed expression of pancreatic related transcription factors Isl-1、Pdx-1、glucose transporter Ⅱ（GLUT2）and insulin by RT-PCR. In summary, we suggested that MSCs in Wharton's jelly have potential in differentiating into insulin producing cells and probably be a new source for islet transplantation of diabetes therapy.

Reference

【1】Wang HS, Hung SC, Peng ST, Huang CC, Wei HM, Guo YJ, Fu YS, Lai MC, Chen CC. Stem cells.22(2004)1330

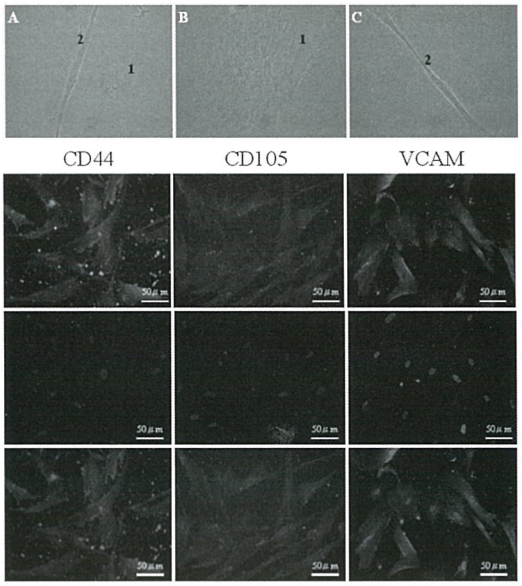

Figure 1.Two type cell morphology were observed. Immunocytochemistry analysisof mesenchymal stem cell markers. Expression of CD44、 CD105 、VCAM. Bar=50 μ m

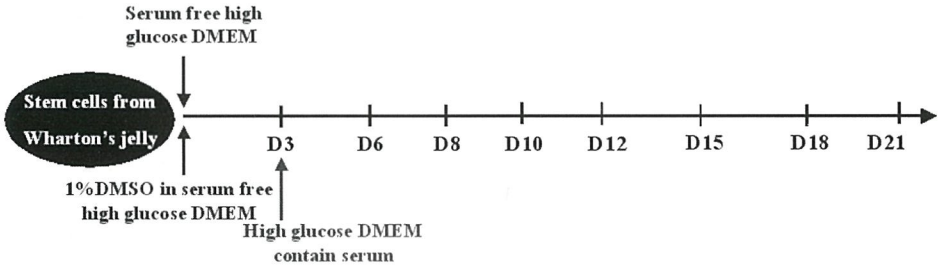

Figure 2. Experimental procedure

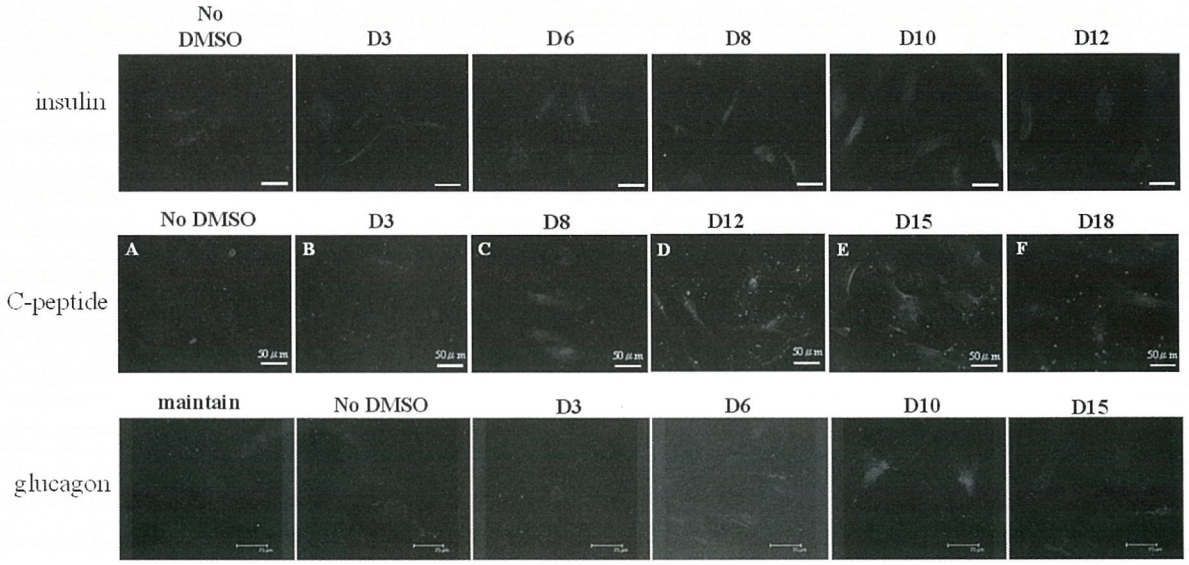

Figure 3. Immunocytochemistry analysis of pancreatic hormone. Lane1:glucagon, Bar=75 μ m. Lane 2: C-peptide, Bar=50 μ m. Lane 3: insulin, Bar=50 μ m

B-P-7: EFFECT OF ISCHEMIA ON THE ULTRASTRUCTURAL ALTERNATION OF THE HIPPOCAMPUS IN THE GERBIL

CHEN, Yu-Lin(陳羽琳)[a], YANG, Cheng-Chang(楊正昌)[a], LU, Min(呂旻)[a], CHEN Yi-Ting(陳宜婷)[a] and YU, Shang-Ming(游祥明)[a]

[a]Institute of Anatomy and Cell Biology, National Yang-Ming University, Taipei, Taiwan

Brain ischemia is a disturbance of the blood flow causing a deficiency of oxygen and glucose to the brain. Ischemia can affect the structural and function of organs or tissues and also cause physiological and pathological alterations including hypoxia, hypoglycermia and blood acidities in experimental animals and human. Previous investigations reveal that the astrocyte has more tolerance to ischemia than that of the neuron. Ischemia also induces the proliferation and hypertrophy of the astrocyte. The aim of this study is to investigate the morphological changes of the hippocampus followed by reperfusion after bilateral common carotid artery occlusion. Mongolian gerbils were followed by bilateral common carotid artery occlusion and reperfusion at different time courses then sacrificed by cardiac perfusion of a saline nitrite flush, followed by a 6% paraformaldehyde-lysine-periodate fixative in 0.1M phosphate buffer. After fixation, the brain were embedded in 5% agar, vibratome-sliced through the hippocampus, and then postfixed in the 1% osmium tetroxide. The brain sections (500μm thickness) were dehydrated by a series of graded ethanol to absolute ethanol and transferred to liquid carbon dioxide for critical point drying. The dried specimens were mounted on aluminum or copper studs, coated with gold (30nm) in a JEOL Ion Sputter JFC-1100 and examined under a JEOL electron microscope (JSM-5300).

At the onset of reperfusion after 60 minutes ischemia, a number of slender microprojections (Fig. 1A, arrow) was closely applied to the exterior surface of the blood vessel. At 30 minutes after 60 minutes ischemia, a plate-like structure (Fig. 1B, arrow) appeared flattened with a ruffled border and was closely applied to the exterior surface of the blood vessel. At 1 hour after 60 minutes ischemia, the red blood cell was located in the perivascular space (Fig. 1C, arrowhead) adjacent to a collapsed capillary (Fig. 1C, double arrowheads). At 6 hour after 60 minutes ischemia, a number of finger-like projections (Fig. 1D, arrows) was closely applied to the exterior surface of the capillary. At 24 hour after 60 minutes ischemia, a striking characteristic was that a capillary (C) contained numerous red blood cells (Fig. 1E, arrows) in its lumen. In addition, a number of the red blood cells also populated within the perivascular space (Fig. 1E, arrowhead). The nucleus (n) of the endothelial cells bulged into the lumen of a capillary (C). A collapsed blood vessel (Fig. 1F, arrowhead) showed no discernible lumen. The perivascular space contained numerous large vacuoles (Fig. 1F, arrow) and trabecula.

B-P-8: CHARACTERIZATION OF INSECTICIDAL ACTIVITY OF GALECTIN-1 AGAINST *PLUTELLA XYLOSTELLA*

CHIEN, Chin-I (簡勤益)[a]; CHEN, Shiang-Jiuun (陳香君)[b]; CHEN, Nien-Ting (陳念廷)[a]; WANG, Siou-Hua (王琇華)[a]; KUO-HUANG, Ling-Long (黃玲瓏)[b*] and HUANG, Rong-Nan (黃榮南)[a*]

[a] Department of Life Science, College of Science, National Central University & University System of Taiwan, Taoyuan 32054, Taiwan.

[b] Department of Life Science, College of Life Science, National Taiwan University, Taipei 106, Taiwan.

Galectin-1 (GAL1) is a mammal lectin which has a carbonhydrate recognition domain recognizing the structural motif, Galβ1-4GlcNAc. Previous study in our laboratory has demonstrated that GAL1 could bind with chitosan (a derivative of chitin) membrane to facilitate 3T3 cell proliferation [1]. These studies further characterized the interaction of GAL1 with chitin. The results showed that GAL1 could specifically bind with chitosan (enzyme-linked immunoassay) and chitin (Pull-down assay). Since chitin is the major component of insect, we therefore further characterize the insecticidal activity of GAL1. The results showed that GAL1 was toxic to *Plutella xylostella*. The histochemical structure and immunostaining suggested that GAL1 binding to the midgut epithelium of *P. xylostella* resulted in dose- and time-dependent disruption of the microvilli, and abnormalities in these epithelial cells. The ultrastructural studies further showed that the peritrophic membrane (PM) was not present in the midgut of GAL1-treated insects; instead numerous bacteria were found in the lumen area. Moreover, the feeding of GAL1 also resulted in interference of carbohydrate metabolism of *P. xylostella*. Moreover, the GAL1 gene was introduced into the genome of ***Baculovirus*** and expressed in sf-21 cells (Fig. 2) to further evaluate the insecticidal activity. In view of GAL1 having a carbohydrate-recognition domain that recognizes the structural motif, N-acetyllactosamine (Gal β 1-4GlcNAc), which is similar to that of chitin (β-1,4 N-acetyl-D-glucosamine), the main component of insect exoskeleton as well as peritrophic matrices lining the gut epithelium, we propose that the possible insecticidal mechanism of GAL1 involves direct binding with chitin to interfere with the structure of the PM.

References

[1] Chang Y. Y., Chen S. J., Liang H. C., Sung H. W., Lin C. C. and Huang R. N. Biomaterials 25(2004)3603

[2] JINN T. R., KAO S. S., TZEN J. T. AND WU T. Y. J. BIOTECHNOL. 119(2005)255

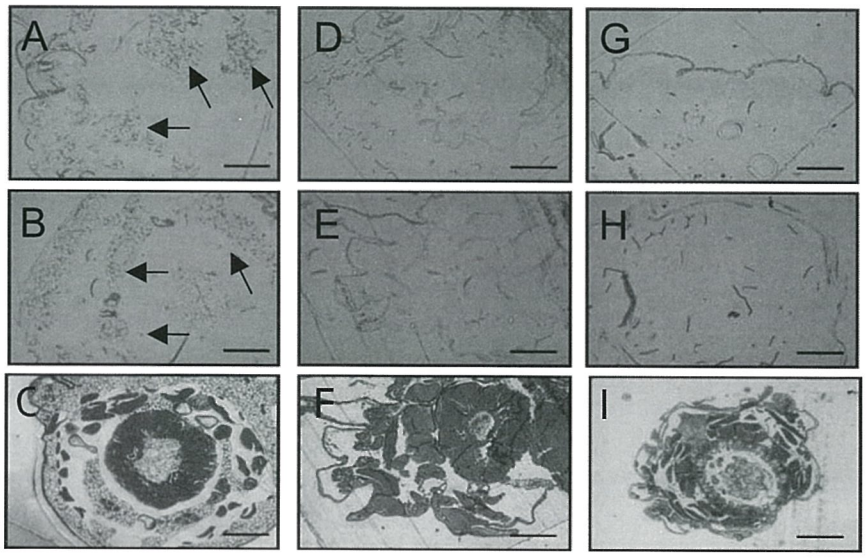

Fig. 1 Effect of GAL1 on carbohydrate metabolism of *P. xylostella*. The larvae of *P. xylostella* were fed on cabbage diet containing GAL1 for 48 hours. Afterward, the larvae were dissected and stained with Safranin O and Fast green stain (C) (F) (I) or with Periodic acid Schiff reagent ((A) (D) (G) and (B) (E) (H) duplicate). The arrows in (A) and (B) indicate the staining of carbonhydrate in control. Bars=1 μm.

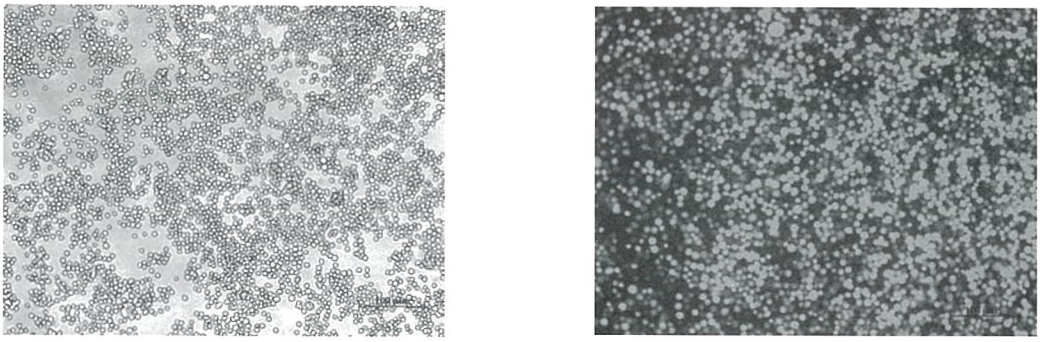

Fig. 2. Expression of GAL1 proteins in sf-21 cells. The GAL1 gene from Chinese hamster ovary cells were constructed into baculovirus expression vector pBac-IR-GFP (AcMNPV-GAL1). The expression vecter (AcMNPV-GAL1) were transfected into sf-21 cells. The intensity of green fluorescent protein (GFP) was used as an indicator for GAL1 expression in Sf21 cells (right panel, 5 days post-infection). Left panel: phase contrast of sf21 cells. Bars= 100μm

B-P-9: MORPHOLOGICAL CHANGES DURING SPONTANEOUS RECOVERY AFTER SPINAL CORD INJURY

YANG, Cheng-Chang (楊正昌)[a], CHEN, Yu-Lin (陳羽琳)[a], LU, Min (呂旻)[a], LIN, Kwan-Hwa (林光華)[b] and YU, Shang-Ming (游祥明)[a]

[a]Institute of Anatomy and Cell Biology, National Yang-Ming University, Taipei 112, Taiwan
[b]Institute of Physical Therapy, College of Medicine, National Taiwan University, Taipei 100, Taiwan

Adult mammal central nervous system (CNS) was vulnerable to injury and trauma. Several degeneration cascades were occurred, including ischemia/hypoxia, ion unbalance, glutamate releasing, neuronal death and axon demyelination. Demyelination may be caused by losing axon support resulting from the apoptosis of the oligodendrocyte after spinal cord injury. Not only apoptosis occurred after injury but also the paraptosis, another kind of programmed cell death (PCDs). Previous study shows that spontaneous recovery is found at some species of rodents. The mechanism of the spontaneous recovery is still unknown. In this study we employed the light and electron microscope to observe morphological alteration after spinal cord injury. Adult male SD rats were hemisectioned at the veterbral level T8 and sacrified at 1, 4, 7 and 14 days after spinal cord sugery. Brain tissues were separated into two parts from the rostral to the caudal and fixed with 6% paraformaldehyde-lysine-periodate (PLP) followed Epon embedding. Spinal cord sections were investigated under the light and electron microscope. At light microscopic level, the spinal cord lost its surface contour and numerous vesicles were present in the white matter and in the cells. During the late stages, numerous spindle-shaped fibrocyte-like cells were found. Under electron microscopic level, the disappearance of cytoplasm and cell membrane of the cell was markedly found at early stage after spinal cord injury. Demyelination was frequently seen at early stage and remylelinated at late stage after the spinal cord injury. At higher magnification, we found many cytoplasmic vacuolations and vesicles containing double membrane structure indicative of the paraptosis. Numerous dilated cisternae of the rough endoplasmic reticulum were found in the spindle-shaped cells.

References

[1] S. Krantic, N. Mechawar, S. Reix, R. Quirion. Prog. Neurobiol. 81 (2007) 179.

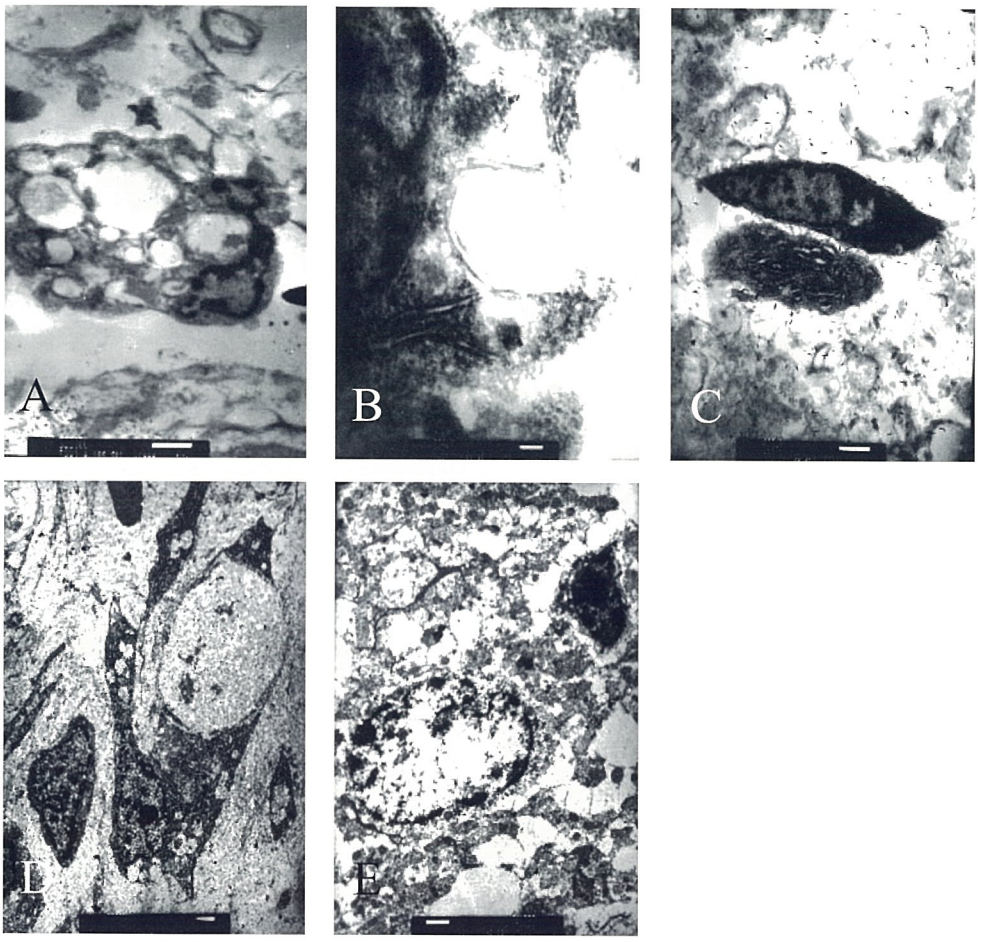

Fig. 1. Micrographs of the transmission electron microscopy after the spinal cord injury. (A) At postlesion day1, several vesicles were found in cytoplasm without distinct contour. (B-C) At postlesion day4, many vesicles contained double unit membrane structure and abundant spindle-shaped fibrocyte-like cells were present in the white matter. (D) At postlesion day7, several fibrocyte-like cells contained dilated cisternae of the rough endoplasmic reticulum. (E) At postlesion day14, the remyelination was present in the spinal cord.

B-P-10: DIFFERENTIAL DISTRIBUTION OF GFP-TAGGED RAT EAG1 AND EAG2 K^+ CHANNELS IN NEURONS

JENG, Chung-Jiuan (鄭瓊娟)[a]; LIN, Huei-Min (林惠敏)[b]; and
TANG, Chih-Yung (湯志永)[b]
[a] Institute of Anatomy and Cell Biology, School of Medicine, National Yang-Ming University, Taipei, Taiwan;
[b] Department of Physiology, College of Medicine, National Taiwan University, Taiwan

The Eag K^+ channel is a member of the superfamily of voltage-gated potassium channels. The mammalian Eag subfamily includes Eag1 and Eag2 K^+ channels, both of which have been shown to express exclusively in the central nervous system. Previous studies from our lab have demonstrated that native rat Eag1 and Eag2 channels displayed differential subcellular localization patterns in hippocampal neurons. In the present study, we aim to study the subcellular localization of GFP-tagged rEag1 and rEag2 K^+ channels in neurons. GFP fusion constructs were created by subcloning rat Eag cDNAs into pEGFP vectors. Upon whole-cell patch clamp recording, HEK293T cells transfected with the GFP-tagged cDNAs displayed outwardly rectifying K^+ currents that were characteristic of rEag channels. We next transfected cultured rat neurons with GFP-rEag1 or GFP-rEag2 cDNA to study the subcellular localization pattern of GFP fluorescence by using confocal microscopy. We found that the localization patterns of GFP-rEag fusion proteins were reminiscent of those for their native counterparts. Our present findings provide further evidence supporting the idea that rEag K^+ channels are localized in the dendrosomatic compartment of neurons. Furthermore, our present findings are consistent with the idea that a significant fraction of rEag1, but not rEag2, K^+ channels are localized in the post-synaptic compartment of synapses.

References

[1] Jeng, C.-J., Chang C.-C., and Tang C.-Y. (2005) *Neuroreport* 16:229-233.
[2] Napp J, Monje F, Stuhmer W and Pardo LA. (2005). *J Biol Chem* **280,** 29506-29512.

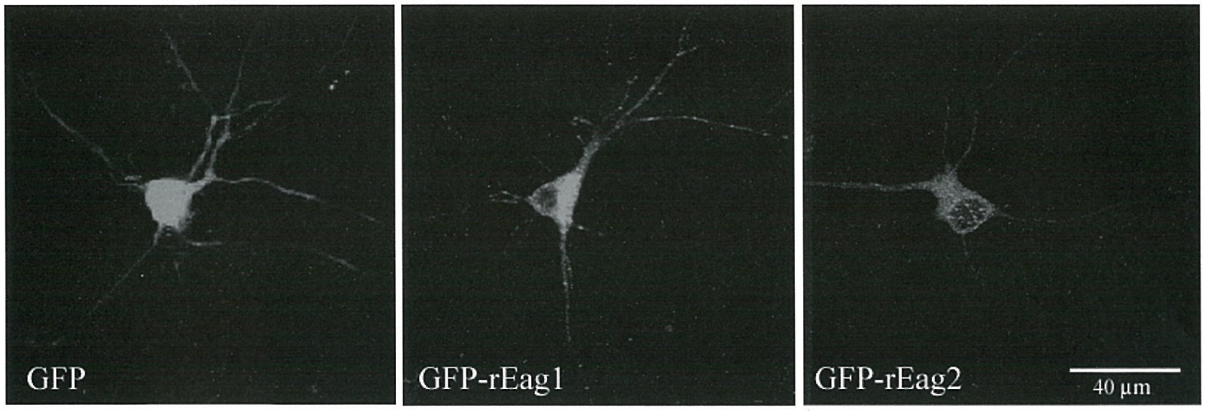

Figure 1. Cultured hippocampal neurons transfected with GFP, GFP-rEag1, or GFP-rEag2.

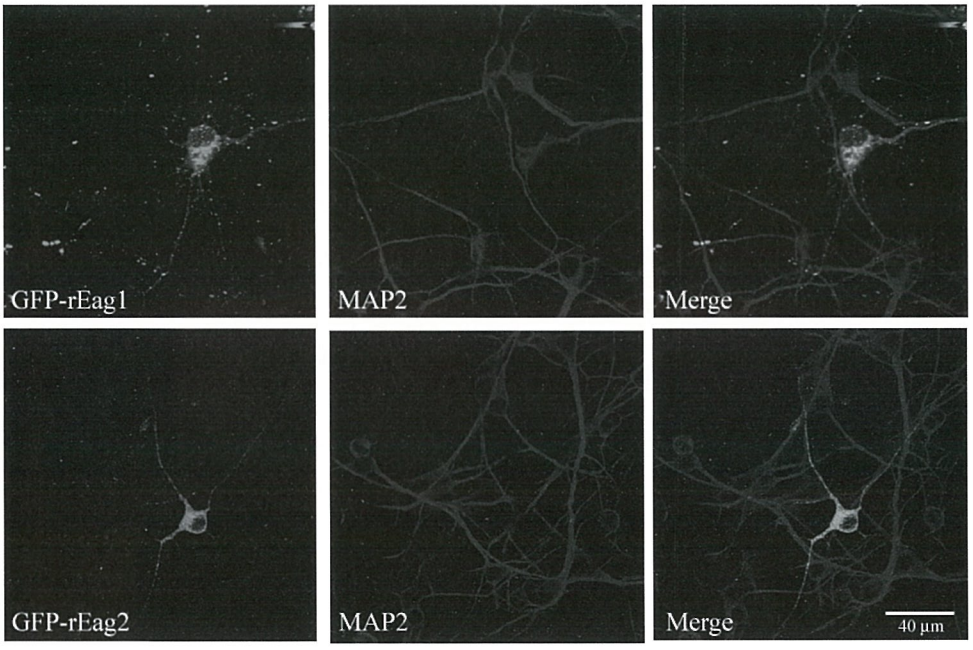

Fig. 2. Dendrosomatic localization of GFP-rEag1 and GFP-rEag2 channels in hippocampal neurons. Hippocampal neurons, transfected with GFP-rEag1 or GFP-rEag2, were labeled with mouse anti-MAP2 (a dendrite marker) antibodies. The co-localization of GFP signals and MAP2 immunostaining patterns indicate that the GFP-tagged constructs possess similar subcellular distribution pattern to those of endogenous rEag1 and rEag2 channels in neurons. Note the punctate staining patterns of rEag1 channels.

B-P-11: THE DEVELOPMENT OF MALE STROBILI AND MICROSPOROGENESIS OF *TAIWANIA CRYPTOMERIOIDES* HAYATA (TAXODIACEAE)

CHEN, Su-Hwa (陳淑華)[1,2]*; CHUNG, Nien-June (鐘年鈞)[3]; WANG, Ya-Nan (王亞男)[3,4]; LEE, Jin-Ling (李金玲)[1] and LEE, Yi-Ling (李宜玲)[1]

1 Department of Life Science, National Taiwan University, Taipei.

2 Institute of Ecology and Evolutionary Biology, National Taiwan University, Taipei.

3 Experimental Forest, National Taiwan University, Nantou.

4 Department of Forest and Resource Conservation, National Taiwan University.

* Correspondence

Taiwania cryptomerioides is an endemic, rare, and extant species to Taiwan. Due to its very good wood quality, relatively rapid growth rate, and high resistance to insect infection, this plant has been selected as an important species for silviculture in middle altitude mountain areas of Taiwan. But, in recent years, it is found that sterile cone is quite common for this species.

In the present study, we investigated the development of male (or staminate) strobili of *T. cryptomerioides* under SEM and examined its ultrastructural changes of microspores during microsporogenesis under LM and TEM. The staminate buds raised in September. Each bud produced 1 to 9 (mostly 4 to 6) staminate strobili, which formed as a cluster at the tip of branch. The staminate strobilus is composed of 15-20 microsporophylls (Fig. 1). Three to five microsporangia are borne at the base of microsporophyll abaxially (Fig. 2). The pollen grains (Fig. 3) were released from the microsporangia at the end of February or the beginning of March when they matured. At the early development stage, the microspore mother cells were enclosed by a layer of tapetal cells (Fig. 4). The microspore mother cells underwent meiosis, followed by subsequent successive or simultaneous cytokinesis to produce microspores (Fig. 5). Then, an asymmetrical mitosis occurred to produce a small prothallial cell and a large embryonic cell (Fig. 6 & 7). This 2-celled pollen is namely a young male gametophyte. The mature pollen grains had a reduced ectexine, lamellate endexine and a very thick intine in their wall structure (Fig. 8), when they were released from the microsporangium.

The present results provide a basis for further study of the male sterility in *T. cryptomerioides*.

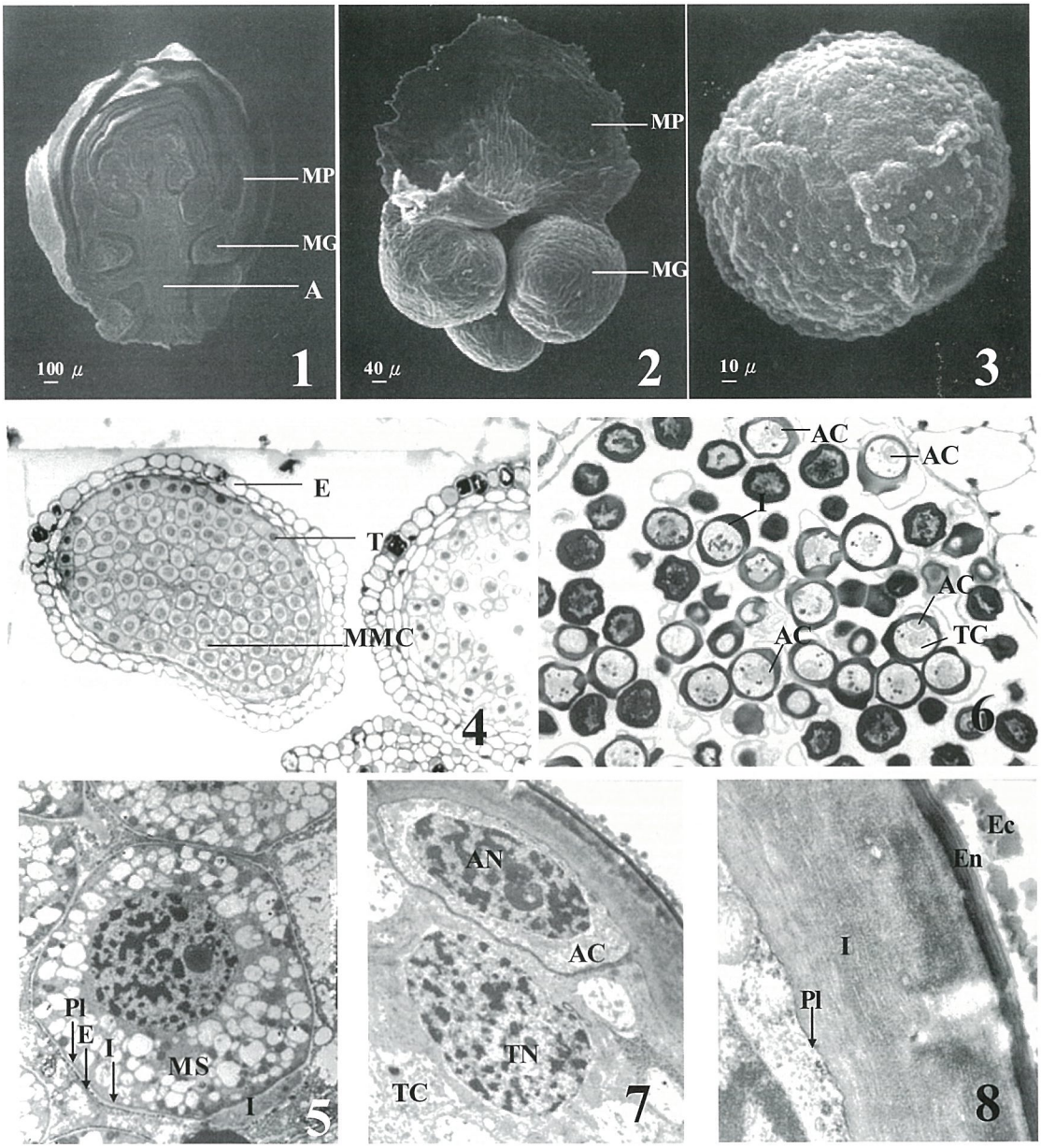

Fig. 1. LS of male strobilus (SEM). A = axis, MG = microsporangium, MP = microsporophyll. Fig. 2. A isolated microsporophyll (MP) with three microsporangia (MG) (SEM). Fig. 3. A mature pollen grain (SEM). Fig. 4. CS of a microsporangium showing microsporocyte (MMC) surrounded by tapetum (T) (LM). Fig. 5. A microspore with non-homogenous thickened intine (I) and a thin synthesizing exine (E) (TEM). Fig. 6. Two-celled pollen with antheridal cell (AC), tube cell (TC) and thick intine (I) (LM). Fig. 7. Detail of a two-celled pollen with an antheridal cell (AC) and a tube cell (TC) (TEM). AN = antheridal nucleus. TN = tube nucleus.

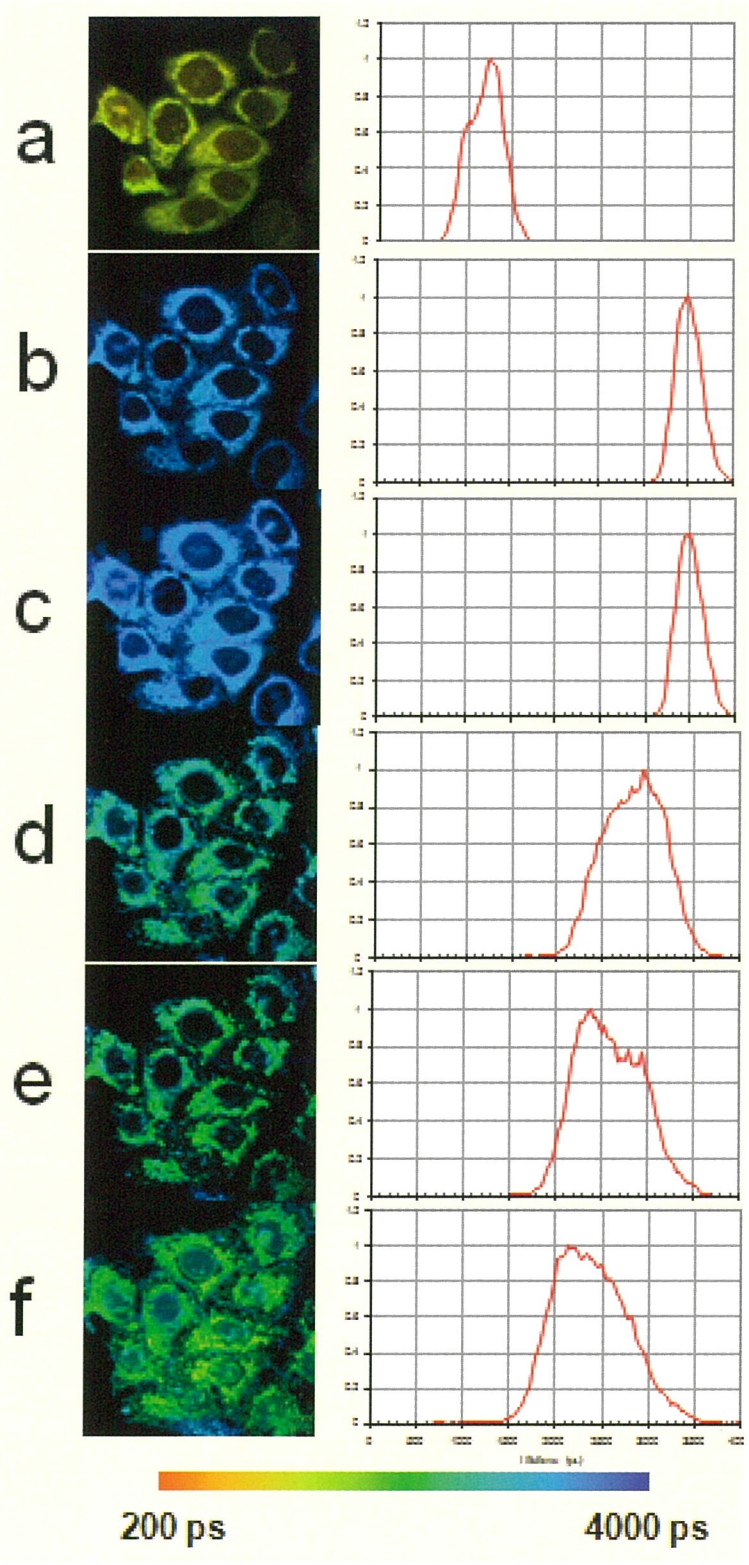

Fig. 1. Lifetime observation in HeLa cells at 15 (a), 30(b), 45 (c), 60(d), 75 (e) minutes and 10 hours (f) after treatment with apoptosis inducer staurosporine (STS). Magnified image shows characteristic to apoptosis morphological changes: nucleus shrinking and blebbing.

B-O-2

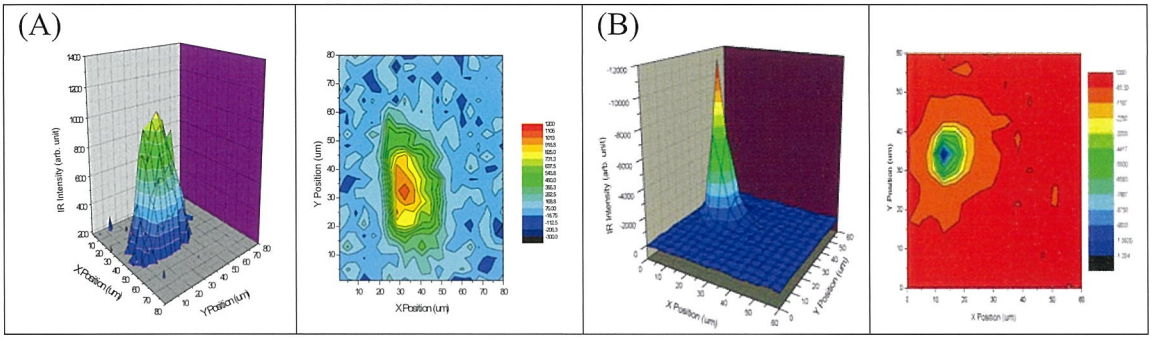

Fig.1. The beam profile of the focused IR beam is mapped by the 5 um pinhole diameter in transmission and the step size of the mapping is 4 μm. (A) The focused beam size of Globar source is around region of 50×30 μm^2. (B) The 2D beam size of the infrared synchrotron radiation is around region of 10×13 μm^2.

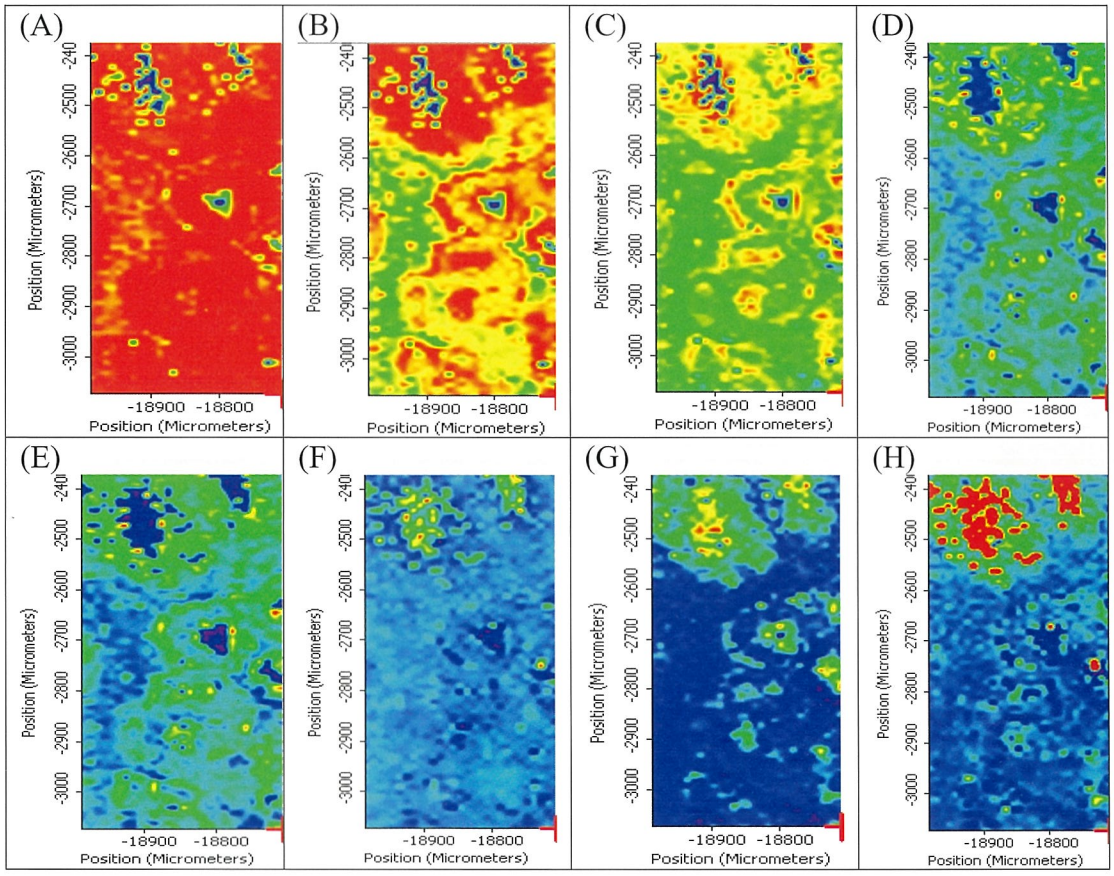

Fig. 2 The functional group map of the deparaffinized colon section of characteristic bands of (A) amide I at 1650 cm^{-1}, (B) amide I at 1638 cm^{-1}, (C) amide II at 1550 cm^{-1}, (D) CH_2 bending at 1467 cm^{-1}, (E), CH_3 bending at 1380 cm^{-1}, (F) ν_{as} PO_2^- (DNA) at 1240 cm^{-1}, and (G) ν_s PO_2^- (DNA) at 1080 cm^{-1}(H) glycogen at 1030 cm^{-1}

B-P-2

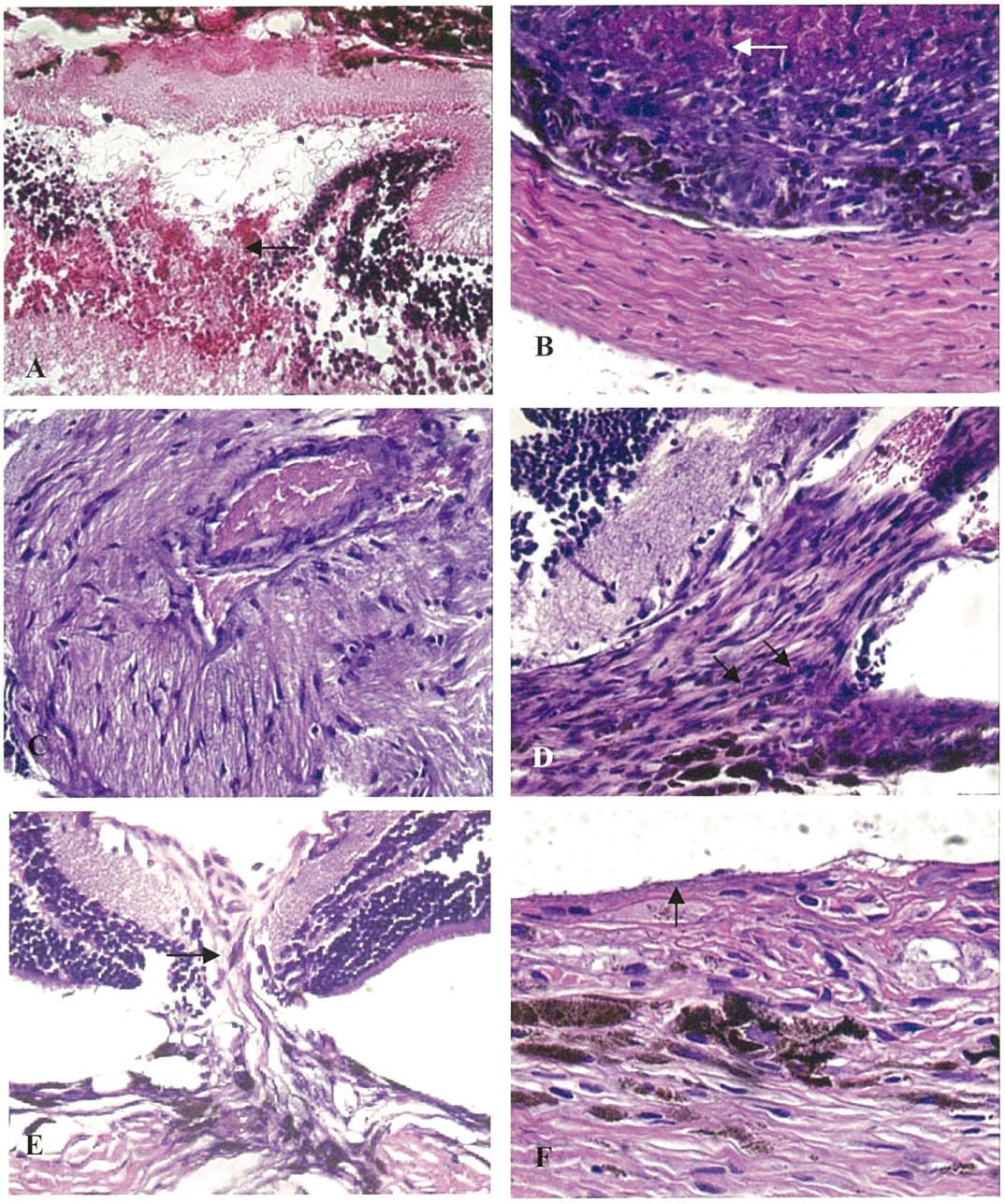

Figures A (postlesioned day 2) through F (postlesioned day 28) revealed the morphological changes after laser application.

益弘儀器股份有限公司

台北 (02)2755-2266　新竹 (03)578-2020　Website: www.ehong.com.tw
臺中 (04)2245-2181　臺南 (06)209-5135　高雄 (07)334-0407　昆山 (0512)57385666

Hitachi 日立電子顯微鏡

Field Emission PC-SEM S-4800

解像力 1.0nm (at 15Kv)
解像力 1.4nm (at 1Kv)

IN-LENS Field Emission PC-SEM S-5500

解像力 0.4nm (at 30Kv) 1.6nm (at 1Kv)

Variable Pressure SEM
S-3000 系列
PC Windows 全自動操作
可變真空電子顯微鏡

解像力 3.0nm / 4.0nm (V.P) [S-3700N 12"]
解像力 3.0nm / 4.0nm (V.P) [S-3400N 8" 含 TMP]
解像力 3.0nm / 4.0nm (V.P) [S-3000H/N 6"]

- ※ HITACHI NANO Prober System N-6000
- ※ HITACHI FIB FB-2100
- ※ HITACHI PC-TEM H-7650 (120KV)
- ※ HITACHI FE-TEM HF-3300 (300KV)
- ※ HITACHI STEM HD-2300A
  HD-2700 (Cs correction)
- ※ HITACHI FE-SEM S-4700/S-4300
  S-4300SE/N (Schottky)
- ※ HITACHI Analytical FE-SEM SU-70(Schottky)
- ※ 其他相關週邊設備及附件
  HITACHI / EMITECH (Quorum)各式
  SPUTTER 蒸鍍機及 CPD
- ※ HORIBA / WDS / EBSD
- ※ HITACHI / E-3500 (Ion Milling System)
  HORIBA / TENSEC (Surface finisher)
- ※ AMT CCD Camera System for TEM (美國)
- ※ EDS 廠家有: Thermo Electron, EDAX, HORIBA

OLYMPUS

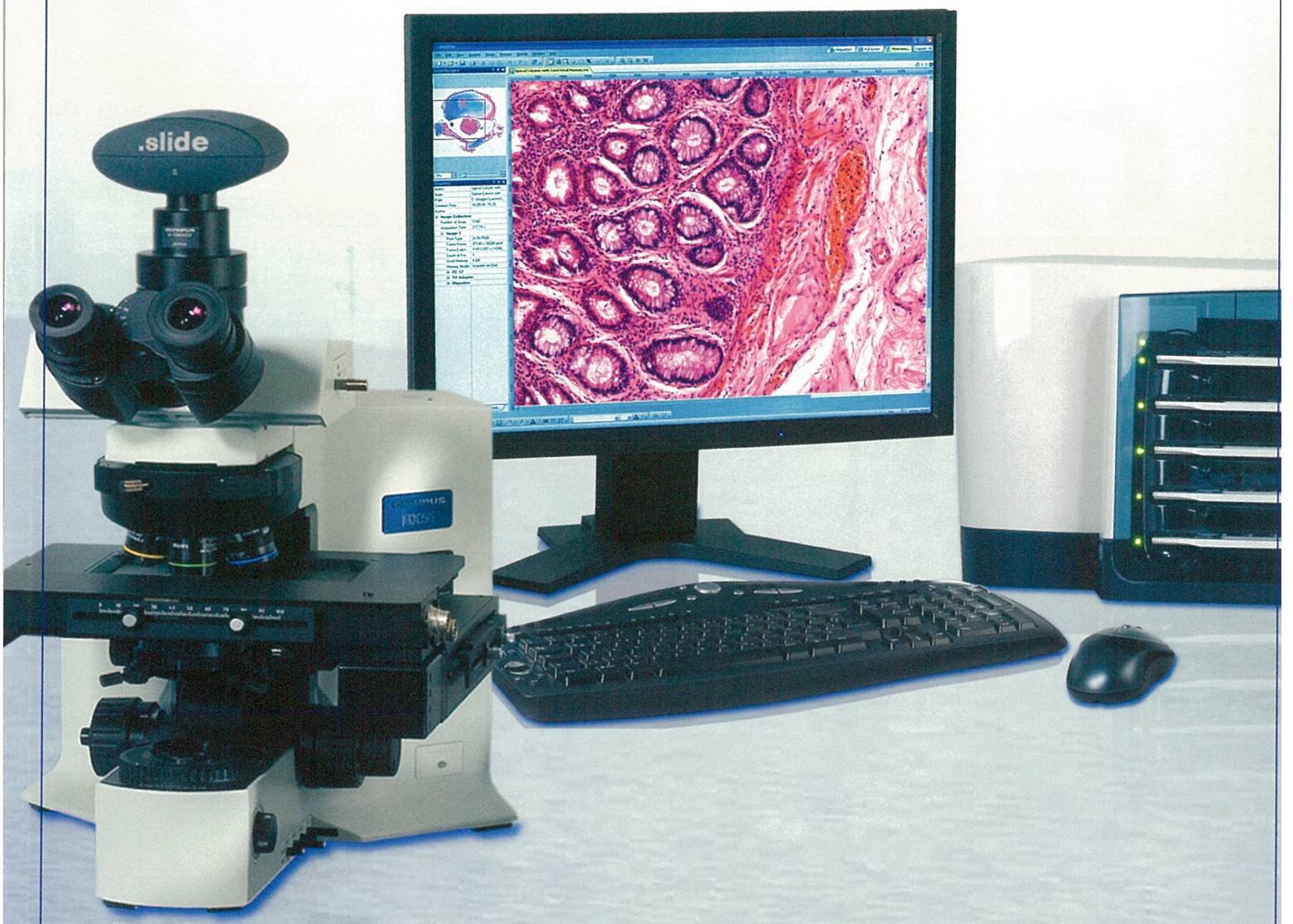

DIGITAL VIRTUAL MICROSCOPY - GET INDEPENDENT OF TIME, SPACE AND EYEPIECE

.slide - Virtual Microscopy System

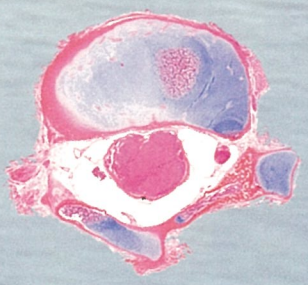

元利儀器股份有限公司
YUAN LI INSTRUMENT CO., LTD
台北市內湖區陽光街365巷39號6樓
Tel:(02)8751-2222 Fax:(02)8751-5356
台中(04)2293-3161 高雄(07)716-1295

元利儀器股份有限公司
YUAN LI INSTRUMENT CO., LTD
台北市內湖區陽光街365巷39號6樓
Tel:(02)8751-2222 Fax:(02)8751-5356
台中(04)2293-3161 高雄(07)716-1295

OLYMPUS

IMAGING EXCELLENCE -
HIGHLY INTEGRATED MULTI-DEVICE IMAGING STATIONS FOR LIVE CELL IMAGING APPLICATIONS

cell^R - Realtime Imaging System

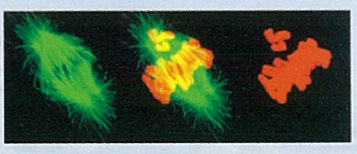

OLYMPUS MICROSCOPY

AppliedPrecision AppliedPrecision

The Gold Standard in Live-Cell

DeltaVision® Core
High-Resolution Live-Cell Imaging System

personalDV
High-Resolution Live-Cell Imaging System

personalDV
High-Resolution Live-Cell Imaging System

- **Faster Acquisition**
- **Fully Integrated**
  - **Hardware and software designed for seamless performance**
- **Precision Travel Stage**
  - **25mm x50 mm stage, 40nm resolution**
- **Compact**
  - **Bench top design to minimize space requirements**
- **Upgradeable**
  - **Options includie Multiplexed Wavelength Imaging, environmrntal contal, DMS lab servr, EM CCD**

沉泰儀器有限公司
Pantech Instruments Co., Ltd.

TEL: 02-27319211 FAX: 02-27319590
E-Mail: sales@pantech.com.tw
Website: www.pantech.com.tw

Image-Pro® PLUS

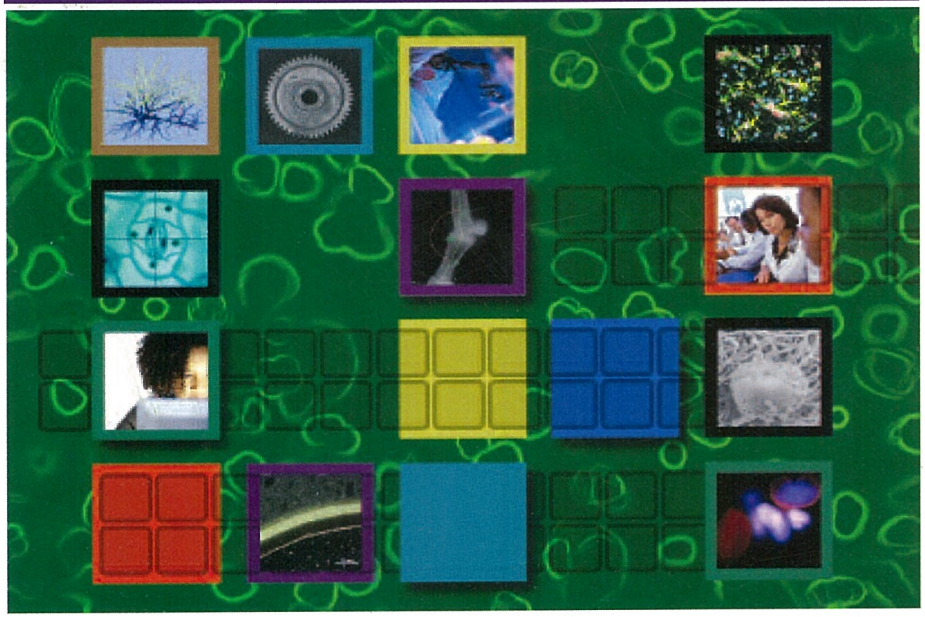

Image-Pro® Plus

Powerful and Customizable
Image Processing and Analysis Software

MediaCybernetics

OPTRONICS

ISO 9001:2000 CERTIFIED
Medical Grade Microimaging Systems™

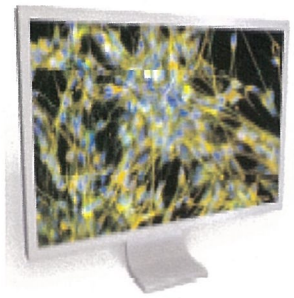

MICROFIRE

Research Grade CCD Imaging for Microscopy

Real-Time Progressive Scan Megapixel Microscope Camera System

- 2-Megapixel Color Imaging
  1600 X 1200 effective pixels creates exceptional image detail and dynamic range in both brightfield and low-light fluorescent images.
- Optronics Exclusive PictureFrame®
  Comprehensive image processing suite with measurement and annotation, scale bar, AVI file-compliant time-lapse imaging, automated image archiving, six position image mixing functionality, flat field correction, background subtraction, live frame averaging with motion compensation and more...
- Direct X Powered
  Real-time, full resolution, full screen preview.
- Intuitive Human Interface
  Powerful software – simple interface means images are captured effortlessly with Optronics point and shoot simplicity.
- TWAIN Compatible Software
  Instantaneous integration within popular imaging applications.
- FireWire® Interface
  Offers "Plug and Play" connectivity from a desktop or laptop computer with data transfer up to 400 mbs.

北區授權經銷商 集可企業有限公司 台北市信義路四段273號5樓 TEL：(02)2704-9669